Mechanical Performance of Additively Manufactured Soft Materials for Ultrasound and Biomechanical Simulation

by

David Edmondson

A thesis submitted to the Graduate Faculty of
Auburn University
in partial fulfillment of the
requirements for the Degree of
Master of Science

Auburn, Alabama
August 9, 2025

Keywords: additive manufacturing, anatomical modeling and simulation, soft mechanics

Approved by

Kyle D. Schulze, Chair, Assistant Professor of Mechanical Engineering
Chad G. Rose, Co-chair, Assistant Professor of Mechanical Engineering
Michael E. Zabala, Associate Professor of Mechanical Engineering

Abstract

Additive manufacturing has enabled the fabrication of anatomically accurate, customizable models for use in medical training and human-interactive technology development. Anatomical manikins produced through these techniques provide a safe, repeatable, and risk-free environment for users to practice and refine clinical procedures or test assistive robotic systems. However, challenges remain in achieving both anatomical fidelity and functional compliance. This thesis explores the design and fabrication of additively manufactured anthropomorphic manikins for two applications: physical simulation in point-of-care ultrasound (POCUS) training and passive validation for upper-limb exoskeletons. In Chapter 2, a passive hand and proximal interphalangeal (PIP) joint model was developed for biomechanical assessment of joint stiffness for future instrumentation using J5 Digital Anatomy Printer (DAP). Anatomical fidelity was achieved through additive manufacturing, the PIP finger model, as well as void-infused thermoplastic polyurethane (TPU), was assessed based on ROM and elastic modulus to ensure appropriate joint compliance via uniaxial displacement, respectively. For POCUS training, a methodology is introduced in Chapter 3 to generate anatomically accurate right upper quadrant (RUQ) models from medical imaging using 3D Slicer. Tissue-mimicking Materials available on the J5 DAP were assessed for their echogenic properties through grayscale intensity analysis, highlighting both their potential and limitations for material tunability and echogenicity for ultrasound realism. The findings of this work address the feasibility of using 3D-printing techniques for soft material prints to fabricate anatomically and mechanically realistic manikins. These manikins have potential utility in enhancing ultrasound medical training and supporting the validation of rehabilitative hand exoskeletons.

Acknowledgments

I would like to express my deepest gratitude to my thesis committee for their invaluable guidance, feedback, and support throughout the course of this work. I am also incredibly thankful to my labmates in the WEBR Lab and S3L for their collaboration, encouragement, and shared dedication, which helped shape and advance this research. Additionally, I would like to acknowledge my summer undergraduate student, Kameron, whose contributions were integral to the efficient fabrication of prints and the generation of experimental results. Sincere appreciation goes to our project sponsors at Auburn VCOM, whose support and resources made this work possible, and to the Auburn ME3D Lab for their assistance in printing models for this study.

There are several non-technical persons that have contributed to the completion of this study. To my parents, Donneth and Hermon Edmondson, thank you for your unwavering love, sacrifice, and belief in me. I also thank my close family, that is, my grandmother, uncles, aunts, brothers and sister who have contributed my journey to this point. A special thank you to my friend Grace and many others present in the Auburn as well as local and foreign Caribbean Communities, whose support and motivation helped me stay focused and grounded during challenging moments. Above all, I give thanks to God, whose grace, strength, and guidance have sustained me through every step of this endeavor.

Table of Contents

List of Figures

List of Tables

Chapter 1

Introduction

1.1 Aim and Motivation

Simulators and manikins play a crucial role in providing a safe, risk-free environment for users to master human-interactive tasks. Medical, rehabilitative and human-interactive robotics fields rely on anatomically realistic manikins and simulators to provide effective training and device validation to ensure human safety. However, current physical simulators for bio-simulation often fall short in either anatomical accuracy or biomechanical compliance—both of which are essential for realistic anatomical representation [1]–[3]. In this study, compliance refers to the ability of a material to replicate the mechanical behavior of anatomical structures in a specific application. To be effective, simulator and manikin materials must exhibit tissue properties that align with the intended use case [4], [5]. Recent advances in additive manufacturing have enabled the development of simulators and manikins that meet both anatomical and mechanical performance criteria [6]–[9].

Additive Manufacturing (AM), once primarily used for prototyping, has evolved into a transformational fabrication method with applications in the medical, industrial, and consumer sectors. With the advancement of multi-material printing techniques and improved machine precision, AM enables the direct production of components with validated structural integrity, performance, and geometric fidelity [10], [11]. Additionally, enhanced layer resolution has contributed to improved surface quality and mechanical strength, while customizable infill geometries enable tunable internal properties [2]. This progress has opened up opportunities for the fabrication of highly complex anatomical structures that would be time-consuming, cost-prohibitive, or infeasible using traditional manufacturing techniques, such as machining or molding [2], [9].

Advancements in AM have not only improved the structural integrity and visual quality of 3D-printed models but also expanded the range of printable materials, enabling the fabrication of softer, more elastic models that enhance realism in anatomical simulation. Printers are capable of layering soft print material with FDM, SLA, and jetting 3D-printing techniques for the creation of non-rigid models. Prior works show the capabilities of additively manufactured to produce complex anatomical models with soft 3D-print material [9], [12], [13].

While there have been improvements in structural and visual quality in addictive manufacturing as well as 3D-printing of soft materials for improved simulation, research into 3D-printing techniques capable of cohesively performing these printing improvements to meet physical simulation requirements of anatomic fidelity and compliance has not been tapped into. Given these limitations, a comprehensive investigation into additive manufacturing methods and material strategies is warranted to develop anatomically realistic and mechanically compliant models.

Several additively manufactured simulators [5], [13], [14] used fused deposition modeling (FDM) printers to print anatomic models of the human body from hard materials, but required additional materials, like composite rubbers, spring steel, agar, or silicone solutions to meet required compliance measures. Other attempts to use softer 3D-printed materials with FDM printing [8], [15], [16] often lack the flexibility in adjusting material properties. Stereolithography (SLA), in addition to FDM 3D prints, is typically restricted to a single material per print to maintain structural integrity, which is not suitable for printing models that require a range of integrated compliant materials. The limitations of these commonly used 3D-printed techniques increase fabrication time, hinder material variation for compliance, and disrupt the continuity between adjacent structures, reducing their ability to fabricate high-fidelity simulators.

The Stratasys J5 Digital Anatomy Printer (J5 DAP) fills this gap in printer technology with its ability to print a variety of soft and hard materials in one build [17]. The J5 DAP is a

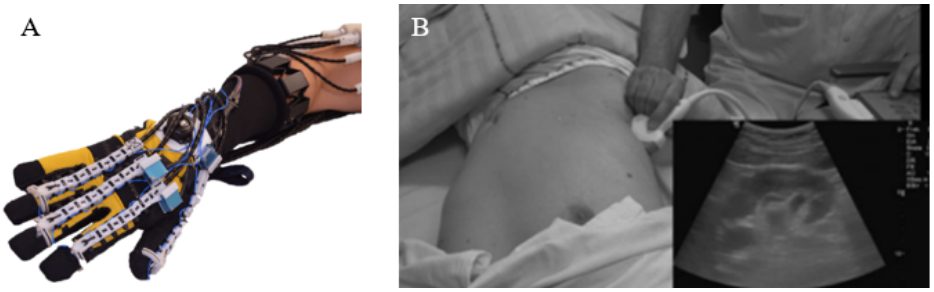

Figure 1.1: (A) A wearable hand exoskeleton designed for hand rehabilitation, requiring validation with a compliant anthropomorphic hand manikin (figure reproduced from [19]). (B) A medical practitioner performing point-of-care ultrasound (POCUS) that encompasses simultaneous processes, illustrating the clinical need for high-fidelity ultrasound manikins for effective hands-on training(figure reproduced from [20]).

material jetting printer that sprays and cures multiple resins, enabling the creation of a wide range of complex organic structures with varying material properties. This PolyJet printer enabled the achievement of both structural and material compliance criteria for anthropomorphic simulation [18]. This study explored the capabilities of J5 DAP to effectively and efficiently produce anthropomorphic high-fidelity models with desired acoustic and elastic properties for ultrasound and biomechanical simulation.

To explore the capabilities of additive manufacturing for creating high-fidelity, compliant manikins and simulators, this study examined two applications: ultrasound (US) and biomechanical simulation. The incorporation of soft 3D-printed materials, such as thermoplastic polyurethane (TPU) and soft resins, into complex anatomical modeling has piqued interest in the clinical and rehabilitation robotics fields [6] for physical anthropomorphic manikins for ultrasound and biomechanical simulation, respectively. To validate the movement of hand rehabilitative hand exoskeleton, similar to Fig. 1.1A, a 3D-printed passive anthropomorphic hand model, to be instrumented, was investigated, along with void-infused soft material as a method for obtaining compliance. For clinical training in point-of-care ultrasound (POCUS), depicted in Fig. 1.1B, the development of an anthropomorphic right upper quadrant (RUQ) US manikin is explored.

1.2 Background and Prior Works

There are two key requirements for accurate simulation: compliance and anatomically correct representation. In this section, previous designs and fabrication techniques used to create compliant and anatomically correct models and manikins were examined for an overview of the current state of the art. Both instrumented and non-instrumented finger and hand models, as well as manikins, were surveyed.

Similarly, abdominal manikins and phantoms used to simulate medical imaging of the human body were surveyed. To validate anatomic models and materials for compliance and anatomical accuracy, relevant anatomy and tissue mechanical properties were reviewed to inform the designs of both ultrasound-compatible and biomechanically accurate anthropomorphic hand manikins. With a focus on J5 DAP for model fabrication and compliance, an overview of its known capabilities was assessed. Prior methodologies used in designing and fabricating anthropomorphic models of the human hand and abdomen offer essential guidance for establishing the design requirements of a manikin produced using the J5 DAP.

1.2.1 Human Hand Anatomy and Biomechanics

The hand is a complex part of the body with several different tissues positioned within a small volume, yet it can carry out dynamic non-prehensile and prehensile functions [21], [22]. The hand consists of a skeleton with 8 wrist bones, 5 palm bones, and 14 finger bones, an exterior layer of skin and a soft tissue layer below [8]. Due to the complexity of the tissue layout within the hand and its size, researchers have focused more on modeling hand external features using non-anatomic intrinsic features. Researchers have aimed to develop anatomically and functionally accurate models of the human hand to reflect its structural and dynamic intricacies [22]. Some of these models, presented in Fig. 1.2, include the use of mechanical joint systems with interlocking rotating components, which can perform expected hand positions successfully, instead of biomimetic modeling.

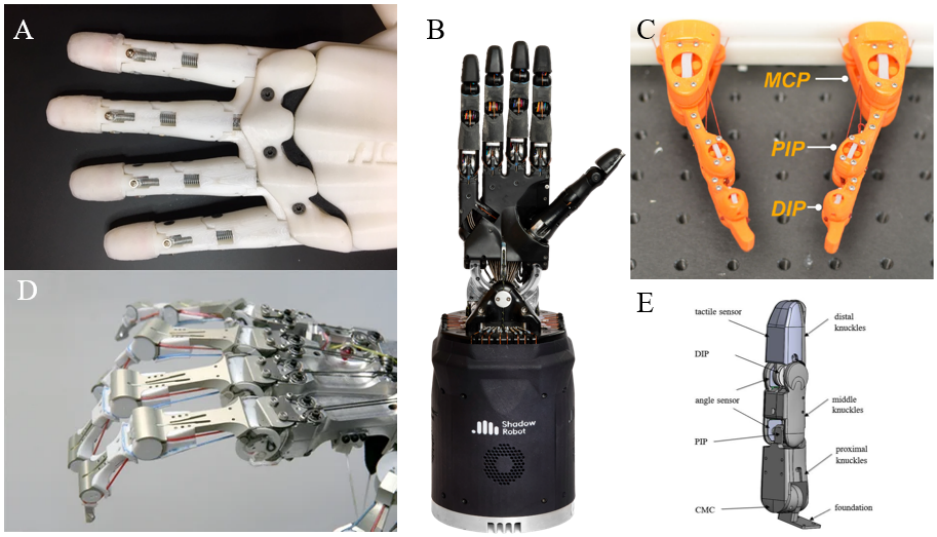

Figure 1.2: Mechanically driven and anthropomorphic hand models feature mechanical joint connections and stiffness mechanisms involving springs and pulley systems. These designs primarily mimic the external features of the hand rather than the detailed internal anatomy. Figures are reproduced from: (A) [23], (B) [24](C) [25], (D) [26],(E) [27]

As manufacturing technology has advanced to produce parts with higher tolerances, designers have created models that operate within anatomically correct volumes. To recreate accurate human hand biomechanics, researchers commonly follow a biomimetic approach, designing anthropomorphic hand models that reflect the structure and function of the human hand from an anatomical perspective [3], [5], [28]. Advancements in machining and manufacturing technologies—including CNC machining, casting, and additive manufacturing—combined with improved techniques for generating virtual models from medical imaging and cadaveric data, have facilitated the fabrication of highly detailed physical representations of bone, ligament, muscle, and tendon structures [3], [5], [29].

For the creation of a passive anthropomorphic hand or finger model, anatomically compliant passive joint stiffness must be replicated for desired biomechanics [14]. According to Kuo et al. [30], the muscle tendon unit (MTU) and capsule ligament complex (CLC) contribute to the passive joint stiffness of a finger joint, which means the contributions of an inactive muscle can be neglected and would only be necessary for simulating the overall

weight of the hand. To maintain joint motion, bone ends must be modeled correctly to provide joint dynamics [3].

Hand Skeletal System

Bone interactions in the hand heavily contribute to the dynamic movement of the hand. The long bones in the hand have endings curved to create smooth joint movement in their intended degree of freedom (DOF) [3]. As a result, modeling of bone is an essential element in creating a hand model. Modelers have created skeletal-based anthropomorphic anatomical models of the hand for high-fidelity biomechanical movement with no external features [3], [5], [28], [31], [32]. Accurately modeling the human hand requires precise representation of the fingers and joints, as they are critical to its functional biomechanics. In this study, the wrist joints were considered outside the scope of investigation. For creating a hand model, four primary bones were considered, introduced in Fig. 1.3, to model the kinematic movement of the fingers in the hand. These are the metacarpals, distal phalanges, proximal phalanges, and middle phalanges, which are not present on the thumb.

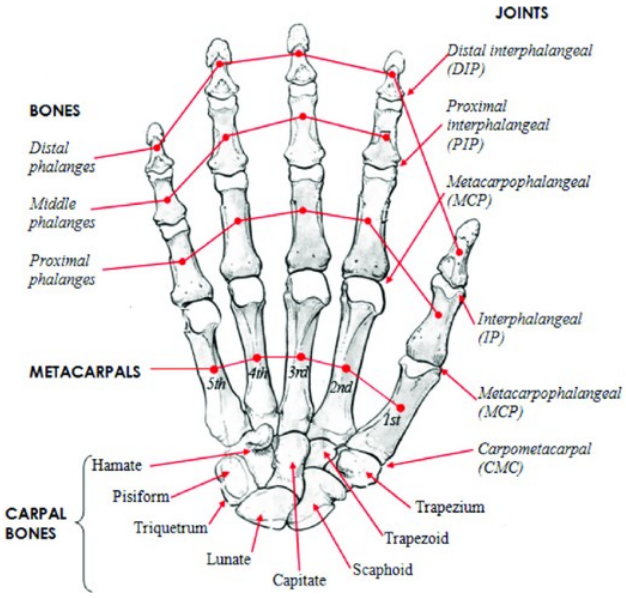

Figure 1.3: Anatomical diagram of the human hand skeletal system, illustrating the bones and joints that provide the structural basis for movement, load transfer, and inertial characteristics essential to hand biomechanics (figure reproduced from [33]).

While modeling all finger and thumb joints is essential to the production of a fully dexterous hand model, exoskeleton designers tend to focus on the thumb, middle, and index finger because they are the main fingers used for grip poses [34].In this study, the development of a 3D-printed model focused on the proximal interphalangeal (PIP) joint of the index finger—formed between the proximal and middle phalanges—and the distal interphalangeal (DIP) joint of the index finger—formed between the middle and distal phalanges—are classified as hinge joints. These joints are modeled with a single degree of freedom, allowing only flexion and extension [35]. The PIP joint of the index finger was chosen for examination to apply the methodology to create a compliant joint model that could be used for other hinge joints and future instrumentation of the hand.

Hand Ligaments and Tendons

Ligaments and tendons play a crucial role in creating a compliant passive hand manikin, contributing directly to the passive joint stiffness of the finger joints. Kuo et al. [30] investigated the contribution of the MTU against the CLC, examining the contribution of MTU to passive joint stiffness in comparison to the CLC's contribution to passive joint stiffness. By evaluating the MCP joint of the index finger, they concluded that the CLC contributes to over 50% of passive joint stiffness. Further studies have confirmed these findings by testing cadaver MCP joint properties [14]. While the CLC is primarily responsible for passive joint stiffness, it is understood that both the CLC and MTU contribute to passive joint stiffness and should therefore be modeled in an anthropomorphic bio-mimetic passive manikin.

Ligaments extend across joints, connecting bones and encapsulating synovial fluid between them. The ligament structures in the hand are thin and complex structures with collagen tissue running over each other, preventing hyperextension and maintaining expected DOFs [31]. Figure 1.4 shows a diagram of the CLC that surrounds the PIP joint of the index finger.The CLC has been modeled with individual ligament representation as well as

mass representation. Key ligaments for biomechanical simulation were volar, collateral, and accessory collateral ligaments [8].

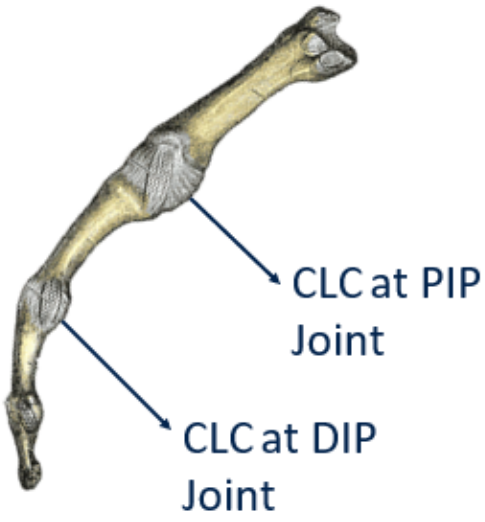

Figure 1.4: Anatomical diagram of the capsule-ligament complex surrounding the distal interphalangeal (DIP) and proximal interphalangeal (PIP) joints of the index finger. This structure is a key component in passive anatomical finger modeling, contributing to joint stability and controlled range of motion. (figure reproduced from [36]).

Cast rubber-like materials, crocheted synthetic polymers, and a combination of both have been used to represent the ligament complex in anthropomorphic design [5], [14], [29],shown in Fig. 1.5.

Tian et al. [8], Hughes et al. [32] and Tebyani et al. [37] models, seen in Fig. 1.6, have fabricated 3D-printed biomimetic ligament structures using elastic rubber-like material. This demonstrates the capability of 3D-printing to fabricate anatomical ligament structures that replicate the form and mechanical function of natural ligaments.

Tendons in the hand are responsible for creating movement in the fingers by applying the force generated by the muscles pulling on them onto the bone they are attached. The index finger has two main types of tendons: extensor and flexor. Extensor tendons make a thin complex structure on the dorsal side of the finger, with tendon tissue laid in multiple

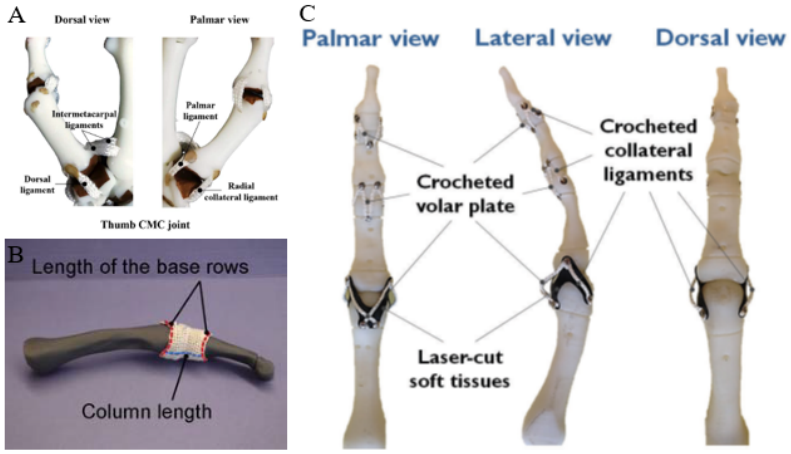

Figure 1.5: Examples of anthropomorphic hand designs that used a combination of crocheted synthetic polymers and cast rubber materials to simulate ligament biomechanical properties. These materials are employed to replicate the mechanical function and flexibility of the human ligament. Figures reproduced from: (A) [14], (B) [5], (C) [29]

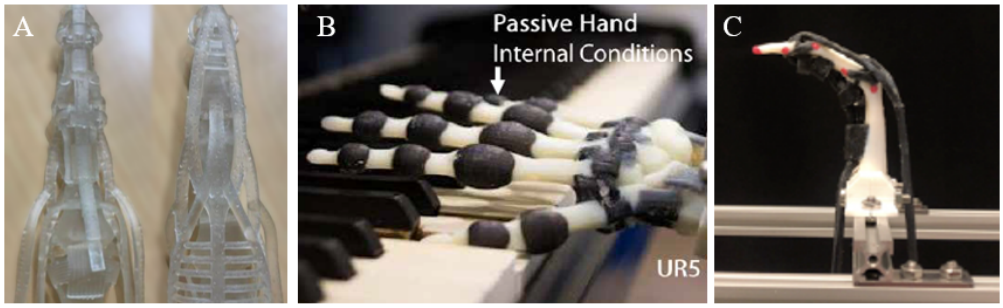

Figure 1.6: 3D-printed biomimetic ligament structures were created using elastic, rubber-like materials on anatomical finger models, demonstrating the capability of 3D-printing to replicate the anatomical form and mechanical function of natural ligaments. Figures reproduced from: (A) [8], (B) [32], (C) [37]

directions across the bone for extension of the finger [3]. On the volar side of the hand, there are less complex tendons that run directly along the volar side of finger bones responsible for flexion of the finger [14]. These two tendons work together to produce active movement of the finger. Figure 1.7 is a diagram of the flexor and extensor tendons running along the finger.

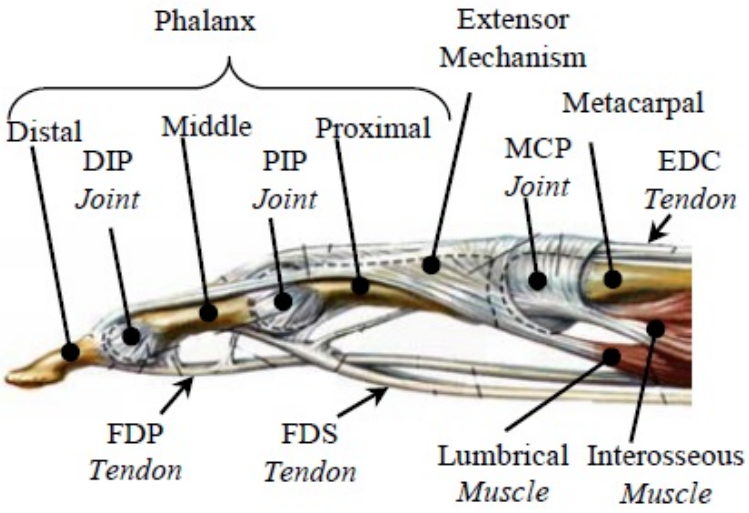

Figure 1.7: Anatomical diagram illustrating the flexor and extensor tendon systems of the index finger. These tendon systems generate flexion and extension movements in response to muscle contraction.(figure reproduced from [38]).

1.2.2 Elastic Properties of Ligaments

This study examined ligament elastic properties as the dominant contributor to passive joint stiffness. Ligaments are anisotropic, making 3D-printed representation directly applicable, if the print direction of layer lines are strategically chosen to be in the same direction as the anisotropic fibers in the ligament faces. The ligament's collagen fibers, when pulled uniaxially along their anisotropic direction, have a non-linear stress-strain relationship which consists of a non-linear toe region, due to crimping of fibers when relaxed, a linear elastic

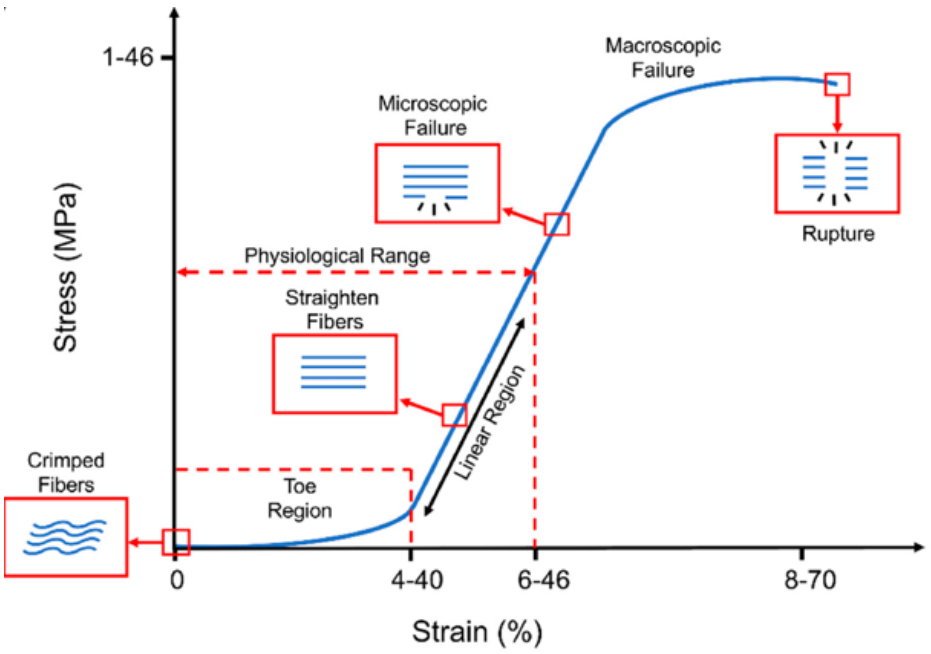

Figure 1.8: Representative stress-strain plot of human ligaments showing their non-linear mechanical behavior. The curve includes labeled regions with a toe region from initial fiber crimping, a linear elastic region, and a plastic deformation region. The figure also highlights the wide range of ligament mechanical properties found in human ligament tissues.(figure reproduced from [39])

region, followed by a non-linear plastic deformation region. Figure 1.8 illustrates this non-linear stress-strain relationship, with the wide range of ligament mechanical performance metrics seen in human ligaments.

Given that the ranges for elastic region strain limits as well as ultimate stress and strain reported by Pioletti et al. [39] differ by an order of magnitude, there is a need for a more narrowly defined range of ligament properties specific to hand ligaments. To narrow the expected range to that of finger ligaments, a study was conducted on the ulnar collateral ligament of sixteen fresh-frozen thumb cadavers [40]. They reported a failure load of 294.3 *pm* 28.2 N, a maximum stress of 11.4 *pm* 1.2 MPa, and a Young's modulus of 37.3 *pm* 5.1 MPa for the intact ligament. It is expected that other finger ligaments exhibit similar elastic properties, thus narrowing the broader ligament property ranges reported for the human body. To meet compliance requirements in a PIP finger joint model, the simulated ligament material must possess elastic properties within these refined ranges.

Beyond elastic properties, ligament performance can also be evaluated based on joint stiffness and range of motion (ROM). In passive hinge joints of the finger, a double exponential torque-angle relationship is expected when the joint is subjected to loading and unloading [34], [41]–[43]. Figure 1.9 demonstrates this double exponential behavior in a DIP joint model, which closely resembles the passive biomechanical response of human joints. Additionally, for the index finger, the PIP joint typically exhibits a maximum flexion of approximately 110° and full extension to 0°. Meeting these kinematic and mechanical benchmarks is essential for achieving compliance in the anatomical PIP joint model.

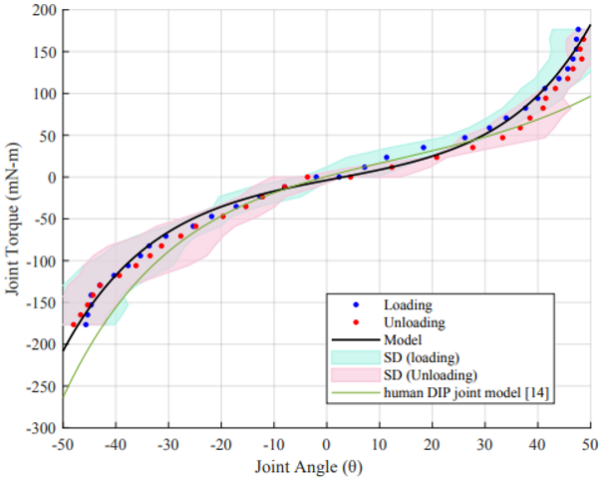

Figure 1.9: Double exponential joint model representing the passive biomechanical behavior expected in finger hinge joints. Shown here is the model applied to the distal interphalangeal (DIP) joint of the index finger in an anthropomorphic hand manikin (image reproduced from [34]).

1.2.3 Review of Anthropomorphic Instrumented and Non-Instrumented Hand Models

Anthropomorphic Hand Models have been previously created for prosthetics, robotics, testing, simulation, and modeling to mimic the human form for both aesthetic purposes and the preservation of human dynamic behavior [22]. Researchers have created anthropomorphic models in two main ways: models with external hand features but not internal ones, or through anthropomorphic modeling of bones, ligaments, and tendons.

Models were anthropomorphized by having a mechanically connected system shaped like the external features of the hand or covered with a replica of the hand's external features. The external material used was made from hard plastics or soft, often elastic, materials for grip simulation. These soft robots utilize materials such as rubbers, springs, shape-memory alloys (SMA), and pneumatic tubing to achieve compliant stiffness [8], [25]. These models previously created compliant joint stiffness by modeling ligaments and tendons using adapted spring systems, tension-driven cables and pulleys, or belt mechanisms across joints [27], [44]–[46]. Bones are connected directly with pin joints or by a stiffness mechanism. Other models use pneumatics for stiffness control [47], [48]. Pneumatic models utilize soft robotic fingers that are capable of gripping objects, but are are not suitable for a passive hand, relying on an active air supply.

This method of modeling demonstrated more predictable kinematic movements that have been mathematically modeled for active control. The hand does not give developers a large volume to place the electronics required for a feedback system. Tactile or position-instrumented models often employ this form of anthropomorphic modeling for sensor and wire placement within finger models. Sonoda et al. [49] utilizes the palm volume for housing electronics.

Review of Non-Instrumented Anthropomorphic Bio-Inspired Hand Models

Modelers have taken a more direct approach to creating anthropomorphic finger or hand models by emulating bone, ligament and tendon structures to create desired biomechanical properties. These models have used anthropomorphic bone structures joined together by rubbers, rubber-like elastic plastics or synthetic polymers to form tendon or ligament complexes. The key to hand dexterity lies in anthropomorphic modeling to achieve human hand biomechanics [8]. Bones have been machined in earlier models and have transitioned to additive manufacturing for reasons such as reduced manufacturing costs and advancements

in printing techniques, allowing for more detailed and efficient modeling. This case study focused on these previous works that used biomimicry for anthropomorphism.

According to Weghe et al. [3], mimicking joint geometry for ROMs and DOFs, joint internal friction, and elastic properties for consistent dynamics, bone inertia, and centers of mass (COMs) are key functions required to produce an anthropomorphic, anatomically correct test bed. Researchers have taken similar routes to create anthropomorphic finger or hand models using rubber or intertwined synthetic polymers to simulate the biomechanical responsibilities of tendons and ligaments.

With the growth of additive manufacturing technology, hand modelers have leveraged these techniques to create cost-effective, complex models. Researchers have printed bone structures modeled from laser-scanned cadavers to simulate anatomically correct bone interactions. Bones have been fabricated from materials such as hard resins [37] and polylactic acid (PLA) material [5]. Modelers have differed in their representations of the CLC and the extensor and flexor tendons. While these models directly mimic anatomic elements, lightweight 3D-printed materials have difficulty simulating hand mass properties. However, joint stiffness has been achieved with these models by increasing stiffness of joint stiffness elements.

Models,seen in Fig. 1.10, have attached molded or cut composite materials across printed bone joints to form novel anthropomorphic ligament and tendon structures using elastic rubber-like materials like silicone rubbers and TPU, as well as crocheted synthetic polymers like nylon or polyethylene terephthalate (Polyester, PET) PET [5], [14], [29], [31], [50]. These materials are used in novel ways using biomimetics to simulate finger biomechanics.

These designs are attached to the bone using epoxy, fittings made for affixation of soft tissue models to bone or mechanical fasteners. Some designers have taken a step further than simulating ligament and tendon structures by modeling cartilage and synovial fluid, applying low-friction materials and lubricants to the end of bone structures [5], [50] and for low joint friction, Xu et al coated 3D-printed PLA bone endings with PLA.

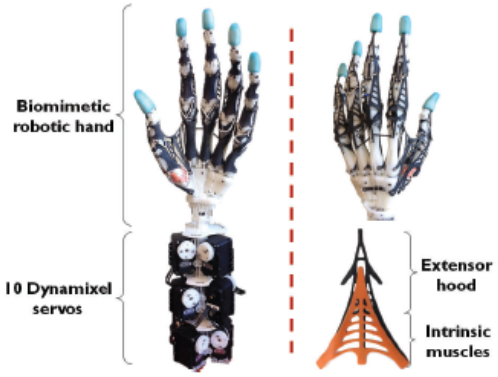

(a) Xu et al. used 3D-printed bone structures from a laser-scanned cadaver with ligament capsules inserted with screws across the joints. Biomimetic ligament structures comprised of laser-cut rubber and crocheted synthetic polymer, while tendon structures were laser-cut from rubber(figure reproduced from [29]).

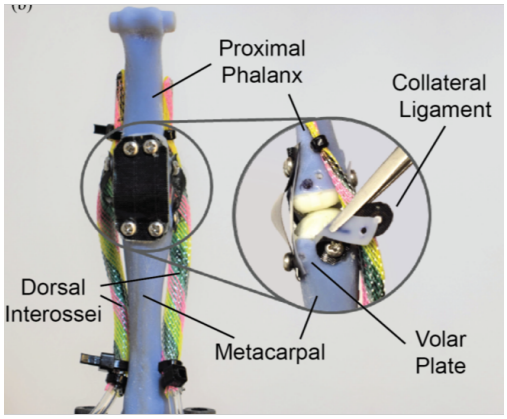

(b) Gollob et al. used a novel ligament structure of cast TPU and nylon sheets attached across 3D-printed bone with screws to form a joint model. Pneumatic artificial muscles represented by wire mesh and thermoplastic elastomer (figure reproduced from [50]).

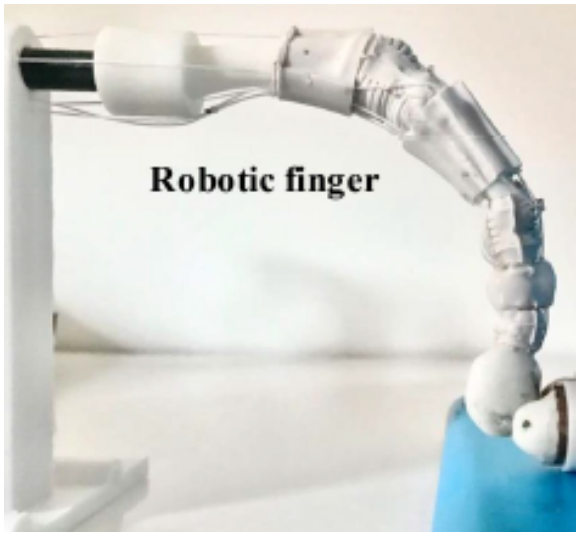

(c) Zhu et al. used polyethylene terephthalate (PET) fiber ribbons to simulate ligament capsules that were sintered to bone across joints. Tendon sheaths were created with silicone rubber and fibers with fishing line (figure reproduced from [14]).

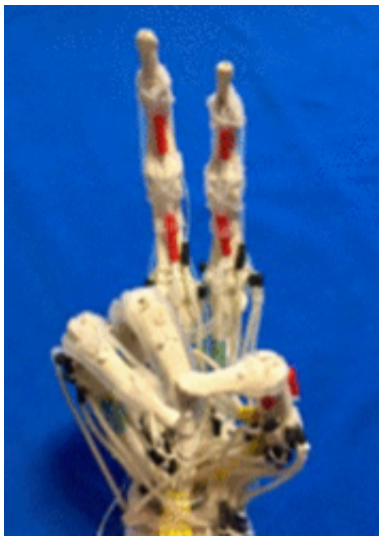

(d) Faudzi et al. used composite rubbers glued across joints to simulate ligaments and thin high-density polyethylene, with high tensile strength for tendon simulation (figure reproduced from [31]).

Figure 1.10: Anthropomorphic finger and hand models developed to replicate anatomical structure and joint mechanics using 3D-printed bones and synthetic ligaments or tendons. These models employ a combination of molded or cut elastic materials, such as silicone rubber or TPU, and crocheted synthetic polymers to simulate ligament and tendon function.

While these models have introduced new anthropomorphic representations of hand anatomy with biomechanical properties, they lack continuity between hard and soft tissue connections. To combat this problem, Tian et al. [8] proposed a cost-effective, easy-to-print anthropomorphic model made of a single material with ligaments and tendon structures printed in one go. They obtained bone structures from 3D scans and used computer-aided design (CAD) software to create flattened, curved cylinders grouped together to simulate ligament tissue and elongated to create thin tendon strands. Although they successfully created a soft cost-effective active hand model, this resin 3D-printed model is incapable of simulating the disparity in material properties in the hand.

Multi-material 3D-printing technology supports the fabrication of continuous, integrated structures that replicate both hard and soft tissues within a single print. Tebyani et al. [37] and Huges et al. [32] both use the Stratasys Connex Printers, a multi-resin printer capable of mixing specific ratios of resins to produce new materials, to manufacture their respective models. Tebyani et al. utilized 3D-scanned bones and bio-inspired CAD designs of ligament and tendon structures to create an active hand. Using the poly-jet printer, they create the bone from a hard resin material and use a mixture of rigid and elastic resin to simulate ligaments and tendons. It is clear from the design that focus was placed on active control of their finger design rather than modeling passive attributes. Hughes et al. focused more on passive finger attributes using a purchased 3D hand consisting of CLC models across each joint and hand skeletal system. However, a similar material selection strategy to Tebyani et al. was used. Both models demonstrated strong performance in simulating soft and hard tissues of the hand, with their effectiveness validated through experimental testing and mathematical simulation. It is believed that a multi-material printer, such as the Stratasys J5 DAP, can be used to create a hand manikin that accurately models both tendon and ligament structures, resulting in a more realistic anthropomorphic model with continuity between soft and hard tissue. This will lead to a model capable of simulating hand dexterity that can be created from a single source.

Many bone-based models have created bone structures from cadaver scans and bio-inspired ligament and tendon structures. However, literature does not show them to have made a complete soft anthropomorphic cover to represent muscle mass, subcutaneous fat or skin, to simulate bunching of skin and tissue during motion and contact interactions. In addition, limited focus was placed on the proposal of a method for developing a hand or finger model from medical imaging [29], which would be beneficial for testing custom hand exoskeletal devices.

While changing bone length can be adjusted to match hand sizes, the full dexterity of individuals' hands can be modeled through this method, including potential abnormalities. To test and validate the movement of exoskeletons, anthropomorphic finger models must be able to measure position data in real-time during testing, eliminating motion tracking data collection methods, as soft exoskeletons are typically placed on a glove or made glove-like, which impede the kinematic motion of a user's hand. Therefore, an instrumented hand model is necessary to perform the task of testing and validating hand exoskeletons.

Review of Instrumented Compliant Hand Manikins

Previous anthropomorphic manikins have included joint angle sensors for feedback control of their active robotic hands, which do not account for passive stiffness or have not verified compliant stiffness across joints, as they focus more on accurate movement when active than passive [22]. These models also contain various machined and purchased parts that make a complex assembly. Prior works have attempted to create an efficiently manufactured, cost-effective passive instrumented manikin for exoskeleton validation with 3D-printable anthropomorphic designs. Yousaf et al.[51] manikin models joint stiffness with a steel spring and pin joint mechanical design. Joint angle was measured via a magneto-resistive angle sensor for zero-contact measurement, eliminating sensor friction contribution to joint movement. This model was hand-shaped and human-like, but not anthropomorphic. Yousaf et al. was able to achieve derived joint stiffness but struggled to overcome noise from the

proximity of the magnet. Baskaran et al. [34] attempted to make a more biometric and anthropomorphic hand with an exterior hand-shaped PLA 3D print. A novel pulley system with durometer 60A rubber for compliant joint stiffness simulation, inspired by the compliant non-instrumented finger model by Kuo et al. [42], was proposed. The design incorporated a potentiometer for measuring joint angle. This model employs the external feature model approach for anthropomorphism, featuring a mechanical mechanism housed within a case with external hand features. Yun et al. [41] also created an instrumented test bed using steel springs and MR sensors, but lacked anthropomorphic features. Figure 1.11 presents all three prior instrumented finger and hand manikins discussed.

Previous designs for a passive instrumented test bed for exoskeleton validation have opted against a bio-inspired design for compliance. While achieving appropriate joint stiffness, some biomechanical dexterity is lost when modeling finger joints with mechanical mechanisms.

1.2.4 RUQ Anatomy and Point-of-Care Ultrasound

Improvements in portable US technology have made POCUS a popular method in the clinical setting for quick, cost-effective medical imaging, allowing medical professionals to access patients without needing to refer them to a radiologist for a comprehensive ultrasound [52]. It is essential that practitioners have a thorough understanding of POCUS to prevent false diagnoses, and as such, trainees are expected to be well-practiced when they become practitioners. Previously, trainees were expected to perform tasks like POCUS and have been exposed to various pathologies with a traditional 'see one, do one, teach one' model, which has been shown to be insufficient [53]. Trainees needed to develop the desired skill through repetition before performing the task on a live patient.

POCUS requires a balance of multiple tasks simultaneously in the clinical setting, including performing procedures, understanding the physics and 'knobology' of the ultrasound device, providing patient care, and interpreting radiologic findings [13], [54]. As such, it

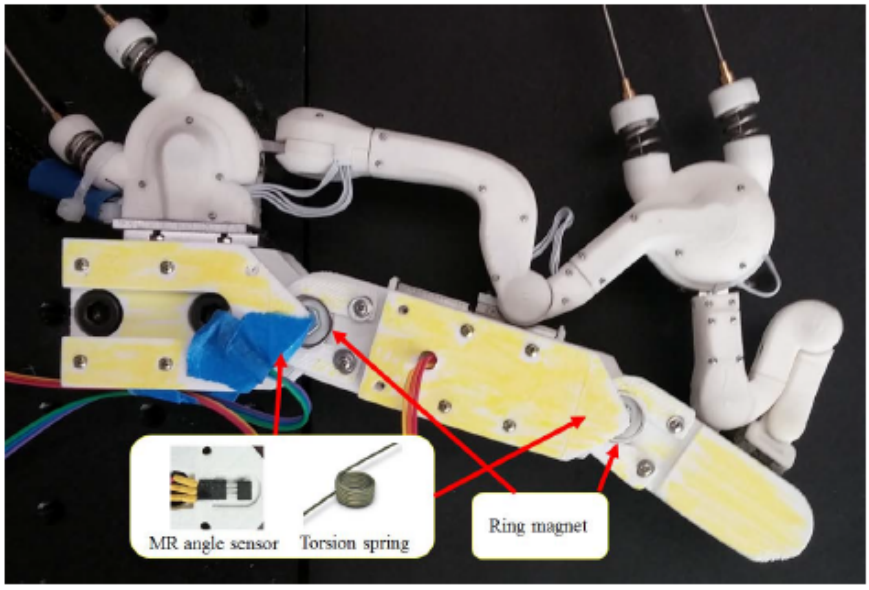

(a) Yun et al. developed a bulky finger manikin with frictionless sensing and torsion spring across joints for compliance (figure reproduced from [41])

(b) Yousaf et al. used an anthropometric model with steel springs for compliance.Hall effect sensors provide frictionless joint interaction.(figure reproduced from [51])

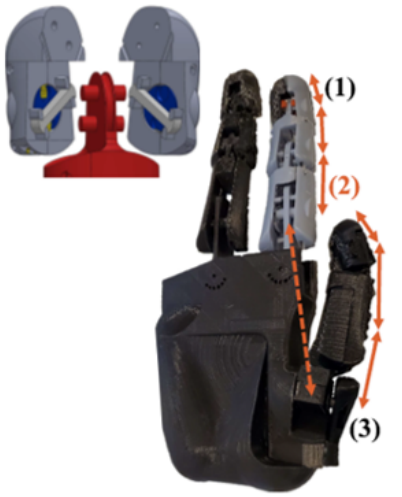

(c) Baskaran et al. produced 3D-printed anthropomorphic hand with a potentiometer for position sensing and a rubber-pulley system for joint compliance

Figure 1.11: Instrumented passive manikins for exoskeleton validation.

can be challenging for trainees to fully grasp these responsibilities through 2D visuals in a lecture-based environment. To minimize this disconnect, training programs have incorporated live patient or animal scans, cadaver scans as well as virtual and physical manikins and phantoms—training tools that simulate specific anatomy.

Cadavers have been utilized as a high-fidelity training solution, offering anatomically accurate visual and tactile experiences for trainees without compromising live patient care. The use of cadavers demands controlled environmental conditions and specialized treatment protocols to preserve tissue integrity, limiting their availability to institutions with appropriate infrastructure. Ethical concerns further complicate their use for training [4]. Simulators were sought to provide adequate training instead [4], [55]. Simulators have been virtual, physical and hybrid in their medium. Similarly, live animal scans are expensive and have similar ethical concern [56].

The key aspect of any simulator is to create a reusable device that mimics the desired properties of human tissue, enabling it to perform the intended training task. For RUQ ultrasound, virtual reality (VR) software, as well as hybrid devices, have successfully created an interactive environment in which students can scan a virtual body representation and view and record US images based on the placement of the transducer within the virtual environment. The realism and immersion of ultrasound VR experiences range from fully immersive virtual worlds to desktop screen visualization. While VR can create multiple pathologies quickly, it lacks image variability, as it is limited to the pathologies that have been programmed. In addition, virtual manikins are costly, require additional software training, lack true POCUS 'knobology' and lack in providing necessary feedback for effective student training [54], [56]. These limitations make VR simulators a helpful tool for introducing ultrasound imaging to trainees, as they have not yet provided sufficient learning experience for a cohort of advanced trainees.

Physical manikins and phantoms are valuable learning tools that provide a safer, ethical, flexible, and realistic environment for POCUS training [9], [18], [56]. They act as suitable

body replacements in comparison to infrequent live patient scan experiences can be stressful for trainees in such a time-constrained unfamiliar environment, which is not conducive to learning and hands-on training. Physical simulators have been made for a variety of procedural and imaging practices [9]. A physical manikin or phantom commercially bought can be prohibitively expensive when implemented for an entire cohort of learners [12], [13], [57]. Additionally, they are typically static in design, which limits their ability to represent a variety of pathologies within a single model [56].

Unlike virtual software, which can simulate multiple pathologies without additional hardware cost, physical models are often restricted to a fixed anatomy and a single embedded pathology, reducing their versatility in the comprehensive training of large training groups. To facilitate cohesive class training, sets of multiple units of costly manikins are often required (a set for each specific pathology to be trained), making large-scale implementation financially burdensome for educational programs [57], [58]. Hence, there is a need for an US manikin or phantom capable of interchangeable pathology for a more cost-effective solution to provide POCUS training for a large cohort. With multi-material resin 3D printers that use photopolymers, such as the Stratasys J5 DAP, fast manufacturing of various soft and hard materials for US simulation of different bodily tissues is achievable with a single printer [18]. To explore these capabilities, this study focuses on the production of a RUQ ultrasound manikin.

The RUQ ultrasound contains abdominal anatomy, involving the liver, kidney, stomach, duodenum, pancreas, gall bladder (GB), adrenal gland, large intestine, spine, ribs and abdominal and back muscles. It also includes major vessels such as the inferior vena cava (IVC), common bile duct (CBD) and aorta. Practitioners and surgeons observe the RUQ for abnormalities, including kidney stones, tumors, and gallstones, caused by diseases related to the liver, gallbladder, pancreas, or intestines, and kidneys. To become practitioners, trainees will need to master POCUS in the RUQ to identify potential issues in patients and follow

specific reference points to particular anatomies. The RUQ is a common site for US assessment due to its inclusion of critical structures such as the liver, gallbladder, right kidney, and diaphragm. The variation in echogenicity across these structures, along with frequent clinical presentations of RUQ pain, makes it an essential region for POCUS training [59].Figure 1.12 is a diagram showing the organs of the RUQ positioned in the body along with the parts of the muscular system.

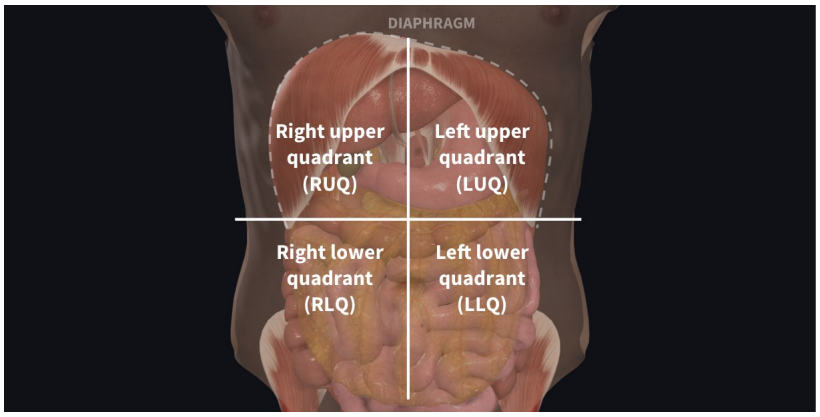

Figure 1.12: Labeled diagram showing the right upper quadrant's (RUQ) location in comparison to the rest of the body, containing organs omitting parts of the abdominal muscle for organ positions to be visual from the anterior view (figure reproduced from [60]).

1.2.5 Echogenic Properties of Human Liver and Kidney

Realistic ultrasound imaging requires that materials emulate the acoustic characteristics of human tissues to produce an appropriate echogenic response, while retaining shape and mechanical integrity [61]. Echogenicity is the term used to describe the unique ability of tissue and other bodily substances to reflect ultrasound waves, which determines their appearance on an ultrasound image. It is influenced by the tissue acoustic properties.

Kidney

The kidney is responsible for filtering excess and unwanted substances in blood to produce urine. Figure 1.13 shows a labeled diagram of the anatomical structures of a healthy kidney under ultrasound.

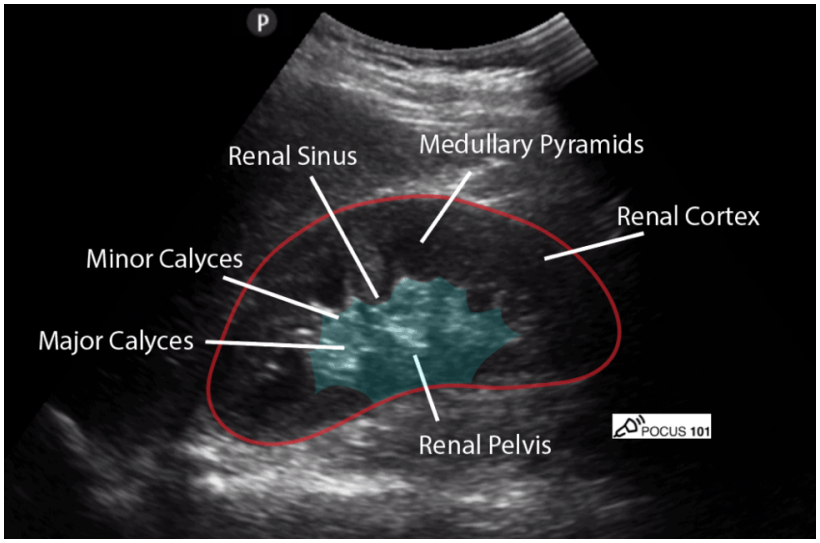

Figure 1.13: Longitudinal ultrasound image of a healthy kidney with red border outlining the organ. Internal structures display distinct echogenic properties, allowing clear differentiation of anatomical regions, such as the renal cortex, medulla, and pelvis(image reproduced from [62]).

Under ultrasound, practitioners can examine the kidney's internal structures such as the renal cortex, sinus pyramids, and pelvis. The renal sinus, as seen in Fig. 1.13, appears as a large hyperechoic area, reflecting a large amount of ultrasound waves, appearing as bright white areas on an ultrasound image- on an ultrasound image, while the renal cortex presents as hypoechoic, reflecting fewer ultrasound waves and appears as darker gray or black areas on the image. Renal pyramids are filled with fluid through which sound waves travel without interruption; this is described as anechoic. The renal pelvis without fluid is commonly isoechoic, blending in with surrounding echogenic features and does not form a distinct shape in ultrasound. Kidney stones, a widely seen abnormality, are imaged as hyperechoic image(bright under US). Other abnormalities may exhibit different echogenic properties or alter the echogenic properties of the internal kidney structures.

Liver

The liver performs a variety of essential bodily functions, among them are the synthesis of proteins, bile and enzymes, storage of multiple substances and nutrients, and detoxification. It has less complex, ultrasound-visible internal structures than the kidney, with homogeneous echogenic properties across independent vessel structures, branching to eight different areas of the liver, which break down into capillaries within the entire liver. These vessels carrying fluid show as anechoic internally with a thin hyperechoic outer layer. These branches include hepatic veins and arteries (HV and HA) as well as portal veins (PV). Liver tissue surrounding the vasculature often shows as hyperechoic when healthy, as seen in Fig. 1.14. Figure 1.14 shows a labeled diagram of healthy liver vessels and tissue under ultrasound.

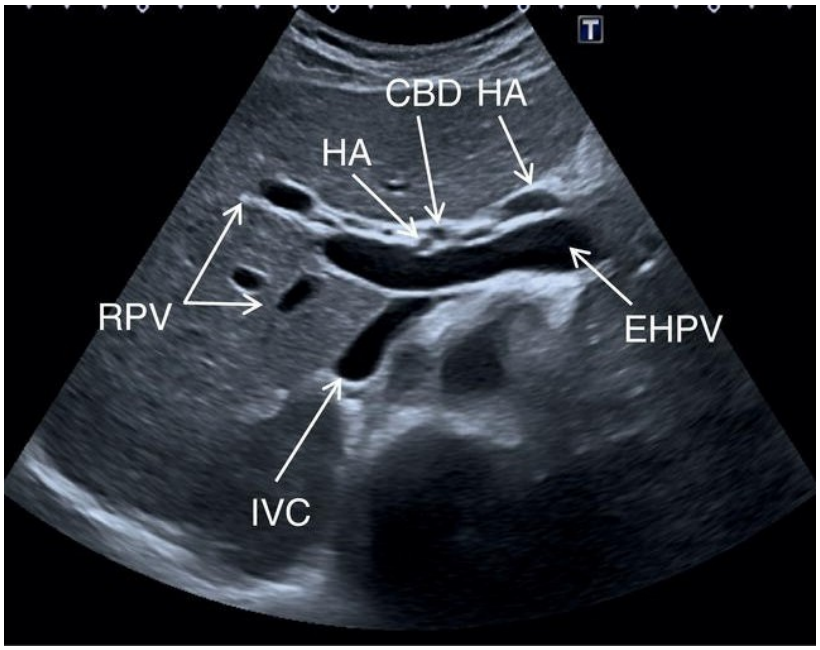

Figure 1.14: Ultrasound image of the liver at the hepatic hilum, displaying the hepatic artery (HA), common bile duct (CBD), and inferior vena cava (IVC) with visible internal vasculature. The vessels appear anechoic with hyperechoic borders surrounded by less hyperechoic liver tissue, all echogenic characteristics essential for liver ultrasound simulation.(image reproduced from [63]).

1.2.6 Review of Abdomen Phantoms and Manikins

3D-printed models for anthropomorphic organ and bodily system designs have been created by segmenting CT and MRI scans, converting them to standard tessellation language (sTL) models, and post-processing using mesh editing software for printing [4], [10]. Models have been created directly using 3D-printing or casting. Manikins and phantoms for ultrasound applications have been previously created by researchers and others sold commercially.

Models have consisted of variety of materials including hydrogels, ballistic gels, silicone, hard and soft resins, composite rubbers, agar, silicone, synthetic polymers and gelatins [13]. Although they offer soft surfaces, they lack in structural integrity, fidelity or echogenic behavior [13], [61].Researchers have gone further to chemically manipulate some of these substances with powders and oils to achieve the correct echogenicity. When these liquid or semi-liquid materials are formed, they must be cured in a negative cavity mold to achieve anatomic structure. This can become a tedious process, especially if models are required to have different pathologies. Hydrogels and synthetic gels often lack longevity, becoming dehydrated, exposed to bacteria, or lacking in structure [61]. Silicone, while providing longevity, structures, and often reusability for procedural practice, lacks the ability to create the necessary echogenicity [61]. Plastic additive manufacturing has decreased production time, increased anatomical correctness, and reduced the cost of creating ultrasound manikins.

Additive manufacturing has significantly contributed to the creation of low-cost, high-detail molds that can print whole and split models for assembly after creating anatomic models from segmenting mainly MRI or CT scans [9]. Efforts have been made to create detailed 3D-printed organ models for simulation. These models have been printed using various printing techniques, including FDM, jetting, and SLA. Many of these models are printed hollow with no internal vasculature or organ structures. Those who do strive to create anthropomorphism or a smooth surface finish cover their models with other materials [6]. Pacioni et al. [12] have made PLA models of the liver using string and epoxy to keep vascular structures together within an outer organ shell. These models were not designed

for ultrasound, and internal structures would not be visible on a scan. Researchers have developed large, multi-material manikins that incorporate molded and 3D-printed models of whole organs, abdominal zones, and the entire abdomen.

However, these models are made of hard or rubber-like materials, lacking in anthropomorphism and echogenicity. Hernandez-Torres et al. [64] made an ultrasound manikin with abdominal organs, including a few in the RUQ, but used ballistic gel and other gel materials to form models. They used air bubbles in the cast to produce anechoic regions, previously achieved with liquid-filled balloons. These models were only able to create hyperechoic organ borders, but not internal structures. Gear et al. [65] used the Stratasys Connex3 Printer to create an anthropomorphic modular unit for radiation image training. The manikin consisted of models of the lungs and liver. Minor changes to the Stratasys Connex3 printed body with the addition of fluid-filled ball mechanisms, simulating tumors, that can be placed at different pre-determined positions. The Stratasys Connex3 created soft models by mixing rubber-like material with hard material for a radiation manikin. Although the manikin was created using a single printer that can print multiple materials simultaneously, the Stratasys Connex3 printer prints dense resin materials that may not accurately represent soft tissue under ultrasound, similar to PLA or silicone.

In addition to the lack of echogenicity among 3D-printed manikins, they also lack high modularity. Commercial ultrasound manikins and phantoms for simulating abdominal pathology,such as the example in Fig. 1.15A, are not suitable for large training groups, due to their inability to change specific pathology. Anwari et al. [4] have presented a multi-material mannequin for X-ray training,as seen in Fig. 1.15B. This comprised of 3D-printed shells that were filled with gel-like materials to achieve the desired radiological accuracy. The liver was assembled by combining 3 shells, with one of them having a vascular structure attached to it. The kidney's cortex and calyces were modeled. They were able to capture internal organ features using X-ray imaging. The manikin had an open abdominal space in its polycarbonate holding for access to organs for replacement. Organs were held together

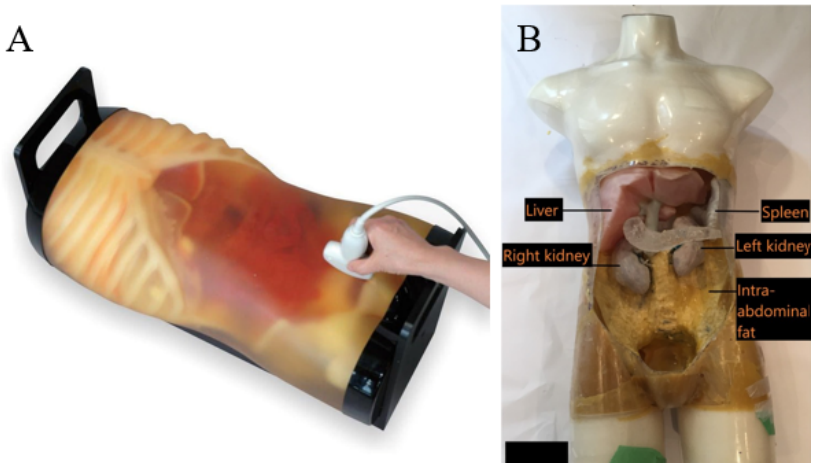

Figure 1.15: (A) Commercial ultrasound manikin for abdominal pathology training lacks modularity, making large cohort training costly(figure reproduced from [66]). (B) Anwari et al. X-ray manikin with modular organ inserts was made from a variety of materials, which demonstrated radiological accuracy but used gel-filled 3D-printed shells unsuitable for efficiently obtaining anatomical fidelity and US compliance(figure reproduced from [4]).

using a mixture of beeswax, olive oil, and lanolin to create a low-melting-point material that was radiologically accurate and facilitated easy removal of organs. Hence, there is a need for a low-cost, high-detail, and modular ultrasound manikin that accounts for internal organ structures for ultrasound training, particularly POCUS.

1.3 Stratasys J5 Digital Anatomy Printer

The J5 DAP is a jetting printer that sprays small droplets of photopolymers, in this case resin, which are subsequently cured using ultraviolet (UV) light [6]. The J5 DAP, developed to enhance the tactile fidelity of anatomical models, is capable of producing high-resolution prints with smooth surface finishes, achieving a reported layer resolution as fine as 18 mum [17].

The DAP uses 3 print heads to spray resin onto a round plate that spins during print to facilitate the cyclic process of laying and curing to be done per layer. Jet printers can spray multiple materials simultaneously in varying quantities [6]. This enabled the creation of unique materials to fulfill specific purposes and represent different tissue properties. The

printer uses biocompatible resin materials capable of producing soft, hard and elastic materials depending on the raw resin materials used to form the printed material. Stratasys has named these raw resin materials: BoneMatrix (hard), TissueMatrix (soft), DraftWhite (hard), GelMatrix (gel-like), and ElasticoClear (rubber-like) [17]. Support, removable by a waterjet, is used in areas that need structural assistance when forming the entire model.

Jet-resin material can be more expensive compared to silicone materials that produce similar anthropomorphism when molded. However, to meet desired echogenicity, other substances or powders must be added in specific ratios [12], [15], [61]. This process can be eliminated with PolyJet printers like the J5 DAP.

1.3.1 Advantages of Polyjet Printing

The J5 DAP's capability to mix resin materials to print new materials is an advantageous print technique in creating echogenic models. FDM printing techniques have been used for direct and indirect anthropomorphic phantom modeling. FDM printers extrude melted filaments through a nozzle layer by layer to form models. Designers have created cost-effective models using PLA ABS, and TPU as models and molds [13], [15]. FDM-printed models, while viable structurally, often do not meet the required radiology requirements as the limited number of compatible materials aren't capable of diverse material properties. FDM prints are used as molds or filled with materials that can create accurate radiological features [2]. Biomaterial FDM printing has been investigated on small scales, printing hard and soft tissue but is in its beginning stages. Bioprinting lays synthetic or grown tissue to form layers of a complete model. While ideal for creating an anthropomorphic material, it has not been developed for large organs with bonding issues between layers [9]. Other printing options like SLA, used in medical 3D-printing, can print soft resin prints like the J5 DAP, but can only print one material at a time and often require a bath for printing. Other jetting printers, like the Stratasys Connex3, have been used for anatomical modeling [37], [65], [67]. However, Stratasys Connex3 would not be capable of jetting soft materials with hypoechoic

attributes as it only prints hard and rubber-like materials for anthropomorphic modeling. The J5 DAP has softer gel-like photopolymers capable of manufacturing novel anatomical models and manikins which allowed for soft and hard tissue mimicry through multi-material jetting technology. The ability to produce these components on a single printer—without the need for molding—enables more realistic, bio-comparable interfaces between tissue types.

1.3.2 Applications

The J5 DAP and adjacent polyjet printers have manufactured compliant anthropomorphic models with both tactile and visual aesthetics. Polyjet printers have been used in both compliant joint design as well as echogenic organ model design. Stratasys Connex3 was used to create an anthropomorphic finger for an active robot model using hard Verowhite and rubber-like TangoBlack materials [37]. Sparks et al. [7] captured and accessed ultrasound images of a soft vessel wall model created with another polyjet medical printer to determine its compliance by measuring its distensibility during fluid flow. Stratasys, along with Creighton University, developed a breast manikin for tumor detection with the J5 DAP that showed expected tissue echogenic properties [68]. Kamalinia et al. [18] investigated a numerical method for evaluating the microstructure of a polyjet print material to understand the scope of its use in ultrasound imaging.

1.3.3 Limitations

Polyjet printing, however, is limited by the available material, the cost of the material, and the build tray size. All of which the J5 DAP has fell short, only able to print 5 costly materials with a build tray only a few full-scale organs could fit on. Unlike other methods of 3D-printing, the J5 DAP offers variety in resin 3D-printing that compares to the variety in tissue properties in the body. With its extensive material options and structural capabilities, it can support a wide range of simulation applications in a single printer. With such a large

possibility of combinations between 5 materials, the J5 DAP's potential in creating full-scale manikins and models for mimicking desired tissue properties has not been discussed.

1.4 Contributions and Thesis Outline

Anthropomorphic models serve as practical tools for simulating high-risk scenarios, providing a safe and repeatable environment in which users can develop and refine their skills. These models reduce the likelihood of error while enhancing user familiarity and proficiency in complex, high-stakes settings. This thesis focuses on simulating finger biomechanics and RUQ ultrasonography to address the needs of hand exoskeleton designers and POCUS trainees, ensuring no harm is done to humans. Leveraging the high-fidelity capabilities of the J5 DAP, this work investigates the underutilized potential of polyjet printing—specifically, its ability to generate variable material compositions tailored for model compliance. The thesis presents detailed methodologies for designing and fabricating anatomically accurate, compliant models, including the mechanical evaluation of 3D-printed soft materials for replicating liver and kidney anatomy for US simulation, as well as a passive PIP joint for biomechanical simulation. These contributions provide model developers in medicine and rehabilitation with a rapid manufacturing approach for producing anatomically correct, compliant simulator and future optimization in material mechanical performance.

The J5 DAP is capable of printing ligament, tendon, and bone structures, as well as soft skin for glove fit, in one print with material combinations that emulate the compliance and structural properties of both soft and hard tissue. To investigate the potential of soft 3D-printed materials for creating anatomically realistic finger joints, this study aimed to answer the research question: Can J5 DAP accurately simulate a passive finger anatomy and biomechanics from a MRI-generated anatomical model for compliance and whether void-infused soft material affects material elastic properties for a potential methodology for achieving compliance? Addressing this question contributes to advancing the state of the

art in exoskeleton evaluation and design. This approach would enable future designers to rapidly manufacture patient-specific models for further exoskeleton controls customization.

For the development of an ultrasound training manikin as a high-fidelity practice tool, all relevant anatomical features must be realistically simulated to replicate the echogenicity of real human tissues. In this thesis, the focus is on simulating anatomy related to the liver and kidney to assess the viability of soft 3D-printed materials produced by the J5 DAP for replicating RUQ tissues in an ultrasound manikin. This study aims to present an effective method for generating RUQ anatomical models from medical imaging data and to characterize the echogenic properties of J5 DAP materials. The goal is to establish a standardized approach for evaluating and comparing these materials to real liver and kidney tissue to support their use in RUQ ultrasound simulation.

This thesis outlines and validates methodologies for the creation of anatomically correct anthropomorphic models from medical images for both a medical and a rehabilitation simulator using the Stratasys J5 DAP and FDM Printers. FDM printers were used for material property adaptation technique validation and model filling for non-compliant parts of simulators while the J5 DAP was used to create the compliant models.

In Chapter 2, anthropomorphic model development for the creation of a compliant passive anthropomorphic hand manikin capable of simulating biomechanical joint stiffness of the PIP joint was investigated with the use of J5 DAP and FDM 3D-prints and techniques. Methodologies for the creation of a passive instrumented hand model with internal anatomically correct structures derived from medical images were proposed and validated through printing. The model is to be integrated with sensor technology to validate and test the position and torque of a hand exoskeleton.Evidence to support the use of void-infused soft material as a method for creating compliant ligament structure was presented by altering void parameters, which affected the elastic properties of a soft elastic TPU.

Chapter 3 investigated the use of a soft, 3D-printed gel-like material, the J5 DAP, for creating ultrasound-compliant models and proposed a methodology for rapidly and

cost-effectively developing anatomically correct RUQ models with internal liver and kidney anatomy that simulates RUQ POCUS training.

These two applications of additively manufactured anthropomorphic manikins required key methods and tools that led to compliant model creation on the J5 DAP. Chapter 4 summarizes the principal findings of the study and proposes directions for future work.

Chapter 2

Passive Anthropomorphic Hand Model

2.1 Introduction

The human hand is a key instrument in facilitating human interaction with their environment. This interactive experience can be dampened by neuromuscular injuries or disorders of the hand, as seen in stroke patients who have limited upper extremity motor functions [69]. Soft hand exoskeletons have been proposed to assist and rehabilitate hand function due to their capabilities for compliant and comfortable wearability [70]. This compliant behavior is created from passive components through inherent stiffness and damping in the exoskeleton design, along with active supply of controllable torques about the patient's joints to generate a kinematic haptic experience within the patient's ROM.

Designers of wearable robots must validate the torque and position controls implemented in their wearable robots to create the most comfortable and stable haptic experience. Often designers use themselves to test and validate their exoskeletons. Others have also used small participant populations or static manikins for validation [19]. This can lead to undesired validation results due to unforeseen complications in exoskeleton control model, the inability of a static manikin to produce viable dynamic data or difficulty in using current motion tracking devices to capture joint movement of the human hand from within the wearable robot. The construction of a passive, anthropometric instrumented manikin would aid in solving these problems [19], [34], [41], [51], with a sensor to determine the motion of each joint. Access to an efficiently manufactured, cost-effective design of a passive manikin will not only provide a more accurate validation of exoskeleton movement but also present the possibility for designers to readily use different hands for validation, such as a male hand against a female hand. This leads to more controlled and generalizable exoskeleton designs

being created in shorter periods of time with increased access to the design tool over the current practice.

While these solutions exist, a passive instrumented anthropomorphic hand model with anthropomorphic tissue structures can lead to higher biomechanical accuracy for validating the kinematic and dynamic behavior of these exoskeletons. With a high-fidelity patient-specific maninikin, exoskeleton designers could generate more patient-specific controls with less risk of patient or designer harm. In pursuit of such the instrumented anthropomorphic model, this thesis proposes a method for developing a PIP joint with the desired passive joint stiffness, made using Stratasys J5 DAP derived from Magnetic Resonance Imaging (MRI). Polyjet printing of a hand model enables continuity between modeled anatomy and a variety of materials, providing compliance in comparison to the state of the art, which requires detailed assemblies. A compliant, dexterous, and anthropomorphic hand model produced through single-printer 3D-printing, with integrated position sensing, would offer a streamlined and manufacturable platform for exoskeleton validation—marking a significant improvement over current instrumented joint models.

This chapter investigates the use of an anatomical PIP joint model of the index finger, derived from MRI data and 3D-printed using the J5 DAP to achieve high anatomical fidelity. The compliance of the joint model, with stiffness simulated using J5 DAP soft tissue materials, was evaluated, along with void-infused soft materials as two approaches to achieve desired biomechanical performance. Figure 2.1 demonstrates the proposed methodology for creating anatomic structures to represent the CLC for the creation of an instrumented anthropomorphic joint model and eventually an instrumented hand. For compliance, this study investigates the intentional infusion of voids in soft 3D-printed material as a method for varying the elastic properties of 3D-printed material by varying void parameters using TPU. This method is intended for use with soft materials designated to create compliant joint stiffness in the proposed joint model.

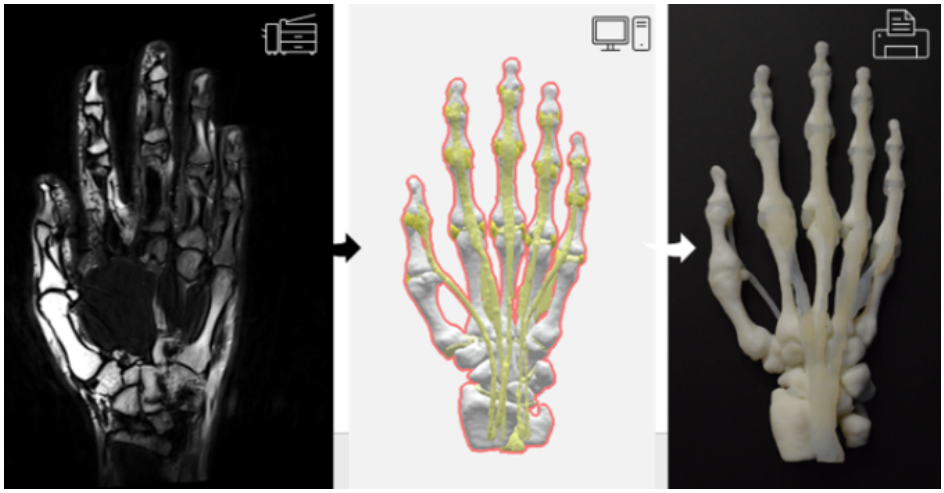

Figure 2.1: Methodology for developing anthropomorphic structures for the creation of an instrumented anthropomorphic hand beginning with magnetic resonance imaging (MRI) of hand to digital 3D representation of the bone, tendon and ligament structures in the hand and lastly, an anatomical 3D-printed model of the hand.

2.2 Development of Anatomical Hand and PIP Joint Models for Biomechanical Simulation

2.2.1 Model Reference for Anatomic Geometry

There are two primary options for creating anatomic models of the hand: indirectly by matching gross anthropometry [25], [34], [51], or directly by deriving models from imaging of the hand [3], [29], [37], such as a laser point scan of a cadaver or a MRI. A laser-scanned model does not allow for anatomical soft tissue modeling; therefore, models derived from medical images present the opportunity for anatomically correct anthropomorphic joint modeling with desired biomechanical properties for improved dexterity. The structural detail and complexity of muscles, bones, ligaments, and other tissues can be better preserved, enabling more accurate representation of anatomical volumes and curvatures. This improved fidelity enhances force transmission and kinematic interactions within joints, allowing for more precisely modeled joints with anatomically accurate shapes and appropriate thicknesses in ligament and tendon structures. It is expected that high-fidelity modeling will improve the modeling of joint stiffness along respective movement axes naturally created

within each joint.For the development of an anthropomorphic, instrumented hand manikin to validate exoskeletons, these features enable dexterous movement that closely replicates human biomechanics while allowing for the integration of sensors to accurately measure joint motion.

Researchers have utilized models generated from point clouds from the laser scan of a hand cadaver in their efforts to create anatomically accurate models [4], [29]. Stratasys has developed a notable model used for joint interaction [71]. While this model is suitable for printing, it lacks detailed joint interactions, with bones adjoined at joints and ligament structures. Early versions of the model used for anthropomorphic design only consisted of bones in the hand, not suitable for direct mimicry of soft tissue morphologies [3], [5], [28]. In addition, the Stratasys model does not accommodate future works in patient-specific modeling. Creating an electronics-infused anthropomorphic manikin will enable exoskeleton designers to test and validate the position and torque of patient-specific exoskeletons using a high-detail simulator, eliminating the need for consistent patient participation and potential discomfort.

With this in mind, a medical imaging approach was taken to create a hand model for this device. Medical Imaging is a vast and growing industry, as machines are capable of producing high-resolution internal images without physically penetrating the scanned area and filtering out distortions caused by the movement of the patient or machine. A CT or MRI scan can be used to create a contrasted image of the internal structures of the hand. These two scans are best suited due to their ability to show high-resolution contrasted imaging of multiple tissue types, unlike ultrasonics and X-rays. Ultrasounds tend to produce lower-resolution images, while X-rays, often used for bone imaging, are single shots of a chosen dimension of the body. Both are not conducive to creating accurate 3D-Models of the entire hand.

CT scans utilize multiple X-rays taken from various angles around the body, which are directed to a detector or receiver to generate a series of high-resolution image slices that accurately represent internal anatomical structures. While CT scans create high-resolution

images that are useful for making detailed models, access to CT scans is limited, as they are often performed only in extreme situations due to the high levels of radiation exposure and are not typically used for hand-related or non-medical purposes. Since CT scans involve ionizing radiation, they are not considered an ethical choice for imaging in this context. The next alternative, given current technology, is MRI. MRI uses a strong magnetic field to align hydrogen atoms in the body. As radio-frequency pulses pass through the body, they interact with these atoms, generating signals that are converted into high-contrast images of internal structures. Unlike ionizing radiation, magnetic and radio waves used in MRI are not harmful to the body. MRI provides high-resolution images that differentiate between hard and soft tissues, making it a suitable modality for constructing a biomimetic model of the hand.

Although open-source MRI scans are available, they are frequently compressed or converted into file formats incompatible with segmentation and 3D reconstruction software to minimize file size, limiting their direct usability for anatomical model generation [72], [73]. Scan visualization software requires a DICOM file type. DICOM files store scan information along with the image such as order, orientation and scan type of the images in comparison to other commonly used image file types. Due to the lack of open-source images meeting the required specifications, it was necessary to obtain a custom MRI.

Auburn University MRI Research Center was able to accommodate a MR scan of the right hand of a healthy adult male with no deficiencies or prior hand injuries. The center's Siemens 3-Tesla Scanner, seen in Fig. 2.2, was used to produce the MR images. The subject's hand was placed in a hand coil, seen in Fig. 2.3A, to reduce movement and obtain high-resolution images of the hand. Images were obtained using T1-weighted and T2-weighted scan sequences with a slice thickness of 1 mm to achieve optimal contrast between tissues in the hand, facilitating the creation of distinct boundaries for 3D modeling of anatomic features in the hand. A clear image is essential for defining the anatomic feature boundaries during 3D model generation. MR image clarity is heavily dependent on patient movement. The slight movement can cause noise in the image, commonly known as "ghosting," which

Figure 2.2: MRI scans are used to gather high resolution imaging of soft and hard tissue. Stillness is required to develop sharp images.

results in blurry white lines that reduce image sharpness. Lower resolution can create high-quality images, but requires ideal conditions. While smaller image slices were achievable for higher precision with the 3T scanner, 1 mm was chosen for the best quality image, thereby avoiding undesired noise in the images.

MR Images along orthogonal sagittal, transverse and longitudinal axes captured the desired shape and curvatures of the four long bones within the hand to be modeled, as well as ligament and tendon structures. Figure 2.3B and Fig. 2.3C show the coronal and sagittal views, respectively, of the MRI scans collected along with the hand, in a pronate position, in the hand coil used to generate the MR images.

MRI has shown to be a solution for imaging patient-specific hand features with desired anatomy for an anatomically accurate passive hand model present in scan. To convert these medical images into 3D models, they were segmented using available software capable of converting the 2D segmented feature boundaries into a 3D representation.

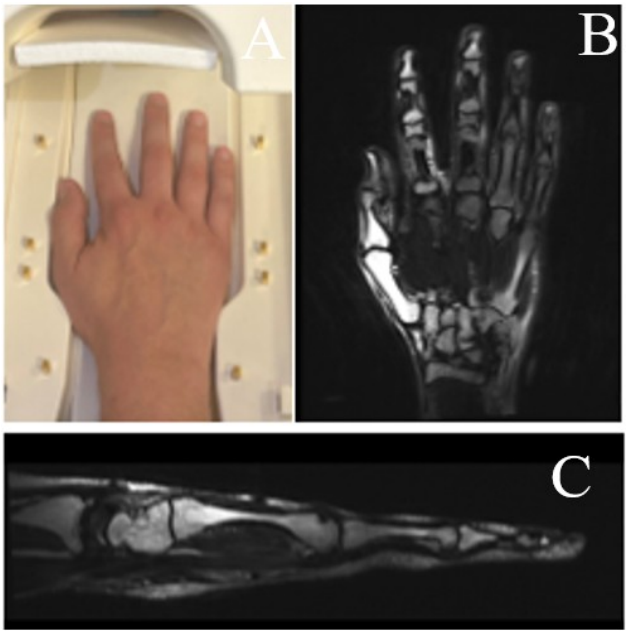

Figure 2.3: Figure 2.3A shows the participant's hand in a hand coil used to provide support and enhance clear imaging of the hand under MRI. Bone, tendon, ligaments, and muscle are all visible under MRI, as well as the hand structure. Figure 2.3B shows a MRI of the hand in the pronate position. Figure 2.3C shows the lateral plane view of the MRI image. The images are used to create digital 3D models of anatomy.

MR Images along orthogonal sagittal, transverse and longitudinal axes captured the desired shape and curvatures of the four long bones within the hand to be modeled, as well as ligament and tendon structures. Figure 2.3B and Fig. 2.3C show the coronal and sagittal views, respectively, of the MRI scans collected along with the hand, in a pronate position, in the hand coil used to generate the MR images. MRI has shown to be a solution for imaging patient-specific hand features with desired anatomy for an anatomically accurate passive hand model present in scan. To convert these medical images into 3D models, they were segmented using available software capable of converting the 2D segmented feature boundaries into a 3D representation.

2.2.2 Anatomically-Correct 3D Model Generation

Segmentation is a commonly used process to identify features in a medical image on any scan plan. It includes identifying and outlining the boundaries of specific anatomic features

within scan images. Software for converting medical images to 3D models generates 3D models by giving the marked region in all 3 orthogonal planes to create a volume. This process can be very tedious and time-consuming [9]. However, auto-segmentation algorithms enable rapid segmentation of anatomy. Additionally, some automatic segmentation algorithms utilize image recognition trained on previously segmented medical images, as well as intensity tracking, which segments areas with a similar contrast level. Image recognition algorithms can identify specific anatomy, reducing the need for knowledge of hand anatomy and radiology to accurately identify anatomic feature boundaries in MRI scans. These algorithms enable efficient and consistent identification of complex anatomical structures. Software such as OsriX, Meshlab, ITK-SNAP and 3DSlicer are open-source software frequently used for segmenting medical images for model generation and are viable programs to segment required hand anatomy for 3D modeling.

To convert the MRI scan into 3D models for additive manufacturing, DICOM files generated by the scanner were uploaded into 3DSlicer. 3D Slicer was selected for its auto-segmentation features, user-friendly interface, and widespread use in medical imaging research [74]. After assessing the capabilities of 3DSlicer for hand segmentation, it was decided that 3DSlicer's auto-segmentation extensions and tools were inefficient for fast segmentation of desired bone, ligament, and tendon structures. The open-software struggled to auto-segment detailed thin structures such as the CLC, as well as the extensor and flexor tendons and proved labor-intensive. However, the software was able to fast segment the external morphology and bulk internal volume of the hand.

Open-source software struggled to auto-segment detailed thin structures such as the CLC, as well as the extensor and flexor tendons, Since segmenting is not the primary focus of the study, alternative avenues for auto-segmenting hand scans were explored. To address this limitation in open-source software, Axial3D was consulted to assist with the segmentation of these intricate features from the MRI scan. Axial3D [75] allows customers to define desired anatomic features from a scan they obtained and, for a cost, provides physical 3D prints, 3D

digital displays or 3D-printed files. The international medical modeling company employs proprietary algorithms that can rapidly segment anatomy, with a 48-hour model generation policy.

AI-Driven Automated Segmentation: Axial3D

There are several avenues available for preforming rapid segmentation. Open-source software, 3DSlicer has available extensions or built-in tools that can run auto-segmentation algorithms on images. These algorithms were inefficient for hand model generation, most likely due to the complexity in its thin and small volume structures. Licenses were required to gain access to algorithms that would produce only bone structures in the hand. This is most likely due to low number of studies devoted to modeling highly detailed hand models from medical imaging. Commercial entities use proprietary algorithms to create models for customers that provide the scan for conversion.

Axial 3D uses proprietary AI models to create detailed anatomic models within 48 hours. Axial 3D was used to generate STL files with 3D models of hand anatomy, assembled in Figure 2.4A, based on the acquired MRI scan using their proprietary automated segmentation machine learning algorithm for fast scan-to-model generation. Axial 3D provided the composite of anatomic models for $500, which may be considered costly but reduces the time taken to generate segments. Figure 2.4B and Figure 2.4C show images of Axial3D segmentation in the sagittal and axial views as well as the generated 3D display from segmentation results.

2.3 Manufacturing and Assesment of 3D-Printed Anatomical Hand and PIP Joint Models with J5 DAP for Biomechanical Simulation

2.3.1 Preparation and Manufacturing of 3D Print on J5 DAP

A 3D print, shown in Fig. 2.5, of the digital 3D hand model provided by Axial3D was fabricated using a Stratasys J5 DAP. The J5 is able to print complex anatomical structures

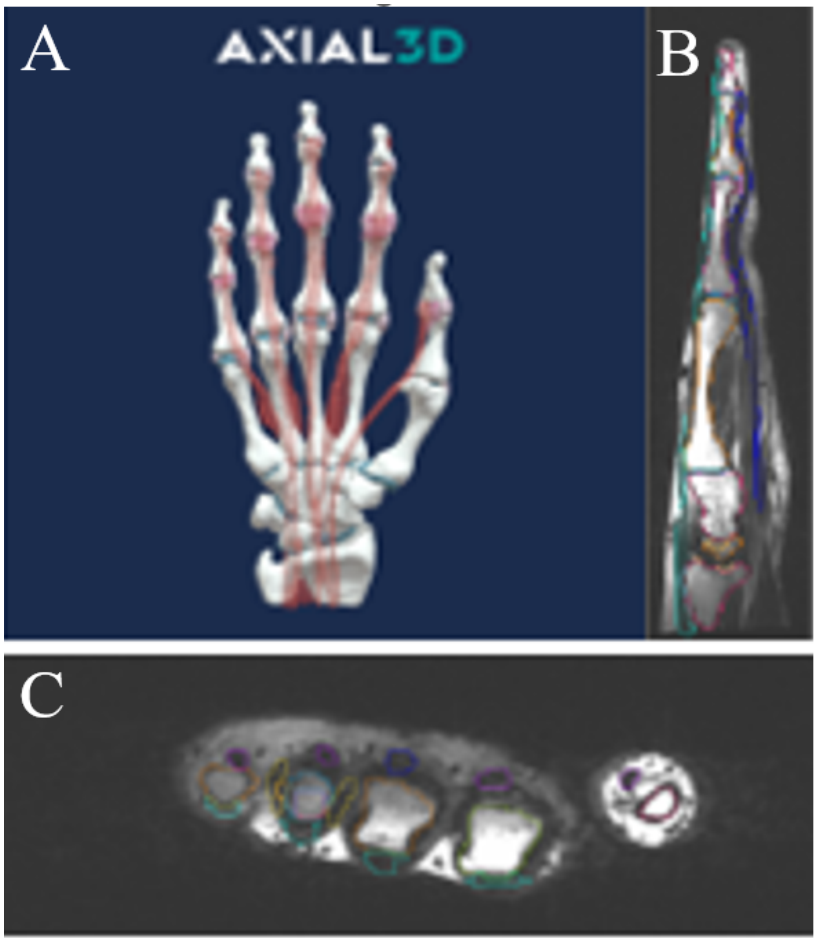

Figure 2.4: Axial3D uses image segmentation to produce digital 3D model of bones, ligaments and tendons.Figure 2.4A is a digital 3D hand model in a supine orientation presented in the top left. Segmentation process done by Axial3D with provided MRI with figure 2.4B being the sagittal view of the process and Figure 2.4C being the axial view.

with different components of different materials, achieving a clean finish in a single print, which is an asset in the quest to determine an efficiently-manufactured, cost-effective passive instrumented hand model. GrabCAD software is used with the J5 DAP to repair, prepare, asign material and orient files for printing. The J5 DAP has preset material mixes designated to represent specific anatomies best. Different types of bones, organs, blood vessels, and musculoskeletal tissues were presented by Stratasys to have hardness properties similar to the tissue it aspired to replicate [17]. For the printed hand, the preset long bone was used with the miniature type for small bones like the phalanges, with a small medullary cavity. This setting places softer material on the inside of bone models to represent the cavity with a hard outer shell similar to internal bone anatomy. For soft tissue representation, the compliant ligament preset was used to represent ligaments and soft connective tissue for tendon structures. The print took approximately 12 hours to complete printing and print supports were removed with a water-jet to obtain the product in Fig. 2.5.

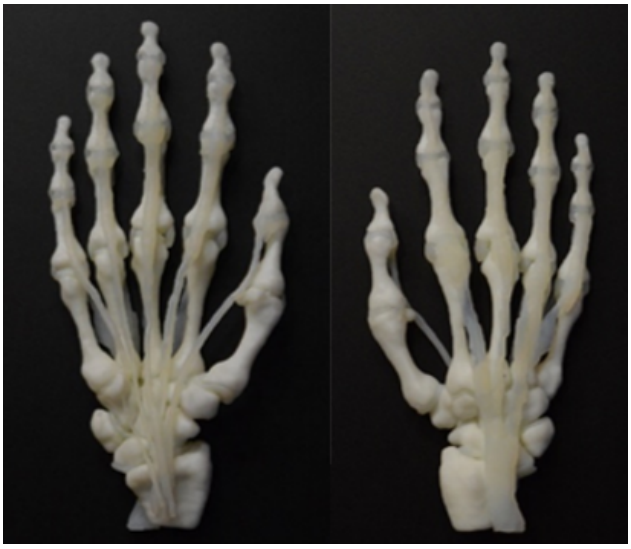

Figure 2.5: Stratasys J5 Digital Anatomy Printer used to print anatomic 3D model of bones, ligaments and tendons in the hand. Hand A is the 3D print of the hand in the supine position and hand B is the same hand in the pronate position.

For a model with higher fidelity, a method that combines AI-based fast segmentation algorithms with human revision would improve model anthropomorphism. With 3DSlicer's Python extension, users have the ability to run developed algorithms on medical images and

produce 3D models. A commercially obtained model or an open-source AI segmentation algorithm can be used to generate bulk anatomical morphologies, serving as a foundation for more detailed modeling. Tools in 3D Slicer or other open-source segmentation software can then be employed to enhance model fidelity by isolating finer anatomical features.

This two-step approach is believed to improve anatomical accuracy, which in turn supports more realistic kinematic behavior in simulation models. Currently, a proportional relationship exists between the time invested and the anatomical accuracy achievable when segmenting 3D models from MRI data. High-fidelity hand segmentation often comes at a financial cost, as it relies on proprietary software or services offered by commercial providers. In contrast, while open-source platforms provide a cost-effective alternative, they typically demand significantly more manual effort and time to produce a similar result.

2.3.2 Assessment of 3D-printed on J5 DAP for biomechanical simulation

The resulting models accurately represented all target bones as separate structures, maintaining realistic joint articulation geometry for joint interface accuracy. Generated models also included desired soft tissue models for passive anthropomorphic hand modeling, namely the flexor and extensor tendons as well as the volar and collateral ligaments for the PIP and DIP of the index and middle finger. Figure 2.6 shows a labeled model of the printed hand with volar and collateral ligaments as well as flexor tendon models for the PIP joint.

While soft tissue structures were present in the printed model as generated by an AI algorithm, the extensor-flexor tendons and volar ligaments lacked anatomical fidelity for the index finger. In vivo, tendons are capable of gliding along bone surfaces when actuated by muscle, allowing natural joint movement. However, in this model, tendons were rigidly fixed across the joint, restricting their mobility. Furthermore, key ligamentous structures in other regions of the hand, such as those in the thumb, were not represented. Despite these limitations, the model included soft tissue structures spanning the PIP joint of the index finger on the volar, dorsal, and lateral aspects, with restriction in the proximal direction. This

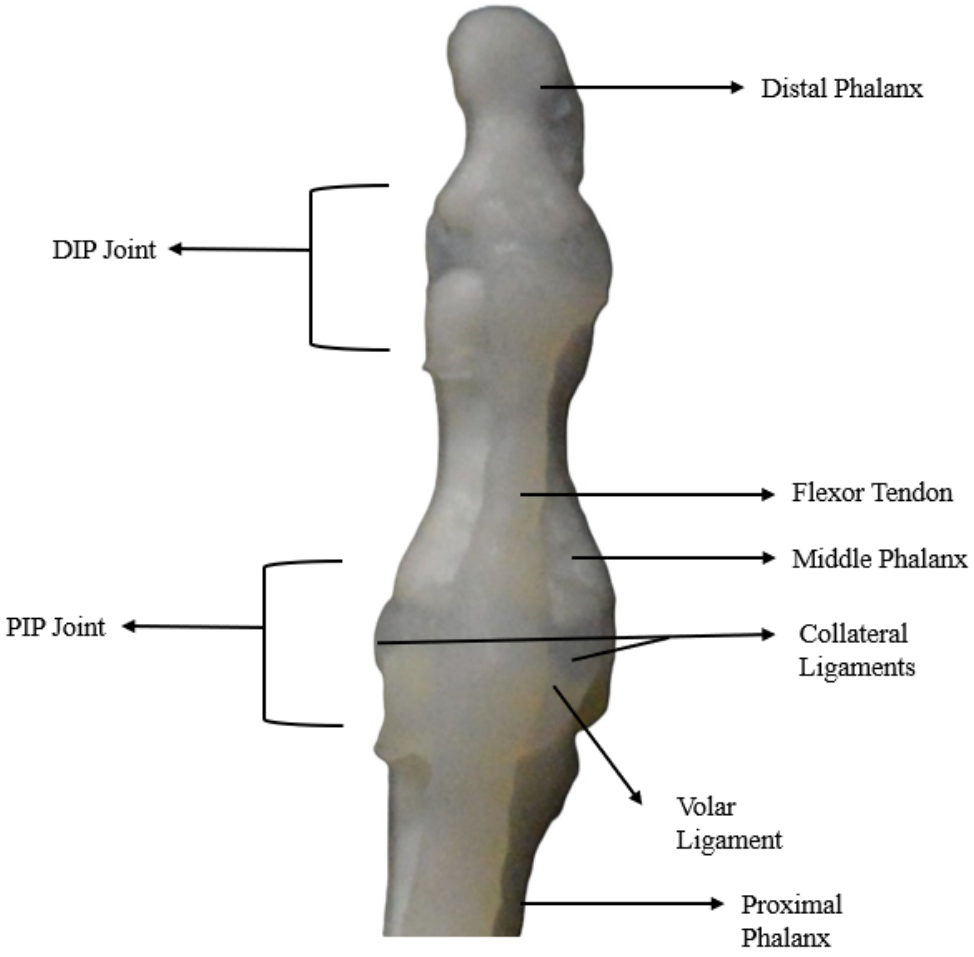

Figure 2.6: Labeled 3D-printed model of index finger anatomy, generated by Axial3D from a MRI scan and printed in a single run using the J5 Digital Anatomy Printer. The model combines soft materials to represent soft tissues and hard materials for bone structures. It includes detailed representations of finger joint ligaments and flexor and extensor tendons, designed to support passive finger movement modeling.

anatomical representation creates a joint capsule that enables constrained DOFs for expected passive stiffness conditions, making it suitable for passive biomechanical simulation.

After printing, it was observed that the hand was flexible at the index PIP joint, and the soft elastic material surrounding the joint was capable of elastic deformation, returning the hand to its original position after a maximum of 1 kg weight was loaded and unloaded 1.5 cm from the joint on a secured finger, eliminating other joint influences. Joint angle was measured with a goniometer as a reference.

The PIP joint in the index finger of the 3D-printed model was capable of flexion and extension movement, but did not achieve the expected PIP joint ROM before breaking anatomical features. Passive constraints for simulating the PIP joint of the index finger are expected to allow a ROM of approximately 110° in flexion and 0° in extension from a flat palm position [76]. An assessment of the 3D-printed PIP joint revealed a maximum flexion angle of approximately 57°, indicating a substantial reduction in ROM compared to the expected anatomical ROM. The hand model was flexed until initial signs of tearing were observed at the PIP joint, at which point the joint angle was measured using a goniometer for reference. The joint also experienced over 0 ° in extension without reaching failure. These observations suggest that to meet biomechanical performance requirements, the soft tissue material must exhibit increased stiffness and higher elongation before failure, or the joint must incorporate a stronger material interface to withstand the mechanical demands of flexion.

The J5 DAP soft ligament and connective tissue materials were insufficient in achieving desired properties for biomechanical accuracy in the developed anatomical PIP joint model. It was determined that the compliant ligament tissue preset, used for ligament models, only uses ElasticoClear material. A stiffer material can be created by adding a percentage of rigid materials to the original material to increase material stiffness, which is possible with Stratasys' Digital Anatomy Creator (DAC) [77]. With this software, the rigidity of the materials and properties of internal print structures can be tuned to obtain a compliant print

material. This feature allows for variation in material composition across individual print layers, along the part's longitudinal axis, and radially from the surface inward. This feature would allow for the creation of improved rigid and soft material interfaces similar to anatomy, where a transition from rigid bone structure to collagen fibers takes place. However, this feature can be costly(<$3,750/year); hence, a repeatable, cost-effective method for achieving compliance is desired to enable manikin designers. Void-infused materials are believed to impact material elastic properties [78]. This study investigates the use of void-infused soft materials as a method for manipulating material elastic properties in section 2.4.

For glove interaction and a complete anthropomorphic hand model, a combination of the external hand model generated with 3DSlicer and Axial3D's intrinsic models is to be printed with soft materials similar to the hardness of skin and subcutaneous fat. A digital model of this combination is presented in Fig. 2.7.

Figure 2.7: Axial 3D's hand model printed with the J5 Digital Anatomy Printer is depicted on the left, and the corresponding digital representation of the external morphology of the hand derived from the same MRI scan generated in 3DSlicer is presented on the right.

2.3.3 Summary of Development of Anatomical Hand Model

The methodology presented provides a foundation for creating anatomical 3D-printed joint model structure from a MRI scan for use in a passive, instrumented manikin. Current instrumented hands do not utilize internal anatomic features for joint design [34], [51], whereas non-instrumented hands tend to employ 3D models with low anatomic resolution derived from laser-scanned cadavers [5], [37]. Preliminary observations of the model print show that anatomical features can be modeled. However, some manipulation of the CLC structure of the print will have to be undertaken to achieve compliance. Void-Infused soft material is a potential method for manipulating material elastic properties. For anthropomorphic external appeal and validation of exoskeletons, a flexible, low-stiffness external hand model is to be printed and placed over the assessed model. A 3D CAD representation of the external hand model was generated with 3Dslicer from MRI.

2.4 Elastic Property Variation via Void-Patterned TPU for Joint Stiffness Simulation

Soft 3D-printed materials require validation of their elastic properties to achieve compliant joint stiffness in a 3D-printed finger model. 3D-printed soft materials often exhibit homogeneous properties; however, human ligament tissue is heterogeneous, comprising several different types of collagen fibers. A method for manipulating the properties of 3D-printed materials to simulate heterogeneous properties in ligaments is desired to overcome the constraints of soft 3D-printed materials.

A cost-effective method for adjusting material elastic properties was desired for implementation in the joint design to achieve compliant stiffness. TPU, as a soft 3D-printed material, was chosen to evaluate the placement of voids within 3D-printed material to simulate the heterogeneous properties of ligaments. Huang et al. [78] demonstrated that composite TPU with voids influences stiffness properties of the polymer by assessing changes in elastic

modulus (E), used to evaluate material elasticity and stiffness. However, there is a significant difference between a composite and 3D-printed technique, with different attributes contributing to the material properties.

An investigation into the effect of void parameters, including void size and distribution, on the elastic modulus of 3D-printed void-infused TPU was conducted. **This study seeks to answer the research question as to the extent to which modifying the void parameters within soft, void-infused 3D-printed materials would impact their elastic properties.** This is analogous to behavior observed in composite materials, where voids can disrupt the internal structure and reduce the number of layer lines that contribute to stiffness or elasticity along the direction of the applied force.

In this study, a preliminary empirical assessment was conducted to evaluate how the inclusion of specific void parameters—specifically, void size and void distribution along the length and width of rectangular coupons—influences mechanical performance. The coupons were compared to the stress-strain behavior of biological ligaments to assess the ability of 3D-printed TPU to simulate the elastic behavior of ligaments, determined through tensile testing on an Instron machine.

With a methodology for evaluating void-infused 3D-printed materials ability to simulate ligament elastic properties, other void-infused soft materials, like that of the J5 DAP, can be preliminarily evaluated on how void parameters impact their elastic properties and their ability to produce similar elastic properties to human finger ligaments for the creation of a anthropomorphic compliant passive finger joint with desired double exponential joint torque response [25], [34], [41].

I examine material stiffness in Section 2.4.1, detailing the biomechanical compliance capabilities of void-infused 3D-printed soft materials via TPU. Section 2.4.2 describes a methodology for the creation of void-infused TPU. Section 2.4.3 details an experiment to determine the correlation between void parameters and elastic modulus through tensile testing. In Section 2.4.4, the data collected and analyzed to examine the elastic behavior of

void-infused TPU are presented. Section 2.4.5 discusses the effects of void-infusion and the ability of TPU to simulate void parameters. That exists between void parameters and elastic modulus and explores the optimization potential of these findings.

2.4.1 Overview

By explicitly defining the requirements for biomechanical compliance, a reference for simulating elastic properties of soft tissue in the finger can be established, thereby specifying the mechanical demands that the joint model must meet. Void-infused material is a novel method that enables soft, 3D-printable materials, such as TPU, to meet these requirements with favorable properties by incorporating controlled heterogeneity into the material.

A passive finger joint model for an instrumented manikin must show a double exponential joint stiffness, as seen in Fig. 1.9, response to be a viable representation of human finger joint movement [34], [41]–[43]. The model must also display the correct amount of resistance to torque applied to a finger joint and maintain relaxed finger positions, such as those of a real hand [34], [79]. With these criteria met, a finger joint model can be considered compliant. For a passive bio-referenced joint model to meet these expectations, the 3D-printed material must have stiffness properties similar to those of ligament tissue to create the desired joint stiffness. Ligaments were determined to contribute more to passive stiffness than the MTU [25].

Mimicking anatomic structures of ligaments across finger joints to create a compliant, dexterous hand requires mimicking the elastic properties of the ligaments as well. Since every human has varying joint stiffness within a particular range, a tunable method for adjusting stiffness properties of a material chosen to simulate the capsule ligament complex (CLC) in a joint model is beneficial for creating a fully compliant joint model.

This study investigated the effect of controlled addition of voids with specific parameters into a soft 3D-printed material as a mechanical method for manipulating material stiffness properties and mimicking heterogeneous properties of ligaments. A mechanical method

would alleviate the potential complications, high material costs, and complexities associated with a chemical method [25]. TPU was selected to evaluate this research question due to its low cost, wide availability, and suitability as a soft 3D-printed material. When additively manufactured, TPU exhibits viscoelastic properties [80] similar to the mechanical properties observed in human ligaments [81]. Viscoelastic materials have been considered a beneficial property for creating compliant joint models [25], [34].

The elastic properties of hand ligaments have not been well investigated through tensile testing. Ligaments in the body have an extensive range in stress-strain metrics depending on the amount of load they experience in the body [82]. To narrow the expected range to that of finger ligaments, a study of the ulnar collateral ligament, done on sixteen fresh-frozen thumb cadavers, indicated that the intact hand ligament has a failure load, maximum stress, and Young's modulus of 294.3 $\pm$ 28.2 N, 11.4 $\pm$ 1.2 MPa, and 37.3 $\pm$ 5.1 MPa, respectively [40]. To assess the mechanical performance of the TPU, a ligament study with similar elastic properties was chosen for reference.

By determining the relationships between the mentioned void parameters and stiffness, an optimal approach can be implemented that maps the desired compliance to void parameters, allowing for the creation of compliant materials from any desired soft 3D-printed material of those in the J5 DAP.

2.4.2 Methodology for Void Infusion

A method for placing voids within thin structures was examined using test coupons for experimentation. MATLAB was used to generate coordinates for evenly distributed void patterns with no overlap using dimensional inputs and void parameters. Code is provided in Appendix A. These coordinates were input into SolidWorks' linear pattern feature to create a matrix of voids of a particular size patterned within the coupon.

A 3D model of a rectangular coupon of dimensions 152.4 mm x 3.2 mm x 101.6 mm was created using SolidWorks. To place voids into the coupon model, a linear sketch pattern

feature was used that allowed for each void to be given a coordinate within the coupon which was limited to a certain distance from the edge of a specific dimension. A cube void shape was used to reduce print complexity, reducing the number of changing parameters. Void placement of the Z coordinate, that is position along the thickness of the coupon, was kept constant such that the center line of the coupon went through the midpoint of the single void on the Z-axis, as it was out of the scope of this study. The coordinates were generated using MATLAB code to ensure that the voids were evenly spaced and there was no overlap. The MATLAB code generated a table of coordinates that were generated in the coupon in SolidWorks.

The range along a certain axis within which the coupons were linearly spaced between, the number of voids along the Y dimension (width), the number voids along the X dimension (length) and the void size. With this code, 3D models of coupons, similar to Fig. 2.9, with voids infused in them were created for varying the void parameters.

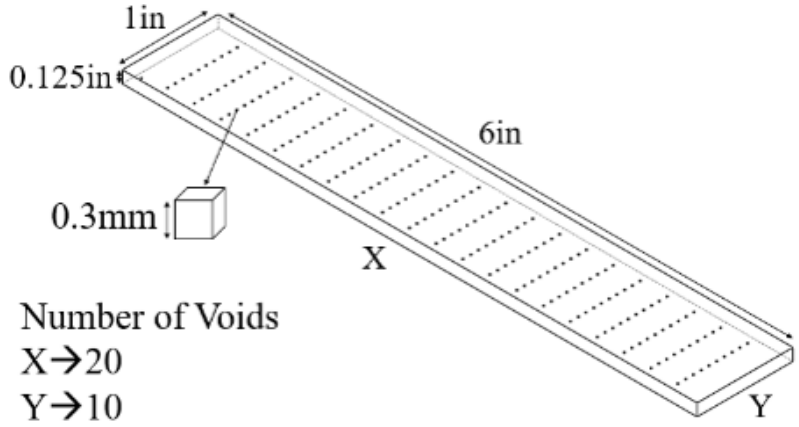

Figure 2.9: MATLAB and SolidWorks used to generate a void-infused model of a coupon for 3D-printing. Void-infused digital coupon models were used to assess the impact of void parameters on elastic properties. Void parameters can be changed through MATLAB code and represented physically in SolidWorks.

2.4.3 Experimental Design

The void content in the X and Y directions, as well as the void size, was changed independently to determine their effect on elasticity. The samples created for testing can be

seen in Table 2.1. Each parameter was varied independently while a standard of 20 voids in the X, 10 voids in the Y and 0.3 mm void size was maintained. The void-filled coupons were also assessed against a void-less sample.

Table 2.1: Void Parameters used in eight 3D-printed coupon samples for displacement tensile testing on an Instron mechanical tester.

Parameters	**S1**	**S2**	**S3**	**S4**	**S5**	**S6**	**S7**	**S8**
Void Content on Length (X)	20	20	20	20	20	20	50	90
Void Content on Width (Y)	10	10	10	10	5	15	10	10
Void Size (mm)	0.1	0.3	0.8	1	0.3	0.3	0.3	0.3

This was done to isolate the behavior of a sample to one input parameter change. NinjaFlex [83] TPU was used to print coupons. The test coupons were printed on an Anycubic Kobra 2 Max FDM printer [84] with a rectilinear infill with 100% infill, which prints a line pattern that oscillates between approx. 45° direction off the center line along the length of the coupon to mitigate additional undesired voids and best mimic anisotropic ligament tissue, with the resultant under tensile load along the length of the coupon.

A tensile displacement test was carried out on each coupon using an Instron Machine [39], [85] with max force of 100 kN at a 0.3 mm/s displacement rate as set up in Fig. 2.10. A uniaxial force was applied along the length of the coupon. Sandpaper was used between the machine grips and the coupons to avoid slipping during experiment. The experiment was done until failure.

Based on the preliminary assessment of the behavior of the coupons, a sample representing both void distribution and size was chosen to compare to the stress-strain behavior of the void-less coupon as well as the human ligament. S3 and S6 were selected as they showed significant deviation from the control. To assess consistency and variance in results, the experiment was repeated three additional times for the control, S3, and S6. These coupons were converted to engineering strain and stress, and an average of the repeated sample types was taken with standard deviation.

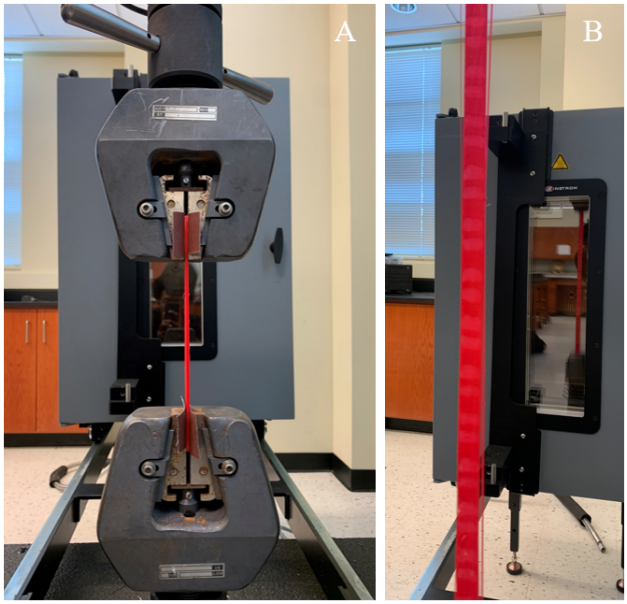

Figure 2.10: Figure 2.10A shows a coupon within the grips of an Instron mechanical tester before the start of a displacement tensile test with no load. Figure 2.10B displays a coupon sample during experimentation being pulled axially at a 0.3 mm/s displacement rate along its length.

2.4.4 Results

A plot of force against displacement was plotted for coupons with differences in void distributions in X and Y dimensions of the coupons in Fig. 2.11. The plot was assessed to determine the best void distribution for further evaluation of its stress-strain behavior. The plot was truncated to 200 mm of displacement to focus on the observed elastic regions of the coupons.

Figure 2.12 shows the force against displacement plot for coupons with varying void size. The plot was also truncated to 200 mm displacement for visualization of the observed elastic region. The coupons for both void distribution, void size and the control exhibited similar elastic behaviors with a linear elastic and plastic deformation region after reaching a yield point.

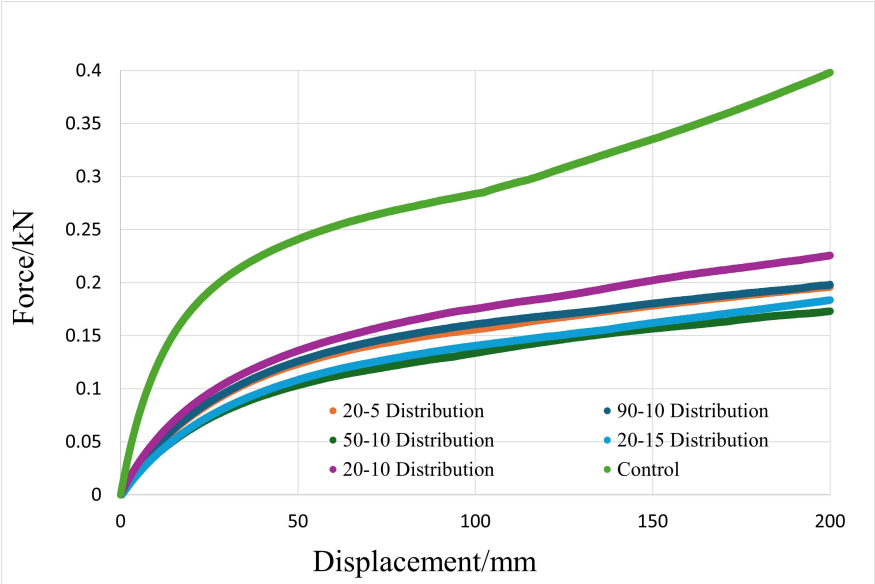

Figure 2.11: Force–displacement plot from uniaxial tensile testing of 3D-printed TPU coupons with X–Y void distributions, using an Instron mechanical tester. Force was applied along the length of each sample, with displacement plotted up to 200 mm. The presence of voids influenced the elastic properties of the printed structures.

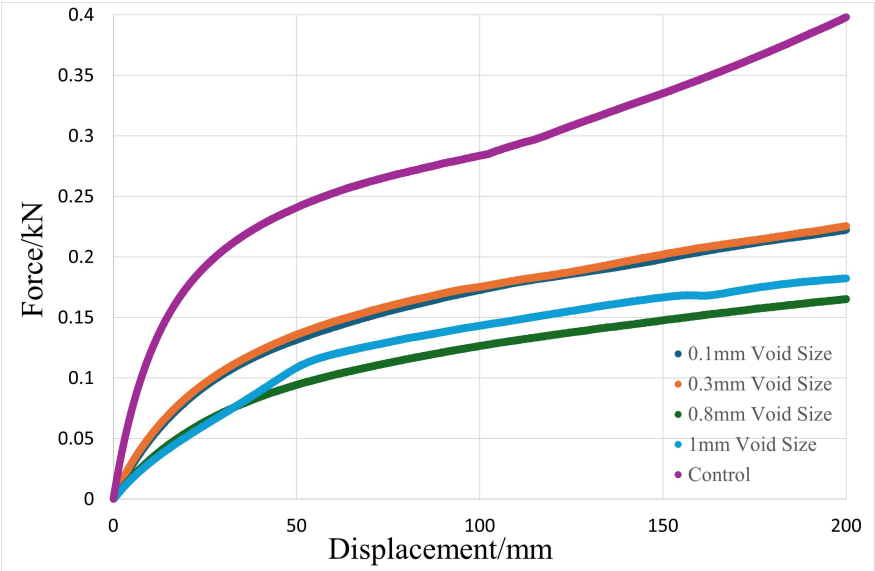

Figure 2.12: Force–displacement plot from an Instron uniaxial tensile test of 3D-printed TPU coupons with varying void sizes. The plot demonstrates that void size influences the elastic properties of the printed structures. Data was truncated at 200 mm displacement to focus on the elastic region of the coupons for analysis.

Engineering stress and strain for S3 and S6, as well as the control, were calculated for each experiment run. Using the measured thickness and width of each coupon, the cross-sectional area of each coupon was determined. Stress was calculated using Eq. 2.1

$$\sigma_x = \left| \frac{F_x}{A_x} \right| \tag{2.1}$$

where σ_x is engineering stress, F_x is uniaxial force applied to the coupon, and A_x is the cross-sectional area of the coupon orthogonal to the direction of uniaxial force. Engineering strain was found using the measured distance between the points at which the coupons were gripped. The displacement measured was divided by the grip length to obtain the engineering strain. The mean stress and strain for the repeated experiments done for S3, S6, and the control, with their standard deviations, were calculated and plotted against each other as seen in Fig. 2.13.

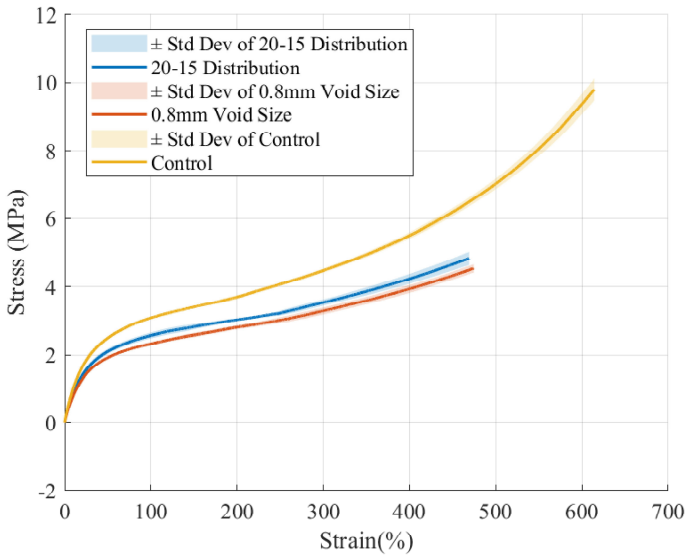

Figure 2.13: Stress-Strain behavior for coupons with void distribution 20:15 with 20 voids in the X and 15 voids in the Y dimension with void size of 0.3 mm, coupons with void size of 0.8 mm and distribution of 20 voids in the X and 10 in the Y and a void-less control coupon.

The mean elastic modulus of average stress was estimated by finding the gradient of a linear best-fit line for average stress against strain under 10% strain, which was within the linear elastic region for each coupon variation chosen for stress-strain analysis. Table 2.2 displays the calculated elastic modulus for each coupon type.

Table 2.2: Elastic moduli determined by linear regression within the elastic region under 10% strain for coupon samples S3 and S4 representing void distribution and void size parameters, respectively. Results are compared to a control coupon without voids to assess the influence of void inclusion on material stiffness.

Sample Group	**Elastic Modulus (MPa)**
S3 (20-15 Distribution)	0.08
S4 (0.8mm Void Size)	0.09
Control (void-less)	0.1

The average stress-strain behavior for samples S3, S6, and the control were compared to the expected ligament stress-strain behavior of ligaments. The elastic properties of the anterior cruciate ligament (ACL) of animal cadaver was taken as a reference for ligament behavior. In the study of Pioletti et al. [39], the elastic properties of anterior cruciate ligament was determined by using an uniaxial test machine to pull ligament tissue along its anisotropic direction. The data was derived from eleven bovine calves. The stress-strain behavior of the ACL was assessed at various strain rates. The result closest to the 0.3 mm/s strain rate used in this was used as a reference to compare TPU. Figure 2.14 shows a plot of average stress-strain behavior for S3, S6 and control along with expected ACL elastic behavior.

2.4.5 Discussion

Plotting of various void distributions in Fig. 2.11 and void sizes in Fig. 2.12 against a control void-less sample allowed for the comparison of elastic behaviors of void-infused coupons with a control sample without voids. This comparison illustrates the impact of void parameters on the material's elastic properties and overall mechanical behavior, with a

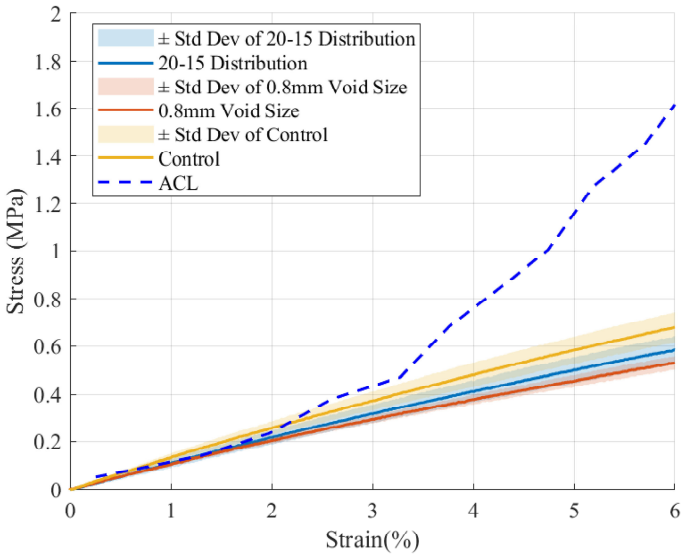

Figure 2.14: Comparison of stress-strain behaviors between void-infused and void-less TPU with expected behavior of the anterior cruciate ligament (ACL) from animal cadaver.

distinction in the behavior between void-infused structures and the control. However, these samples needed to be assessed for their repeatability and tunability.

Figure 2.13 demonstrates that 3D-printing soft materials can produce repeatable and tunable mechanical performance. To evaluate repeatability and variability, standard deviation was employed to quantify the tendency of 3D-printed structures to exhibit consistent elastic properties across prints. Modifying void parameters—such as size and distribution—led to significant differences in mechanical performance. These differences were reflected in distinct stress–strain responses between groups, with no overlap in standard deviation ranges, thereby confirming the influence of internal architecture on mechanical behavior. 3D-printed void parameters were observed to alter mechanical performance when voids with specified distributions and sizes were included within a printed structure. Stress-strain behaviors differed significantly in the plastic regions with the inclusion of voids, but exhibited similar behaviors in their linear elastic regions.

This is also seen with the elastic moduli determined for S3, S6 and void-less parameters seen in 2.2 with a max of 0.02 MPa variance in estimated elastic modulus. A reduction in yielding stresses was observed with the inclusion of void parameters.

With repeated experimentation, the effect of void parameters does not exhibit monotonic behavior with that of the void-less samples.The observed differences in behavior may be attributed to variations in mechanical pressures and micro-stress concentrations, resulting in a reduction in the yielding stresses supported by the material, which could potentially lead to fracture under lower loads than those of 3D-printed soft materials without voids.

Further research on the micro-structures within soft material is needed to verify the causes of the change in mechanical performance produced by the addition of voids and attribute deviations and trends to specific void parameters. Further defining of a tunable relationship between void parameters and the elastic properties of 3D-printed soft material structures will enable the designers of anatomic hand manikins and simulators to tune the elastic material properties for biomechanical simulation of the human finger.

Measured TPU did not meet elastic performance of reference chosen to represent ligament tissue properties based on comparison to reference biological ligament. In Fig. 2.14, TPU used in this study showed similar elasticity to the reference ligament in its toe region but differed significantly in the linear elastic region as the TPU elongated more under lower stresses than ligaments. In contrast, the ligament reference showed more resistance with an increase in load.

A stiffer 3D-printed soft material than the NinjaFlex TPU used in this study is required to simulate the elastic properties of biological ligaments. To improve performance, further investigation is needed into the elastic properties of other soft 3D-printed materials and the effect of void parameters in those materials. The inclusion of voids in soft 3D-printed materials has potential in expanding soft material options for ligament simulation by making stiffer materials more compliant.

A difference in elastic properties resulting from the inclusion of voids in 3D-printed soft material provides insight into the ability of void parameters to change elastic performance, answering the posed research question. Further evaluation of the specific effects for each void parameter would provide a cost-effective method to adjust the elastic properties of soft materials. To reduce Type I error, further experimental assessment is necessary to determine the number of samples required to verify observations and make trend predictions in this analysis.

Placing voids within 3D-printed material allows for the insertion of heterogeneous properties, which are observed in human tissue. Mimicking elastic ligament properties requires the simulation material to have similar stiffness properties to those of the finger ligaments. A study with a finger ligament reference is needed for direct comparison.

2.5 Conclusion

An additively manufactured instrumented passive anthropomorphic hand can be used to validate soft hand exoskeletons. The biomechanical compliance of a joint model can be divided into two categories: high-fidelity anatomical structures and compliant material elastic properties for desired joint stiffness.

For high-fidelity anatomical structures, integrating AI-based auto-segmentation with expert-guided manual refinement enables the generation of an anatomically precise hand model. PolyJet 3D-printing, using the J5 DAP, enabled the fabrication of complex anatomical structures of the hand derived from MRI. The print included both soft and hard tissue simulation with soft and hard J5 DAP materials, respectively, in a single print in less than 12 hours. Preliminary biomechanical assessment of 3D-printed model revealed compliance limitations.

Void-infused 3D-printed soft materials showed promise as a method for changing the elastic properties of soft materials for compliance. This study aimed to investigate whether the inclusion of voids in 3D-printed TPU influenced the elastic properties of a print structure.

Void size and distribution were tuned parameters to address this question. Stress-strain analysis was conducted to examine the effects of void parameters, size, and distribution. While NinjaFlex TPU showed limitations in simulating ligament elastic behavior, the addition of voids within 3D-printed structures had a non-monotonic mechanical performance when compared to void-less material.Further investigation into a defined model for creating compliant material from void-infused 3D-printed material for soft tissue simulation, along with the anthropomorphic model structure, is expected to develop a compliant anthropomorphic anatomical PIP joint model.

Chapter 3

RUQ Ultrasound Manikin for Medical Training

3.1 Introduction

This chapter presents an approach for utilizing 3D-printable materials, employed by the J5 DAP, to design a novel 3D-printed anthropomorphic manikin for RUQ POCUS training. The model was designed to be modular for ease of improvement, allowing for future changes in pathology and accommodating the print tray limitations of the J5 DAP. POCUS requires an operator to balance several tasks simultaneously within the observation room, making its processes, physics, and 'knobology' difficult to visualize in a lecture setting in which trainees observe 2D lecture visuals. To minimize the disconnect, live patient and cadaver scanning as well as virtual and physical phantoms or manikins have been used as a solution by training programs, but have proved, respectively, risky, unethical, and costly for full complements of trainees. Infrequent live patient scans can be stressful for trainees in a time-constrained environment, potentially leading to patient harm. Alternatively, cadavers of the human body or animals have been deemed unethical.

Virtual phantoms and manikins have been useful in basic-level education of POCUS but lack image variability, cost-effectiveness for large training cohorts, cohesive participation, guidance during training sessions, and realism. Current VR applications do not give trainees comprehensive experience in the processes of POCUS. Physical phantoms and manikins tend to be static, costly, and made from molded material. Molded models require a complex and labor-intensive process to achieve echogenicity, making the development of new pathological variations time-consuming. Moreover, creating internal organ structures with accurate

echogenic properties involves intricate multi-step molding techniques, further limiting efficiency and adaptability. Obtaining a single manikin per pathology for a large cohort becomes challenging for training programs.

To minimize these drawbacks, it is believed that the manufacturing of a modular, reproducible soft physical manikin with echogenic and anatomically correct internal liver and kidney anatomy for standard RUQ POCUS using Stratasys J5 DAP. A manikin with directly additively manufactured tissue and organ models enables the rapid fabrication of different pathologies, resulting in significant cost savings compared to alternative methods. That is, printing a new organ or part of an organ would be more cost-effective than purchasing a new manikin. Additionally, soft physical manikins with echogenic models include the use of a real US device, thereby enhancing trainee proficiency in medical device handling and procedural skills than virtual reality simulators.

To begin the exploration of such a device, this study evaluates the use of J5 DAP materials to produce desired echogenic properties for modeling kidney and liver anatomy. J5 DAP material combinations of DraftWhite, ElasticoClear, TissueMatrix and GelMatrix were printed and assessed for comprehensive grayscale analysis of acquired material US images. The echogenicity of various 3D-printed materials was validated against that of the renal pelvis, renal kidney and liver tissue within standard RUQ US. The J5 DAP materials were categorized based on their echogenic properties, validated through grayscale analysis and confirmed by a medical professional. Grayscale metrics served as a quantitative method to assess US intensity and echogenicity. Additionally, a workflow was developed for rapidly and cost-effectively generating anatomical mesh models from CT scans of the RUQ, including internal structures of the liver and kidney, using 3D Slicer [74]. With both the material characterization and anatomical modeling approach established, suitable J5 DAP material combinations can be selected for 3D printing and integration into a high-fidelity RUQ ultrasound simulation manikin.

3.2 Workflow for Modeling Internal Organ Structures using 3DSlicer

Segmentation software and commercially available 3D models of RUQ organs have enabled efficient and effective anatomical modeling [86]–[89]. However, existing models focus primarily on external organ morphology and lack detailed internal structures. In addition, commercial models often come at a high cost and offer limited anatomical fidelity. Advanced segmentation tools capable of producing detailed, high-resolution models may also require expensive licenses, creating barriers to widespread use. In this section, a rapid-manufacturing, cost-effective method for generating anatomically accurate internal models of the liver and kidneys using open-source software platform, 3D Slicer.

3.2.1 Model Reference for Anatomic Geometry: CT vs MRI

MRI and CT scans have mainly been used to create 3D-printable anatomically accurate models of abdominal organs [4], [10]. While MRI scans are more accessible than CT scans due to the latter's use of high levels of ionization, scans from both imaging techniques were obtained. CT scans of the abdomen are a standard procedure in medical examinations that provide a high amount of information on pathologies, making them more accessible than other anatomies, such as the human hand. To create anatomically correct models of organs and tissue in the RUQ of the human body, 25 deidentified CT and 28 deidentified MRI scans of the abdomen were obtained from East Alabama Medical Center. The scans were provided as DCOM files, suitable for use in most segmentation and visualization software. Each patient's scan was approved under IRB for research purposes. After reviewing the obtained scans, the CT scans were determined to be the most detailed medical imaging technique for segmenting the external and internal features of RUQ organs, specifically the liver and kidney. Using open-source segmentation software, 3DSlicer [74], the scans were examined alongside medical students to determine the optimal scans that presented desired internal anatomy of the liver and kidneys for RUQ ultrasound. Segmentation requires prior knowledge of pathology and radiology. Medical students assisted with providing medical expertise on

identification. A CT scan with the most ideal image intensities of anatomic features, seen in Fig. 3.1, was chosen for segmentation. 3DSlicer was used to segment the models within the RUQ, a process that involves delineating the boundaries of distinct anatomic features within the scan.

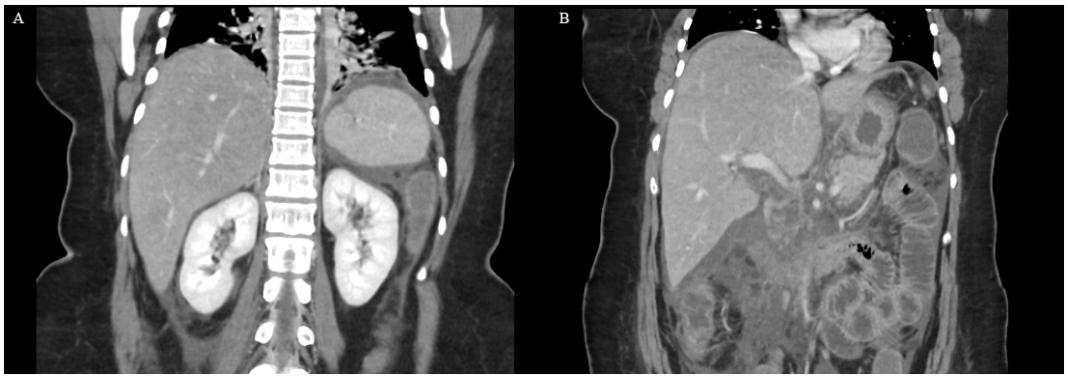

Figure 3.1: Coronal view of selected CT scan with distinct internal liver and kidney anatomy as well as other RUQ features. CT scan's high anatomic resolutions make it a suitable medical imaging technique for model generation.

3.2.2 AI-Driven Automated Segmentation:TotalSegmentor

Segmentation done strictly manually can be a trivial labor-intensive process [9]. Assistive auto-segmentation tools within software can be used to estimate the boundaries of features being segmented. Some tools are capable of segmenting areas with similar scan intensities, or AI-driven algorithms trained to recognize and mark organ boundaries within medical images. 3DSlicer's extension- TotalSegmentator [89]- uses an image recognition algorithm to efficiently create segmented bodily systems within the abdomen. The algorithm was trained on 1228 subject CT scans and 616 MRI scans. It is capable of developing a detailed assembly of morphological abdominal organ models in under an hour, with adequate processing capabilities. For CT scan segmentation, the algorithm can segment up to 117 body features. Despite TotalSegmentor's vast anatomic modeling capabilities, it does not segment internal organ features as well as thin subcutaneous muscles and fat and provides

limited vascular or duct segmentations. This includes several features desired for RUQ ultrasound, such as the diaphragm, portal veins, hepatic vessels, renal pelvis, pyramids, bile duct, and circulatory vessels. The TotalSegmentator AI model was used in 3DSlicer to segment abdominal organs that it could recognize using the chosen abdominal CT scan. The result of the algorithm is shown in fig 3.2.

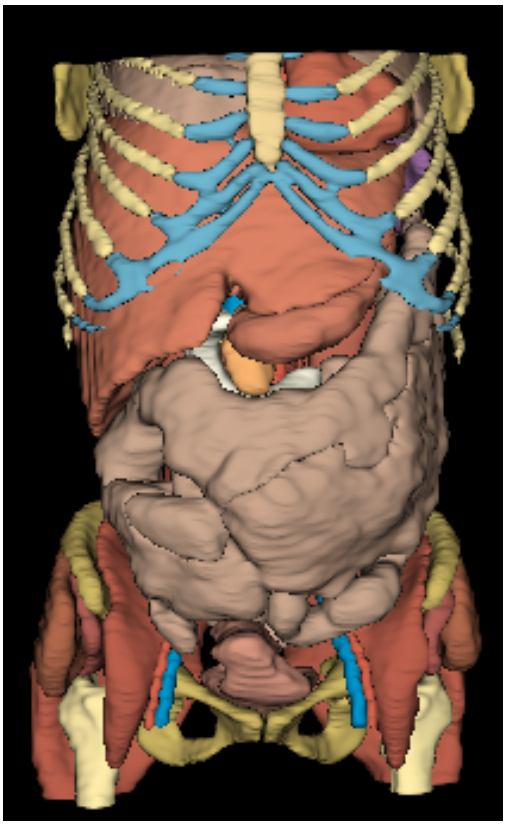

Figure 3.2: Segmented abdominal structures generated using the TotalSegmentator extension in 3DSlicer. The AI-driven segmentation algorithm enables efficient delineation of major abdominal organs.

The TotalSegmentator model reduces the segmentation time of bodily systems in the abdomen, requiring only minor adjustments to refine the segmentations. This significantly improves the segmentation timeline for designers developing anatomically specific manikins, addressing a significant limitation in the production of 3D-printed anatomical models. The segmentations generated by TotalSegmentator were sufficiently anatomically accurate for training purposes, as trainees primarily require a close approximation of human anatomy

for visual recognition and the development of device handling skills. Anatomically accurate kidney and liver models were generated as seen in Fig. 3.3.

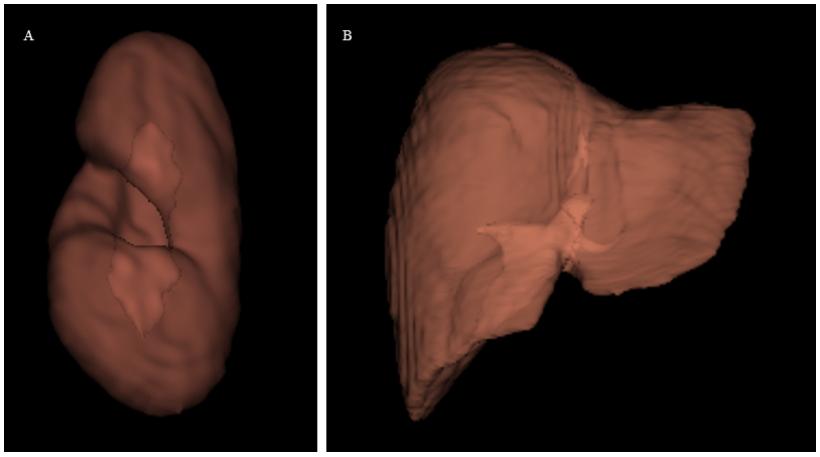

Figure 3.3: Semi-transparent 3D models of organ morphologies generated using TotalSegmentator. (A) Kidney and (B) liver models were effectively segmented to capture general external anatomy. However, these segmentations lack sufficient detail for internal organ structures, limiting their use for simulations requiring internal anatomical accuracy.

The Ai-model generated no internal structures within organs as these features were out of scope of the specific algorithm used. While the AI model was limited to segmenting only the gross morphology of the organs, it generated an editable segmentation and model in 3DSlicer. This provided the opportunity for further model refinement and use of model segmentations in future segmentations and segmentation procedures for other anatomic features. In addition, several segmentations lacked anatomical accuracy due to disjointed segments, over-segmentation, or incomplete segmentation, resulting in unrealistic models. This issue was attributed to the algorithm's weakness and the quality of the scan, as the algorithm misidentified organ boundaries.

The desired internal features within the liver and kidney, as well as the inaccurate segmentations, had to be segmented using other extensions, tools, or manually in 3DSlicer. 3DSlicer has another extension for fast segmentation of liver vessels, known as RVesselX [90], that follows similar intensities near a predetermined tree model generated from nodes placed at key anatomic features in the scan to create internal vessel structures present in uploaded

medical images. The model requires precise anatomic knowledge of scan radiology and liver anatomy for proper placement of nodes to make an adequate segmented model. An alternative method for segmenting liver vessels, which does not require significant anatomic knowledge, was investigated.

3.2.3 Fast Model Generation with Semi-Automated Segmentation Tools

3DSlicer features several segmentation tools in its segmentation editor module, which were used to segment internal features of the liver and kidney. Some of these tools facilitate faster segmentation and editing than manually segmenting in each image within the scan. The steps taken to create detailed models in commonly used segmentation software, 3DSlicer, are briefly discussed by other model designers [2], [55]. Marro et al. [10] gives a review of popular auto-segmentation tools found in open-source segmentation software, but does not provide a methodology to create a model in any specific software. This study presented a method for using auto-segmentation and other tools in 3DSlicer to develop internal structures of the liver and kidney. The process entails the use of thresholding, surface smoothing, removal of undesired segmented areas, and manual adjustments. Comparable tools available in other open-source software platforms can be applied similarly to the methodology outlined here to achieve analogous results.

1. Thresholding

Thresholding is a widely used segmentation technique that serves as an essential tool for rapidly generating initial segments [10]. This feature enables the user to specify a range of intensity values that encompass the desired feature to be segmented. In 3D slicer, this can be used to define a mask for other tools used to edit the segmentation, that is, only segments within this threshold can be created, edited or deleted. For the internal structures of the kidney and liver, this was the first tool used to establish base segments that could be

refined. The same threshold was used as a mask, limiting segmentation to only the specified intensity range.

A threshold chosen can be limited to a specific, desired segmented region. Since most of the desired features were within the kidney and liver segmented by TotalSegmentator, the threshold could be contained within the gross morphology already segmented.The applied threshold segmented the desired features across several images simultaneously. Threshold values must be adjusted based on the specific scan characteristics and the degree of contrast between the target structure and adjacent tissues, as these factors directly influence the accuracy of segmentation. Figure 3.4a shows the resulting model after using the threshold tool for initial segmentation of desired liver vessels and renal pyramids.

2. Smoothing

Following thresholding, the smoothing tool was used to refine the base segmentation created by the thresholding process. The tool features repair and smoothing methods that prompt users to select the degree to which these methods will affect the segmentation. The smoothing method can be used directly on specific areas of the generated 3D representation by 3DSlicer or on the entire segment. 'Gaussian', 'closing' and 'opening' are the three key features of the smoothing methods used to refine the models.

The 'gaussian' feature was first used with a standard deviation of 3.00 mm. Depending on the impact of the Gaussian at this value, it may need to be decreased or increased to remove further or less segmentations that appear as unstructured, forming no clear volume. The method shrinks the current segmentation and, in the process, creates a smoother model surface. 'Closing' was useful to repair small gaps within the segmentation.

However, it was not best for segments that contain multiple disjoint proximal volumes as it may join the volumes to fill the gap. 'Opening' helped remove any additional undesired extrusion that came from the model, as well as remove any extrusions that would be difficult

to print or cause print failure. These two methods were applied with adjusted weighting based on the extent to which they improved segmentation refinement.

For liver vessels and renal pyramids, 'opening' was used with a kernel value of 2.00 mm, while closing was not, as it reduced anatomic accuracy by creating undesired bridges between vessels and pyramids. The 'closing' feature was useful in repairing holes in larger anatomical masses, such as the renal pelvis. Figure 3.4b illustrates the capabilities of the smoothing tool to remove undesired segments in the liver for smoother models, in this case, liver vessels and kidney pyramids. To evaluate the change in model appearance between thresholding and smoothing Fig. 3.4 shows the result from both processes adjacent to one another for both renal pyramids and liver models.

3. Island Removal & Splitting, Scissors and Local Thresholding

After smoothing the model, a more detailed outline of the segmented region was formed. However, instances can occur where large segments remain a part of the segment outside the region of interest (ROI) or the feature removes too much of the ROI. The scissors tool was used to remove isolated portions of a segment that are unwanted. Undesired segments were removed by encircling the ROI with the scissors tool. A drawback of the scissor tool is that it only works in 2 dimensions. Multiple scissor cuts may be required to remove the remaining isolated outside the ROI.

Another method for removing undesired segments is with the 'Islands' tool. An island can be described as an isolated region or voxel cluster within a segment. This tool provides the user with options including 'keep largest island', 'remove small islands', 'keep selected island' and 'split islands to segments'. This tool was useful in distinguishing the various vessels within the liver into distinct segments. The 'keep largest island' feature was used to remove any small islands that remained after smoothing the liver vessels and renal pyramids.

The 'split islands into segments' feature was used to segment hepatic vessels different from the portal vein and remove any other segmentations that may have been left. This

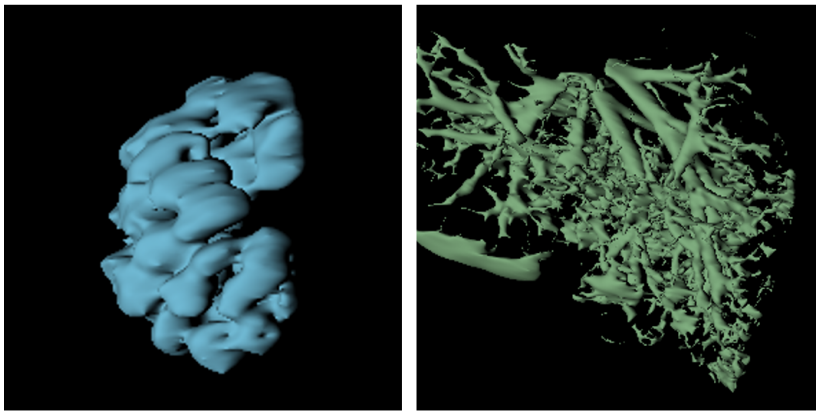

(a) Initial segmentation of renal pyramids, on left, and liver vessels, on right, using the threshold tool in 3D Slicer.

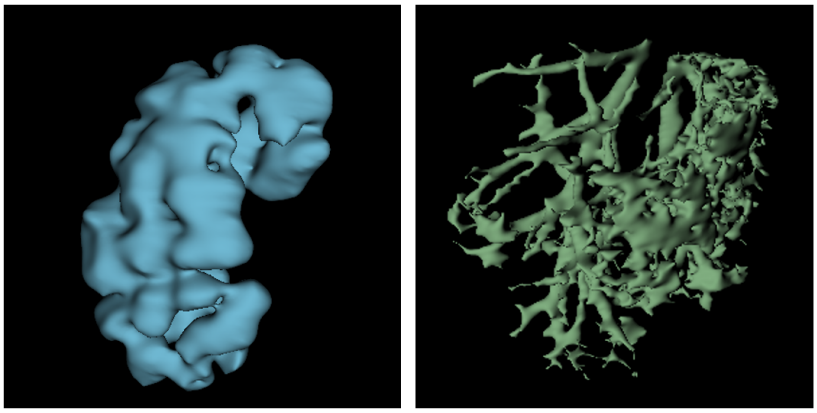

(b) Refinement of segmented renal pyramids, on left, and liver vessels, on right, using the smoothing tool in 3D Slicer.

Figure 3.4: Segmentation and refinement of internal anatomical structures-renal pyramids and liver vessels-from imaging data using 3D Slicer thresholding and smoothing tools. Thresholding enabled the selection of intensity ranges to isolate structures of interest. Then, smoothing was applied to enhance the output from thresholding, producing more precise 3D models of internal structures.

feature requires the desired vessel islands to have no overlap. In this case, the erase tool was used to separate segments in specific slices. This was done when insignificant connections were made between two large islands. For segments with separate volumes, such as renal pyramids, this feature remained beneficial. Islands that were initially intended to be one segment but were made distinct were combined to form a single segment.

When essential structures were excluded during global thresholding, the local thresholding tool was used to recover and accurately segment those regions. Local thresholding enabled the selection of specific islands within a certain threshold to be added to the segment. While segmenting, it was easier to create a segment with larger boundaries than the ROI for refinement than to generate segments using tools like 'fill between slices'. Local thresholding was performed within the existing segment boundaries to minimize the formation of undesired islands. This requires a copy of the desired segment to be made so that the local threshold can be performed within the previously developed segment.

4. Manual Adjustments and Final Smoothing

Auto-segmentation, regardless of the tools employed, has inherent limitations and requires user input to refine models and produce high-fidelity, anatomically accurate features. The segmentation was evaluated, and slices with inaccurate anatomic features were adjusted using the 'erase', 'draw', 'paint', and 'level tracing' tools to create the final structures for anatomic accuracy by removing and filling desired areas on scan slice. Level tracing segments nearby sections within a similar threshold range. At the end of the segmentation process, the smoothing procedure was repeated with lower intensities where needed for a final model surface refinement. Gaussian smoothing was reapplied with a smaller standard deviation (less than 2 mm). Higher smoothing values, particularly those exceeding 0.1 in (3 mm), were found to reduce the segment boundaries and compromise anatomical accuracy excessively.

Segments were classified as having satisfactory distinguishable anatomy after review with medical students. A copy of the morphological segments of organs were made such that the segments of internal structures could be removed. This preserves the morphological mass, so that the process could be repeated, if internal structures' segment is changed. 3D Slicer enables users to subtract segments from one another, preventing overlap and ensuring clear separation between anatomical structures in the resulting models.

This tool was employed both to generate hollow cavities within the segmented morphological mass and to prevent undesired overlaps between neighboring anatomical models, thereby improving the accuracy and usability of the final 3D reconstruction. Figure 3.5 shows the final resulting internal structures developed for the kidney and liver for 3D-printing after applying the steps presented in the proposed methodology.

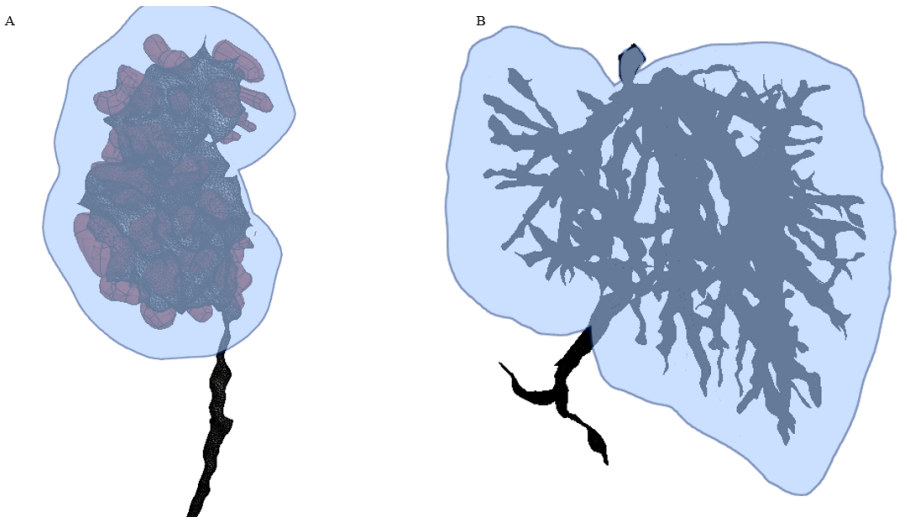

Figure 3.5: Refined (A) Kidney and (B) Liver, with internal anatomy generated from CT Scans using the proposed segmentation methodology in 3DSlicer and mesh-editing software to prepare the model for printing.

A methodology for deriving organs with auto-segmentation tools has been presented. The segmentation and resulting 3D models from TotalSegmentor's generated models and the internal kidney and liver derived with the proposed internal structure methodology can be seen in Fig. 3.6.

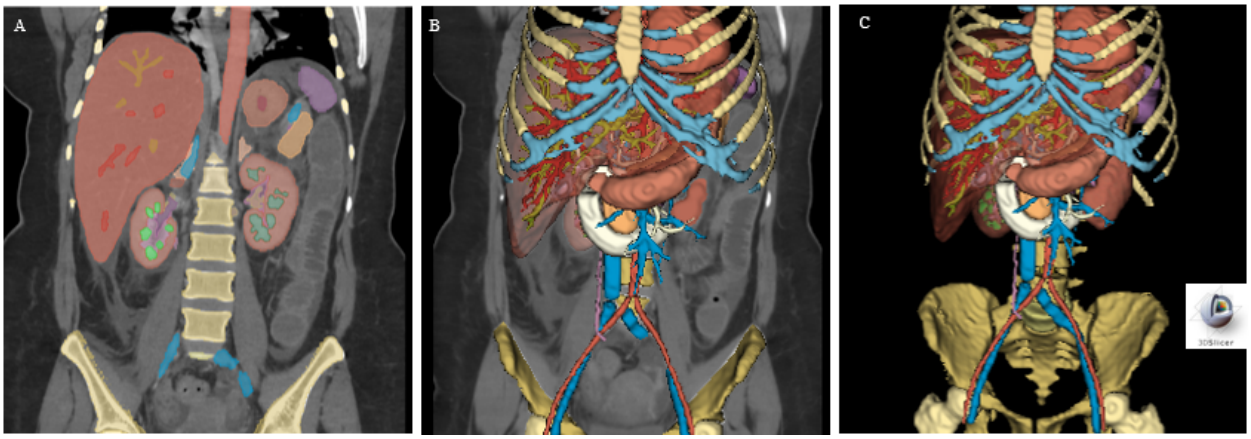

Figure 3.6: Anatomical Models of abdominal organs and tissue were generated using an AI-driven algorithm, TotalSegmentor, and auto-segmentation tools in 3D-slicer.

3.2.4 Export and Post-Processing of Segmented Models for Additive Manufacturing

Models generated through segmentation software,3D Slicer, were exported as STL files for further processing. This included files produced using TotalSegmentator, as well as auto-segmented internal organ structures and remaining soft tissues within the RUQ. Open-source mesh repair and editing software, such as MeshLab [91] and Autodesk Meshmixer [92], are commonly used to resolve invalid mesh constructions that may cause errors during 3D-printing [9]. In this study, Autodesk Meshmixer and Fusion 360 STL repair tools were utilized to correct mesh irregularities and reduce the chance of print failure. Autodesk Fusion 360 [93] proved to be an effective CAD platform for converting STL files into solid bodies, enabling the application of CAD tools to both anatomic STL models and their converted solid forms. Additionally, it supported the customization, design and integration of non-anatomic components for interface with anatomical models.

Models were converted into solid bodies in Autodesk Fusion 360 using the 'Form' environment. STL files converted within this environment allowed grouped surface faces, which helped reduce overall model complexity while preserving visual and structural aesthetics.Organ models were prepared for printing, which involved splitting models, creating internal volumes using the 'boundary fill' or 'combine' feature, and modifying models that

did not fit within the RUQ nor on the J5 DAP built tray. The models were exported as STL files for printing.

An assembly of the anatomical components, seen in figure 3.7, was created to facilitate the design of a containment unit containing the RUQ. Abdominal models obtained from Zygote[86] were used to replace specific models, such as ribs, IVC, and aorta, in the RUQ for higher-fidelity structures to improve the overall model, where 3DSlicer models were believed to be modifiable.

Figure 3.7: Digital assembly of the RUQ internal anatomical components, including detailed liver and kidney anatomy, prepared in Fusion 360. The environment enabled integration and adjustment of models generated using 3DSlicer and sourced from Zygote to constrain the RUQ region.

3.3 Echogenic Characterization of J5 DAP Soft Materials for RUQ Anatomical Simulation

3.3.1 Overview

While accurate anatomical geometry is essential for achieving anthropomorphism, the materials used to fabricate anatomical models must also replicate the mechanical and acoustic properties of the human tissues they represent [61]. In US simulation, it is particularly important that the density and acoustic impedance of the material closely mimic the echogenic response of real tissues. Soft hydrogels, agar solutions, and synthetic gels are frequently used in simulation due to their US-transmissive nature [94]. However, these materials are often brittle, prone to dehydration and degradation, and require precise chemical formulation to achieve tissue-specific acoustic velocities [61]. Moreover, producing such models typically involves labor-intensive two- or three-part molding techniques to incorporate heterogeneous internal structures, which significantly increases production time and complexity.

Silicone rubber represents another common alternative but also demands specific additives to achieve the desired echogenicity. In contrast, the Stratasys J5 DAP utilizes polyJet technology to automate the mixing of materials in defined ratios, enabling the fabrication of multi-material structures with customized mechanical and acoustic properties. Despite its potential, the application of polyJet printing for simulating diverse echoic responses in medical ultrasound imaging remains underexplored.

In this section, the development of new material formulations created with Stratasys' DAC and printed on the J5 DAP was investigated for its ability to simulate the acoustic properties of liver and kidney tissue, thereby enhancing the realism of an RUQ POCUS simulator. The US performance of the printed materials is assessed by comparing the echogenicity of printed test models with in vivo US images of real liver and kidney tissue, specifically the renal pelvis and medulla. Furthermore, the study evaluates the acoustic characteristics of

individual J5 materials across various mixing ratios to determine their suitability for specific organ representation.

3.3.2 Methodology

Given the wide range of materials available for use with the J5 DAP, a baseline assessment of Stratasys' commonly used material presets was conducted to identify combinations suitable for structurally sound soft tissue prints. Presets designed for compliant anatomical structures where elasticity is essential—such as ligaments and tendons—primarily utilize ElasticoClear(EM). In contrast, presets for soft tissues, such as the liver and subcutaneous fat, predominantly use GelMatrix(GM) and TissueMatrix(TM). To increase material stiffness, DraftWhite(DW) is often blended with soft materials, or thicker outer layer of ElasticoClear is applied.

Based on this review, it was expected that TissueMatrix and GelMatrix will serve as the primary components for constructing soft, low-density structures. The addition of ElasticoClear or DraftWhite is expected to increase material stiffness and acoustic reflectivity, resulting in higher-density materials. However, excessive mixing may compromise the anthropomorphic tactile quality of the print. Thus, selecting an optimized blend that balances softness and acoustic properties is crucial for achieving realistic and functional material behavior in an ultrasound-compatible anthropomorphic manikin.

While the available material presets were designed to replicate specific anatomical structures, their acoustic properties have not been comprehensively evaluated. To address this gap, an experimental protocol was developed to assess the ultrasound behavior of J5 DAP-printed materials. This study aims to determine the suitability of various material combinations for achieving desired echogenic responses.

To evaluate acoustic compliance, simple rectangular test coupons (7.7 cm x 5.3 cm x 1.7 cm), seen in Fig. 3.8, were printed with the J5 DAP, using select combinations of J5 DAP materials created with Stratasys' DAC software. These coupons served as test samples

for ultrasound imaging analysis, providing insight into the relationship between material formulation and echogenicity. The rectangular coupon block provided a sufficient surface area for stable US probe placement, as well as adequate thickness to evaluate material performance under US imaging.

Figure 3.8: Rectangular prism ultrasound test coupons printed with varying J5 DAP material formulations. These samples were used to assess the acoustic properties and echogenicity of different material combinations under ultrasound imaging.

The Stratasys DAC software enables the precise formulation of compatible J5 DAP materials. 'Digital Materials', a predefined infill setting that facilitates the generation of new material combinations at a 100% scale, was utilized to produce the desired formulations for testing. Each test coupon was printed with an encapsulating outer layer composed of 80% ElasticoClear and 20% TissueMatrix to preserve the structure of the soft coupons.

ElasticoClear, Tissue Matrix and GelMatrix, as candidate materials for soft matter production, were evaluated for their acoustic properties. To capture the broad bandwidth of material combinations, both binary and ternary digital materials were formulated. These combinations were designed to span the lower and higher extremes of material contribution within the available range. The higher extremes of GelMatrix are not compatible with the J5 DAP for printing and were omitted from this study.

To investigate the influence of DraftWhite on acoustic properties, the material was incorporated into formulations containing TissueMatrix and GelMatrix in small proportions.

High concentrations of DraftWhite, as a rigid material, produce significantly stiffer materials, undermining the objective of this study to characterize soft, tissue-mimicking materials. Table 3.1 presents 16 different binary and ternary combinations of the four J5 DAP materials for evaluation of their echogenic properties.

Table 3.1: J5 DAP Digital Material Combinations of ElasticoClear, TissueMatrix, GelMatrix and DraftWhite

Sample	**ElasticoClear (%)**	**TissueMatrix (%)**	**GelMatrix (%)**	**DraftWhite (%)**
1	75	0	25	0
2	50	0	50	0
3	0	50	50	0
4	0	75	25	0
5	25	75	0	0
6	50	50	0	0
7	75	25	0	0
8	20	20	60	0
9	34	33	33	0
10	25	25	50	0
11	20	60	20	0
12	60	20	20	0
13	50	25	25	0
14	0	72	13	15
15	0	76	14	10
16	0	80	15	5

For testing, an US probe was placed directly on the surface of each printed coupon using ultrasound gel as a coupling medium. The scans were taken with the Phillips S4-1 phased array transducer, shown in Fig. 3.9, under its 'Abdomen' preset. The transducer produced US Images with arrays coming from a central point with a 90° field of vision. To ensure consistency across scans, US gain was standardized at 60% and depth set to 6 cm for all coupon scans.

Ultrasound imaging was performed by a medically trained professional (MP) with experience in conducting US diagnostic assessments of the RUQ. The professional was asked to

Figure 3.9: The Philips S4-1 phased array ultrasound transducer used for imaging printed test coupons. Scans were performed using the 'Abdomen' preset, with a 90° field of view originating from a central point. Ultrasound gel was applied as a coupling medium, and imaging parameters were standardized with a gain of 60% and a depth of 6 cm.

provide an expert evaluation of each test coupon's ultrasound image, specifically commenting on the similarity of its echogenicity to that of RUQ anatomical structures. The resulting US images were captured and saved for post-processing and analysis. For a comparative study between coupon performance and RUQ US, a de-identified US scan of the liver and kidney was acquired using the same transducer and gain settings as those applied to the test coupons.

3.3.3 Results

The acquired US images of the 16 coupons with formulations outlined in Table 3.1 containing ElasticoClear, TissueMatrix, GelMatrix and DraftWhite are presented in Fig. 3.10. The images were arranged in the Fig. 3.10 according to the materials varied in each coupon. S1 and S2 are split from S3 and S4 in the first row, separating the mixtures of TM:GM on the left from EC:GM on the right. Mixtures TM:EC were placed in the far left column section below S1-S4 and TM:GL:DW mixtures in the far left column. The remaining EC:TM:GM

mixtures were placed in the remaining section within the two center columns of the 4x4 image table. This separation was maintained throughout the study to clearly show difference in intensity between coupon images with specific changes in J5 DAP materials.

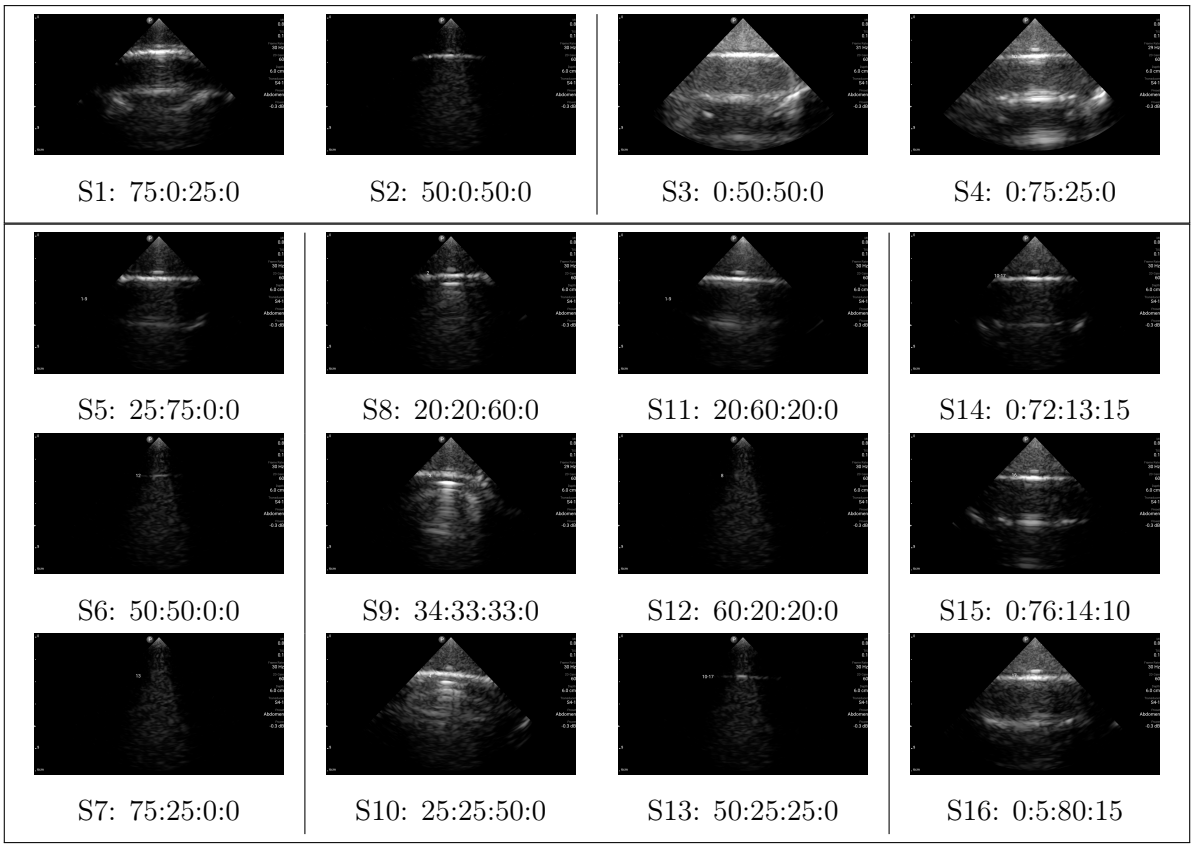

Figure 3.10: Raw ultrasound images of printed test coupons (S1–S16) with varied J5 DAP material ratios of ElasticoClear:TissueMatrix:GelMatrix:DraftWhite (in %). Samples S1–S4 occupy the top row, while subsequent samples are arranged column-wise. The samples are arranged in sections based on the materials that vary within the samples. These images were used for assessing acoustic compliance and echogenicity.

Post-processing and analyses involving all 16 coupons are outlined in this section. Similar processes were used to produce comparable images of liver tissue, renal medulla and renal pelvis US, internal features of the liver and kidney. The processes involving each coupon US image, as well as additional liver and kidney US images, were conducted in MATLAB and are presented in Appendix B.

Coupon Post-Processing

Images were loaded into MATLAB for cropping to a ROI to be analyzed for US image comparison. The raw US image was viewed in Microsoft Paint to determine the pixel-to-cm ratio for each scan, using the scale on the left side of the image to correlate the number of pixels to the scan depth. This allowed us to define a similarly sized ROI for both the human and coupon scans for comparison despite their difference in depth. The US images were cropped to the zero tick mark of the scale, found to be 20 px for all images. The center of the symmetrical and identically sized images was taken as the midpoint of the top of the cropped images. A rectangular ROI of 1 cm x 0.5 cm was defined at a depth of 0.65 cm within each coupon image to quantitatively assess the material's acoustic properties. The ROI only included pixels within the frame of the US scan, removing extraneous artefacts, and centered in the scan to maintain US focus properties. Figure 3.11 shows the cropped US image with outlined ROI designated with a red rectangle.

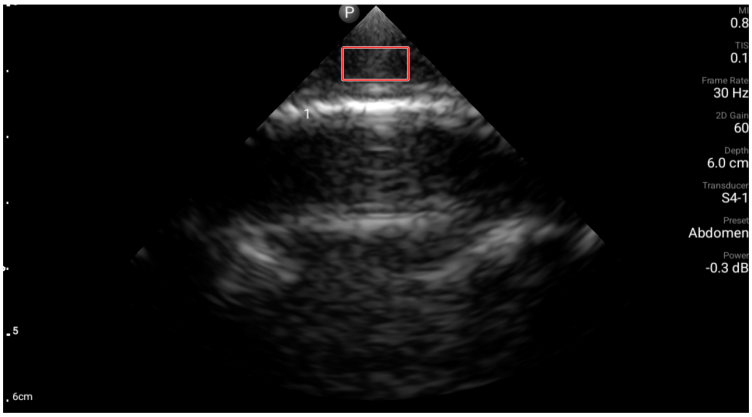

Figure 3.11: Ultrasound (US) image of a test coupon with the designated Region of Interest (ROI) outlined by red rectangle. The ROI measures 1 cm × 0.5 cm and was positioned at a depth of 0.65 cm, based on the image's depth scale. It was selected to isolate relevant ultrasound features of the J5 material coupon samples while excluding external artefacts, enabling consistent comparison between coupons for quantitative analysis of material acoustic properties.

The coupon ROIs were converted to grayscale, and a Gaussian blur was applied to each coupon. The resulting processed ROIs for the 13 coupons were presented in 3.12 below.

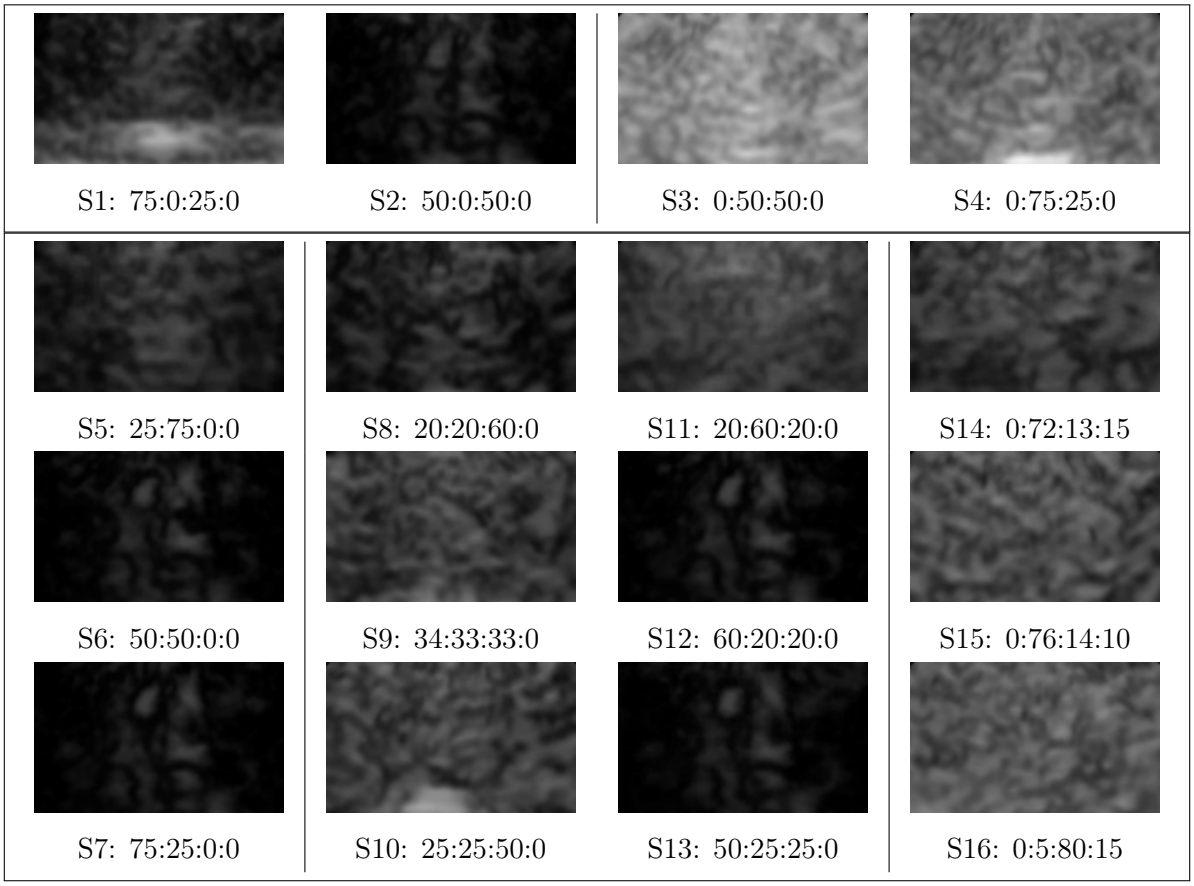

Figure 3.12: Processed ROI images of printed coupons with different J5 DAP material ratios of ElasticoClear:TissueMatrix:GelMatrix:DraftWhite (%) for assessing echogenic properties of RUQ anatomy. Samples S1–S4 occupy the top row, while subsequent samples are arranged column-wise. The samples are arranged in sections based on the materials varied within the samples.

To obtain similar ROIs of the liver tissue, renal pelvis and renal medulla, the ROI dimensions for the coupons were converted to pixels with the pixel-to-cm scale for the human US scan depth. The rectangular ROI was centered in the image to maintain Us focus and array properties across images for consistent image quality. Figure 3.13 shows a sample of the liver, renal pelvis, and renal medulla taken as an ROI for a human anatomy reference to compare printed materials. For consistency in the image processing workflow, the chosen

anatomy ROIs were also converted to grayscale, and a Gaussian blur was applied. MATLAB code used to post-process images is seen in Appendix B.

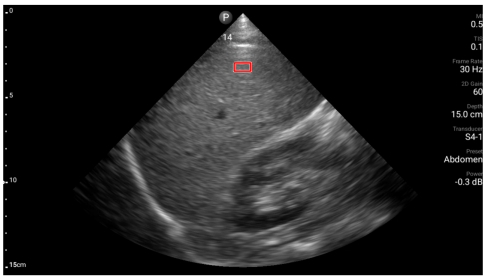

(a) Liver ROI

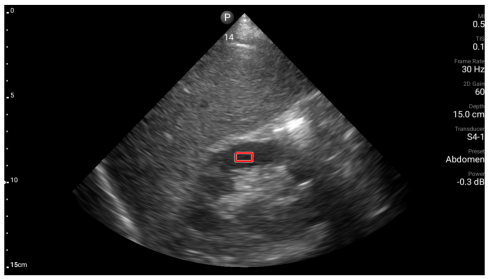

(b) Renal Medulla ROI

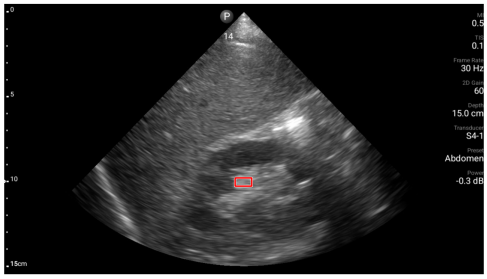

(c) Renal Pelvis ROI

Figure 3.13: US Image Reference ROI (a) liver, (b) renal medulla, and (c) renal pelvis.

Qualitative Assessment of Echogenic Variability in Printed Coupons

To visually assess differences in US image intensity between coupons, pixel-wise grayscale deviation was calculated for each coupon image. These images were obtained by computing the pixel-wise absolute difference between each coupon's ROI ($I_{ROI}(x, y)$) and the pixel-wise mean ROI image ($I_{\mu}(x, y)$) averaged across all coupons, as shown in Equation 3.1,

$$D(x, y) = |I_{ROI}(x, y) - I_{\mu}(x, y)| \tag{3.1}$$

where $D(x, y)$ is the absolute grayscale deviation matrix. Calculations were done in MATLAB and presented in Appendix B. This image enhances visual contrast and reveals

intensity variations between samples more effectively than individual grayscale ROIs alone for qualitative comparison. Figure 3.14 shows the developed images for all 16 coupons.

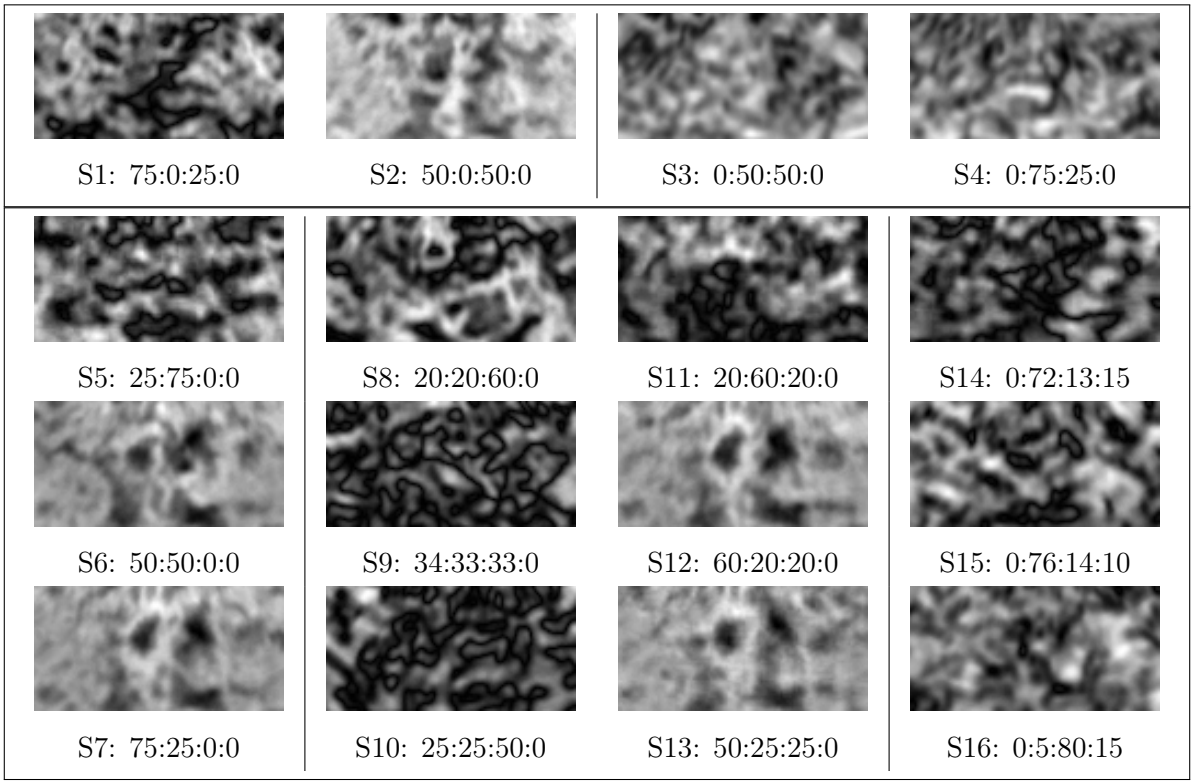

Figure 3.14: Deviation maps for printed test coupons with different J5 DAP material ratios of ElasticoClear:TissueMatrix:GelMatrix:Draftwhite (in %). Top two rows show binary blends, and bottom two rows show ternary blends. Brighter areas represent higher dissimilarity compared to other coupons.

The more similar the images are to one another, the more identical in ultrasound intensity they appear visually. This analysis was able to accentuate US intensity difference between each material. US image intensity was observed to differ for printed material ratios of EC:TM and EC:GM. Ternary mixtures of EC:TM:GM, S12, S8, and S11, all show observable differences in image intensity when one material is the dominant in each mixture. Binary Materials with ratios of TM:GM and ternary materials with less than 28% change in material contribution had no distinguishable differences in material appearance.

The outlined workflow for post-processing and calculating absolute grayscale deviation between printed coupons provided a visual representation of ultrasound (US) intensity differences among the samples. Notably, despite being 3D-printed, coupon layer lines were not visible in the US images, resulting in clean and consistent images of the selected ROIs. This consistency enabled a reliable comparison across samples. The J5 Digital Anatomy Printer sprays, rolls, and cures each print layer, a process that could potentially introduce microstructural variation between layers. However, such non-homogeneous artifacts were not observed in the acquired images, indicating a uniform internal structure suitable for ultrasound imaging.

Echogenicity Comparison Between Coupons and Human RUQ Anatomy

The grayscale average of a US ROI image is a viable scalar metric for evaluating the echogenicity of a material under US [95]. The grayscale mean for each coupon ROI image was determined from finding the mean of all pixel grayscale values in a single US image. In this study, the grayscale mean and corresponding pixel-wise standard deviation of each material ROI image were computed in Ma and compared to those of three RUQ anatomical reference tissues: the liver, renal medulla, and renal pelvis. MATLAB code used to compute the average grayscale intensity and standard deviation for each image is presented in Appendix B. These comparisons were used to assess the acoustic similarity of the 16 printed coupons to human tissue. Figure 3.15 presents a graphical summary of the calculated grayscale means, highlighting the deviation of each coupon's echogenic response relative to the reference anatomical structures, with the desired RUQ anatomical references plotted as dashed lines along the calculated average grayscale axis.

A comparison of average grayscale values for each image with their standard differences graphically displays the variances in US image intensity between coupons. Since echogenic properties are proportional to US image intensity, Fig. 3.15 also compares the echogenic

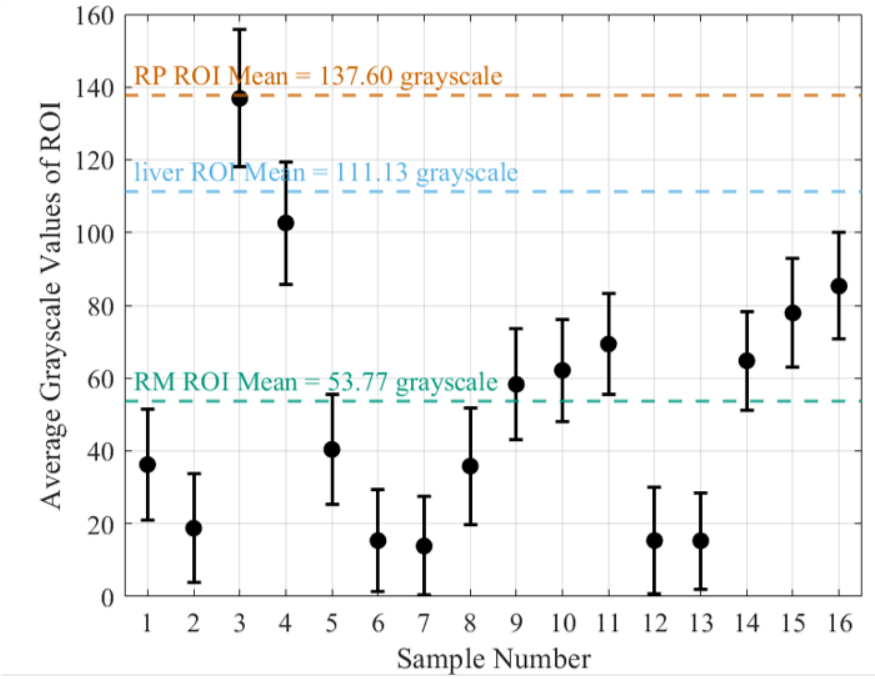

Figure 3.15: Quantitative comparison of average grayscale intensities and standard deviations for each tested J5 DAP material, alongside anatomical reference samples of the renal pelvis, renal medulla, and liver. This analysis was used to assess each material's ability to simulate the echogenic properties of RUQ anatomy for ultrasound imaging applications.

capabilities of each material.Despite the limitations of the J5 DAP printer in achieving uniform material distribution, the printed samples demonstrated consistent pixel-level results, with standard deviation values remaining within a controlled and consistent range between materials.

The MP examined the material coupons and gave notes on each material, stating its echogenic property and potential organ tissue. Furthermore, feedback addressed sound-wave transmission and explained familiar ultrasound artefacts. Table 3.2 provides main takeaways from the MP feedback on coupon performance under US imaging. Transmissive properties were categorized as high-transmits well, medium-transmits, and low-little to no transmission. S3 and S4 were praised for their transmissive behavior, with minimal attenuation of sound waves. These materials would make a great surface interface material, according to the MP. The terms bright and dark were used to distinguish significant differences in samples stated by MP. The 'very hypoechoic' group exhibited extremely low image intensity, approaching

Table 3.2: Echogenic and Transmission Properties of J5 DAP Material Samples Based on Expert Opinion of Medical.

Echogenic Property	Sample Materials	Potential Anatomic Matches	Transmission
dark hypoechoic	S6, S7, S12, S13	vasculature,bone	low
hypoechoic	S1, S2, S5, S8, S14	Liver cist,renal medulla,renal pyramid,spleen	medium
hyperechoic	S3, S4	liver, renal pelvis, renal calcytes	high
isoechoic	S11	spleen, soft tissue	low
isoechoic	S9, S10	spleen, soft tissue	medium
bright isoechoic	S16, S17	muscular and abdominal wall, soft tissues, spleen	medium

levels typically associated with anechoic regions, which are characterized by the absence of returning echoes due to complete transmission of sound waves. Similarly, 'bright isoechoic' were coupons that portrayed isoechoic properties but were explicitly stated to be more hyperechoic than the isoechoic group.

These groupings of coupons acknowledged by the MP lie within a similar ranges on the average grayscale axis seen in Fig. 3.15. To further illustrate this, the sample order in Fig. 3.15 was rearranged to match Table 3.2 by grouping samples with similar echogenic properties were grouped and presented on Fig. 3.16.

Figure 3.16 illustrates the correlation between the average grayscale of a US image and echogenic properties denoted by the MP for each coupon correlating to distinct region of average grayscale values with no overlapping max thresholds. This identifies possible ranges in average gray scale values within which materials can be identified as having a specific echogenic property. Based on the evaluation of the MP and the result of this study, the scale is steep, requiring large jumps to make clear distinctions in echogenic properties.

3.3.4 Discussion

The goal of this study is to explore the similarities and distinctions across various J5 DAP material combinations. As shown in Figure 3.14, variations in image intensity between materials are visually evident. These observations were confirmed through both average grayscale measurements and expert assessment. The results offer a practical basis

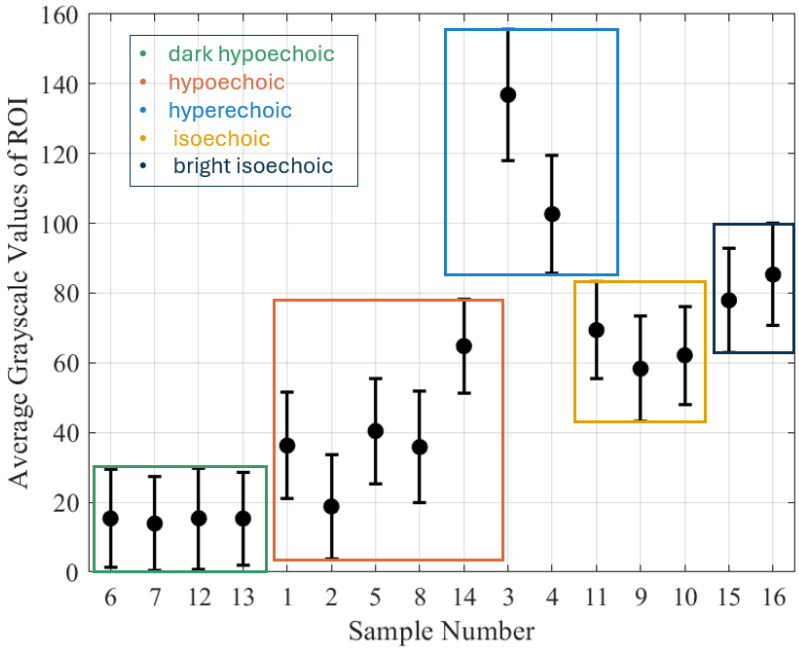

Figure 3.16: Average grayscale values of J5 DAP material samples rearranged and grouped according to echogenic similarity, as classified by the medical professional (MP) and detailed in Table 3.2.This visualization highlights the alignment of grayscale intensity ranges among similarly performing materials for ultrasound simulation.

for material selection depending on the contrast requirements of the intended ultrasound simulation application.

Both average grayscale and pixel-wise deviation in Fig. 3.15 and Fig. 3.14, respectively, showed similar trends with changes in material ratios. The pixel-deviation method provided a visual representation of the changes, while the average grayscale method gave a graphical method of showing differences. The graphical method allowed for comparison between material and reference images of the renal medulla, liver and renal pelvis. For mimicking RUQ ultrasound the J5 DAP material was found to have desired echogenic properties for the assessed anatomy. From Fig. 3.15, the renal pelvis and liver could be represented using S3 or S4, respectively. These samples consist of TissueMatrix(%):GelMatrix(%) with 50:50 and 75:25 combinations, respectively. Gelmatrix and Tissue Matrix combinations are viable for hyperechoic simulation. These materials form a material that can be compared to that of liver tissue stiffness [96]. With only a 10% variation from Stratasys' tested liver preset

at TM(%):GM(%) 85:15, J5 DAP materials demonstrated potential for replicating both ultrasound imaging characteristics and appropriate surface stiffness of the liver, required for realistic anatomic modeling. This result was verified by expert opinion at the time of scans. The medical professional stated that S3 and S4 produced US images similar to expected liver tissue, yielding the most hyperechoic imagery of all material samples. This clear distinction is also observed in 3.15 as S3 and S4 have a significantly higher grayscale average than other material samples. While there is a difference in average grayscale between S3 and S4, the MP expressed that there is a minor difference between the two materials.

Using Fig. 3.15 and validation from expert opinion, the renal medulla could be simulated with S5, S9, S10, and S14. A process for elimination was undergone to determine the best material composition for simulation. The MP stated that S14, a mix of GelMatrix, TissueMatrix, and Draftwhite, produced an image that was too hyperechoic for the simulation, despite being in range. Based on transmissive behavior presented in Table 3.2, all remaining prospects for renal medulla simulation exhibited acoustic wave propagation through the material. However, S5,containing ElasticoClear at 25% and TissueMatrix at 75%, was determined by the MP to be most transmissive, showing artefacts more distinctly within the image. Furthermore, S5 appeared more hypoechoic in comparison to S9 and S10, aligning more accurately with the echogenic profile expected of the renal medulla. This conclusion was corroborated by the MP, who confirmed S5 as the most appropriate material for renal medulla simulation in US applications.

For RUQ ultrasound simulation, materials with high acoustic transmission are preferred, as they allow sound waves to travel deeper with minimal attenuation, enabling clearer imaging of deeper anatomical structures. Figure 3.17 presents the samples chosen for echogenic simulation of the renal medulla, renal pelvis, and liver, showing their average grayscale values relative to the expected averages for each tissue type.

The inclusion of ElasticoClear in a mixture appears to drive echogenic properties towards being more hypoechoic. High proportions of ElasticoClear within a mixture produced

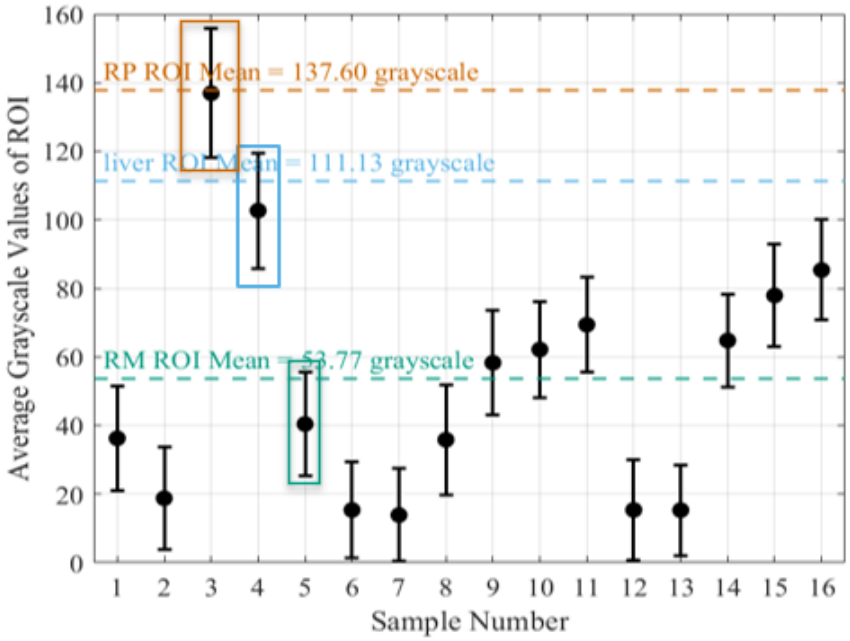

Figure 3.17: Samples S03, S04, and S05 were selected to simulate the renal pelvis, liver, and renal medulla, respectively, based on their average grayscale performance and evaluation by a medical professional. These samples demonstrated grayscale values closely aligned with the expected echogenic properties of each corresponding tissue type.

similar average grayscale values as S6, S7, S12, and S13, all of which contain more than 50% contribution of ElasticoClear. In contrast, the remaining materials contain more hyperechoic features, with ElasticoClear as a non-dominant material in the mixture. Further exploring, the mixtures of TM:GM in comparison to other ternary and binary materials with ElasticoClear, were the most hyperechoic, indicating that ElasticoClear has an influence on echogenicity, producing hypoechoic material.

With closer examination, the resulting US image intensity of ElasticoClear material variation differs per mixture composition. That is, ElasticoClear's impact on US intensity when mixed with other J5 DAP material varies when mixed with TissueMatrix than the ternary mixture option of EC:TM:GM. However, materials that included ElasticoClear had high acoustic impedances, heavily attenuating sound waves and obstructing the visibility of artefacts below. This is not ideal for these materials to be used to model large superficial tissue or organs for an US manikin. These materials may still be useful in simulating small

hypoechoic organs, fluid regions, bones, and specific hypoechoic abnormalities like liver cysts or abscesses.

The inclusion of DraftWhite into a GelMatrix and TissueMatrix mixture, as shown in Fig. 3.15, resulted in materials with more hypoechoic properties. Samples containing DraftWhite fell within the hypoechoic to isoechoic range, which aligns with expectations, given that DraftWhite is a rigid and dense material. Analysis of mean grayscale intensity, pixel-wise standard deviation, and mechanical properties (MP) revealed a slight increase in ultrasound (US) image intensity corresponding to a 5% reduction in DraftWhite content (from 15% to 5%). While DraftWhite-modified materials may be suitable for fine-tuning ultrasound intensity, their limited contrast in mechanical properties suggests they would not be effective for distinguishing between different anatomical structures.

With potential material options for mimicking echogenicity of liver tissue, renal pelvis and renal medulla determined, it is key to assess the interfacing of these materials. While the materials show similar echogenic properties to anatomy when individually evaluated under ultrasound, sound waves must be able to transmit through superficial anatomic structures to visualize deeper anatomic structures. As a preliminary assessment, echogenic materials with medium to high transmissive properties were placed on top of each other with US gel between them to eliminate air gaps and viewed under US. Fig. 3.18 visually demonstrates a difference in US intensity before and after samples S11 and S15 swap positions. This difference was attributed to the acoustic impedance of the material, which attenuates sound waves as they pass through the material.

Investigations into the effects of remaining J5 DAP materials, support material and BoneMatrix, as well as different available DAC infills, may lead to improved interfaces between materials. A different internal print structure of materials, as well as the addition of new materials, will change its mechanical properties and, in turn, its US image properties. A change in the layout of rigid and soft materials within a print may alter how sound

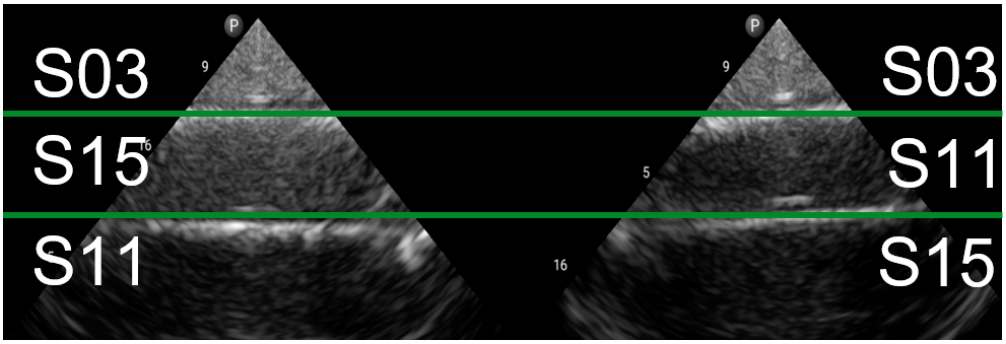

Figure 3.18: Preliminary assessment of select J5 DAP—S03 (high transmission), S15 (medium transmission), and S11 (low transmission)—to evaluate material interfacing and acoustic impedance through stacked echogenic materials. Samples were stacked with ultrasound gel applied between them to eliminate air gaps. The figure illustrates a noticeable difference in US intensity before and after the positions of S11 (low transmission) and S15 (medium transmission) were swapped.

waves propagate through the material, changing the transmissive capabilities of each material, while remaining materials may produce similar echogenic behaviors to materials tested in this study, with better transmissive behaviors.

With the acquired knowledge of J5 DAP materials under US from this study, select materials can be considered to have similar echogenic properties but altered impedance due to differences in print material combination techniques. Similarly, material hardness may be changed while retaining some echogenic properties.

Since the softer materials printed by the J5 DAP exhibit minimal variation in ultrasound appearance across different compositions, a trade-off must be made between material hardness and ultrasound compatibility. The incorporation of rigid materials may improve structural properties but can diminish surface compliance, potentially compromising the material's ability to replicate the behavior of soft tissue.

3.4 Conclusion

This chapter explored the development of an RUQ manikin for POCUS training, focusing on both anatomical modeling and material evaluation for ultrasound simulation. Existing US phantoms, commonly made from silicone or hydrogels, often require additives to achieve

sufficient echogenicity or suffer from inadequate structural integrity. To address these limitations, an approach was presented that uses 3D Slicer, TotalSegmentator, and Zygote to generate anatomically accurate models from CT data. This methodology supports internal organ modeling—specifically of the liver and kidney—and contributes to the limited body of work documenting detailed procedures for anatomical phantom development.

This study sought to investigate the capabilities of the J5 DAP to exhibit US properties if the RUQ using soft materials. Material evaluation through average grayscale and pixel-wise average grayscale analysis of US images revealed that J5 DAP materials can simulate human soft tissue within the RUQ under US. Material mixtures of GelMatrix(75%):TissueMarix(25%),GelMatrix(75%):TissueMarix(25%), and ElasticoClear(25%): TissueMatrix(75%) were selected as prospect simulants of liver, renal pelvis and renal medulla, respectively. Preliminary assessment of material contributions to echogenic properties was undertaken, revealing ElasticoClear and DraftWhite as hypoechoic image generators. ElasticoClear had a noticeable impact, contributing to the formation of near anechoic images.In conclusion,the J5 DAP is capable of creating soft echogenic materials with properties commonly observed in US imaging of RUQ anatomy, answering the question this study sought to investigate. However, limitations in sound-wave propagation through materials suggest that additional materials or modified formulations are needed to achieve balance. This study focused on the acoustic and US properties of J5 DAP materials. To ensure there is a balance between compliance and fidelity, further work needs to be done on the hardness and structural integrity of each material.

Future work should include refining trends in US-compatible materials to examine individual material control over echogenic properties, as well as mechanical testing to ensure structural robustness. With an assessment of individual US capabilities, interfacing between select materials must also be considered for assessment of sound-wave transmission.

With validated materials and refined modeling techniques, the integration of these components can support the creation of fully anthropomorphic, additively manufactured US manikins—advancing simulation-based training in clinical education.

Chapter 4

Conclusion

Manikins play a critical role in supporting the development of rehabilitation robotics and medical training by offering a safe and repeatable platform for practicing human-interactive procedures, reducing the risk to patients in high-stakes environments. Manikins and Simulators must have high anatomical fidelity as well as compliance for realistic simulation. Advances in 3D-printing technology have enabled the rapid fabrication of anatomically accurate manikins with complex geometries and a range of mechanical properties for hard and soft human tissues. Among these technologies, the polyjet Stratasys J5 DAP stands out for its ability to print multiple materials simultaneously, allowing for the integration of diverse tissue-like properties within a single, cohesive structure.

This thesis contributed to the development of a biomechanically and anatomically accurate hand manikin for and index finger PIP joint for exoskeleton validation and a RUQ POCUS simulator featuring echogenic characteristics suitable for US simulation. In Chapter 2, a 3D-printed PIP joint model with anatomical features,derived from MRI, was presented, but failed to meet desired compliance after preliminary assessment. Void-infused TPU showed the ability of void parameters to change the elastic properties of void-infused soft material,characterized by analyzing stress-strain behavior derived from tensile displacement testing using an Instron mechanical tester.Chapter 3 assessed the capabilities of J5 DAP materials for US imaging simulation after presenting a methodology for rapidly creating 3D models with internal organ structures for printing. The echogenic properties of the J5 DAP materials were evaluated by measuring the average image intensity and pixel-wise standard deviation from captured US images and found to have desired echogenic properties.

4.1 Anthropomorphic Hand Manikin

With the rise in limb sensory loss among stroke patients, exoskeleton designers are increasingly developing wearable robots to alleviate the burden on healthcare professionals during rehabilitation. These exoskeleton designers tend to use themselves or small participant pools for exoskeleton validation, potentially compromising safety during development and future patient use. To address this, a passive instrumented manikin is proposed as an intermediate testing solution, enabling developers to refine control models prior to live patient trials.

Current passive instrumented manikins are typically additively manufactured for rapid prototyping, but they often lack anatomical accuracy. Instead, they achieve compliance through mechanical mechanisms incorporating composite rubbers and steel springs. that a more anatomically accurate passive model would better replicate the biomechanical properties of human finger joints, resulting in improved dexterity.

Preliminary assessments of hand compliance indicated that the selected material required higher stiffness. Void-infused soft-material,in this case TPU, was evaluated as a potential alternative method for achieving compliant material. Void parameters were determined to affect the elastic properties of soft 3D print material the via stress-strain comparison from uniaxial tensile testing of TPU. Nijaflex TPU, both with and without engineered voids, was found to be insufficient for simulating ligament elastic properties when compared.Designers of anthropomorphic manikins must carefully balance anatomical fidelity and functional performance as void-infused J5 DAP material may desire changes in anatomical appearance after creation of a model for using void parameters to produce desired elastic performance.

4.2 RUQ POCUS Simulator

Trainees must become proficient in both the operational environment and technical skills associated with POCUS. Simulators are widely used to provide a risk-free environment for

developing these competencies. However, virtual simulators are expensive and often lack realism. Physical simulators, commonly fabricated from silicone or hydrogels, involve time-intensive manufacturing processes and require specialized handling to produce or maintain echogenicity and structural integrity.

It was proposed that an anthropomorphic, additively manufactured manikin be used as a rapid, cost-effective solution for developing RUQ ultrasound training models. Physical manikins provide trainees with a tactile, hands-on learning experience. With additive manufacturing, the cost per unit can be reduced for large cohorts, since changes in pathology only require reprinting individual components rather than fabricating entirely new manikins.

This study presented a methodology for generating anatomically accurate RUQ models with internal features from CT data using 3D Slicer, an open-source medical imaging software. This workflow enables designers to efficiently and rapidly create custom pathologies from medical imaging for use in physical manikins.

Before fabrication, this study determined that the mixtures of TissueMatrix, GelMatrix, ElasticoClear, and Draftwhite of the J5 DAP have suitable echogenic properties for simulating RUQ human anatomy. This was assessed based on qualitative analysis of the grayscale deviation between the tested material and quantitative analysis comparing the average grayscale of coupon ROIs to liver, renal pelvis, and renal medulla sample ROIs, and expert opinion. Binary formulations with GelMatrix and TissueMatrix were determined to be the best materials for US simulation, achieving the desired echogenicity, and acoustic impedance. However, image analysis and expert opinion indicated that changes in material composition do not result in significant shifts in US intensity. Draftwhite and ElasticoClear contributed to creating hypoechoic materials while GelMatrix and TissueMatrix together form a hypoechoic materials. However, materials containing ElasticoClear and Draftwhite had observable effects on wave propagation attributed to the acoustic impedance of the material, preventing sound waves from passing with limited attenuation. The J5 DAP Materials also showed potential for matching anatomy echogenicity with EC(25):TM(75)(in %)

closely resembling the renal medulla TM(75):GM(25) (in %) resembling liver tissue and and TM(50):GM(50)(in %) resembling the renal pelvis. These finding indicate that J5 DAP materials are capable of simulating echogencity of RUQ anatomy.

4.3 Future Works

4.3.1 Anthropomorphic Hand Manikin

Future work requires further analysis of 3D-printed soft material to assess trends and validate the effects of void parameters on their elastic behavior. With the successful answer to the proposed research question, the J5 DAP materials, which exhibit a wide range of elastic properties, can be evaluated for their mechanical performance with void infusion. The findings from this assessment could facilitate the optimization of material compliance, allowing for the development of 3D-printed anatomical finger models that more accurately replicate finger biomechanics.

The joint stiffness of the developed finger model must be experimentally evaluated to characterize its compliance across the PIP hinge joint. Passive joints are typically expected to exhibit a double-exponential joint torque response [25]. Through experimental testing, the biomechanical performance of the model can be validated and compared to existing designs. This data will give insight into adjustments to material properties or anatomical structures to achieve desired joint compliance.

Following the achievement of compliant joint behavior, a position sensor must be integrated into the joint model and calibrated to accurately measure joint angles, without disrupting anatomical features. Contactless sensing methods, such as Hall effect sensors paired with low-force magnets, offer a viable solution. These sensors provide low-friction, low-interference measurements and require minimal space, making them suitable for embedding within compact joint structures.

Once the sensor is incorporated, the external anthropomorphic cover can be applied to the model, and its overall performance assessed.The resulting instrumented joint would retain

biomechanical accuracy, enabling motion tracking and validation of the exoskeleton control models. This framework could then be extended to additional finger joints, contributing toward the development of a fully instrumented anthropomorphic hand manikin.

4.3.2 RUQ POCUS Simulator

To advance the development of a RUQ manikin for POCUS using the J5 DAP, the interface between materials required to make specific anthropomorphic models and the manikin assembly of organs must be investigated. This study focused on the echogenic performance of individual materials; however, during a typical ultrasound scan, sound waves traverse multiple tissue layers, and thus material interfaces must be considered for US simulation. A preliminary assessment showed that materials with ElasticoClear and DraftWhite observably affect wave transmission. A more in-depth examination of select material interfaces is necessary to inform precise adjustments in material composition for improved wave propagation. BoneMatrix and Support materials will be conducted to evaluate them as potential substitutes for rigid materials in formulations. The addition or substitution of these materials could create similar echogenic and mechanical properties, but different acoustic impedance.

Additionally, the selected soft material formulations for representing specific acoustic properties must be evaluated for their hardness and tactile similarities to human anatomy, to inform the appropriate material designation for realism. Identifying and characterizing modifier materials for tuning stiffness and echogenicity will support the development of novel compositions that more closely replicate the mechanical behavior and ultrasonics of real tissue. Echogenic materials derived from this process can then be applied to RUQ models to replicate realistic POCUS experiences and, even further, inspire the creation of other manikins for procedures incorporating US.

Further research is needed to refine material formulations and fabrication techniques that preserve structural integrity while achieving the desired echogenic properties for anatomical models printed with a polyjet printer, such as the J5 DAP. In particular, the behavior of

fluid simulant for anechoic features must be characterized to optimize the realism of a RUQ simulator. The overarching goal is to develop anatomically accurate and acoustically realistic models that support widespread effective training in POCUS.

With US compliance achieved, generated models can be printed and assembled in a designed anthropomorphic containment unit to house the RUQ models in their correct anatomical positions. The unit will provide a realistic interface with features resembling human body extremities. This unit should prioritize modularity, allowing for non-trivial pathology swaps within the simulator—an improvement over current static physical models. Additionally, suitable fluid simulator must be selected that do not degrade model materials and allow ultrasound waves to propagate without significant signal interference.

The successful fabrication of a high-fidelity, anatomically detailed 3D-printed simulator should be evaluated for its successful interfacing with materials. The acoustic properties of materials can be altered depending on the materials superficial to them. At this scale, an effective simulator will provide a cost-effective and rapidly produced training solution. Such a manikin would be well-suited for large training cohorts and adaptable to various clinical scenarios, representing a significant advancement in multi-functional POCUS simulation.

4.4 Conclusion

In this study, a 3D-printed anthropomorphic hand model incorporating anatomical features was developed, and void-infused TPU was evaluated for its potential to achieve joint compliance, as discussed in Chapter 2. This work aimed to simulate biomechanical performance within an exoskeleton testbed. Additionally, Chapter 3 explored the echogenic capabilities of soft 3D-printable materials using the J5 Digital Anatomy Printer to simulate RUQ anatomy, with the goal of developing a RUQ ultrasound manikin for POCUS training.

There exists an inherent trade-off between anatomical fidelity and mechanical compliance in the development of medical manikins. High-fidelity, anatomically accurate manikins typically require substantial financial investment and time to produce, whereas compliant

manikins—though less precise in physical and tactile realism—offer advantages in functional performance and adaptability. Achieving a balance between these properties presents an opportunity for innovative modeling approaches, particularly through the use of polyjet printing technologies.

The J5 Digital Anatomy Printer, which enables the simultaneous printing of materials with varying mechanical and acoustic properties, offers a promising solution for optimizing both compliance and anatomical fidelity. While other additive manufacturing techniques and materials can be considered for their compliant characteristics, they often compromise anatomical accuracy. By leveraging the capabilities of the J5 DAP and related multi-material printing technologies, more anthropomorphic and functionally accurate models can be developed to advance applications in rehabilitation and medical simulation.

Bibliography

[1] K. Navindaran, J. S. Kang, and K. Moon, "Techniques for characterizing mechanical properties of soft tissues," *J. Mech. Behav. Biomed. Mater.*, vol. 138, p. 105 575, Feb. 2023. DOI: 10.1016/j.jmbbm.2022.105575.

[2] M. Wegner and D. Krause, "3d printed phantoms for medical imaging: Recent developments and challenges," *J. Mech. Sci. Technol.*, vol. 38, no. 9, pp. 4537–4543, Sep. 2024. DOI: 10.1007/s12206-024-2407-8.

[3] M. V. Weghe, M. Rogers, M. Weissert, and Y. Matsuoka, "The act hand: Design of the skeletal structure," in *Proc. IEEE Int. Conf. Robot. Autom. (ICRA)*, vol. 4, New Orleans, LA, USA, Apr. 2004, pp. 3375–3379. DOI: 10.1109/ROBOT.2004.1308775.

[4] V. Anwari, A. Lai, A. Ursani, *et al.*, "3d printed ct-based abdominal structure mannequin for enabling research," *3D Print. Med.*, vol. 6, no. 1, p. 3, Feb. 2020. DOI: 10.1186/s41205-020-0056-9.

[5] Z. Xu, V. Kumar, Y. Matsuoka, and E. Todorov, "Design of an anthropomorphic robotic finger system with biomimetic artificial joints," in *Proc. 4th IEEE RAS & EMBS Int. Conf. on Biomedical Robotics and Biomechatronics (BioRob)*, Rome, Italy, Jun. 2012, pp. 568–574. DOI: 10.1109/BioRob.2012.6290710.

[6] T. M. Bücking, E. R. Hill, J. L. Robertson, E. Maneas, A. A. Plumb, and D. I. Nikitichev, "From medical imaging data to 3d printed anatomical models," *PLoS ONE*, vol. 12, no. 5, e0178540, May 2017. DOI: 10.1371/journal.pone.0178540.

[7] A. J. Sparks, C. M. Smith, A. B. Allman, *et al.*, "Compliant vascular models 3d printed with the stratasys j750: A direct characterization of model distensibility using intravascular ultrasound," *3D Print. Med.*, vol. 7, no. 1, p. 28, Sep. 2021. DOI: 10.1186/s41205-021-00114-8.

[8] L. Tian, J. Zheng, N. M. Thalmann, *et al.*, "Design of a single-material complex structure anthropomorphic robotic hand," *Micromachines*, vol. 12, no. 9, p. 1124, Sep. 2021. DOI: 10.3390/mi12091124.

[9] J. Meyer-Szary, M. S. Luis, S. Mikulski, *et al.*, "The role of 3d printing in planning complex medical procedures and training of medical professionals — cross-sectional multispecialty review," *Int. J. Environ. Res. Public Health*, vol. 19, no. 6, p. 3331, Mar. 2022. DOI: 10.3390/ijerph19063331.

[10] A. Marro, T. Bandukwala, and W. Mak, "Three-dimensional printing and medical imaging: A review of the methods and applications," *Curr. Probl. Diagn. Radiol.*, vol. 45, no. 1, pp. 2–9, Jan. 2016. DOI: 10.1067/j.cpradiol.2015.07.009.

[11] O. S. Nesheim, T. L. Steffensen, M. Steinert, and C. W. Elverum, "3d printing gelatin ultrasound phantoms: Observations, challenges and future research," in *Proc. NordDesign 2024*, Reykjavik, Iceland, Aug. 2024.

[12] A. Pacioni, M. Carbone, C. Freschi, R. Viglialoro, V. Ferrari, and M. Ferrari, "Patient-specific ultrasound liver phantom: Materials and fabrication method," *Int. J. Comput. Assist. Radiol. Surg.*, vol. 10, no. 7, pp. 1065–1075, Jul. 2015.

[13] J. D. Krech, T. Wyatt, and D. J. Harmon, "Systematic review of 3d-printed ultrasound-able models in graduate medical education," *J. Ultrasound Med.*, vol. 44, no. 4, pp. 595–603, Apr. 2025. DOI: 10.1002/jum.16624.

[14] Y. Zhu, G. Wei, L. Ren, Z. Luo, and J. Shang, "An anthropomorphic robotic finger with innate human-finger-like biomechanical advantages, part i: Design, ligamentous

joint, and extensor mechanism," *IEEE Trans. Robot.*, vol. 39, no. 1, pp. 485–504, Feb. 2023. DOI: 10.1109/TRO.2022.3200006.

[15] V. Lemarteleur, M. Peycelon, J.-L. Sablayrolles, P. Plaisance, A. El-Ghoneimi, and P.-F. Ceccaldi, "Realization of open software chain for 3d modeling and printing of organs in simulation centers: Example of renal pelvis reconstruction," *J. Surg. Educ.*, vol. 78, no. 1, pp. 232–244, 2021. DOI: 10.1016/j.jsurg.2020.06.035.

[16] A. Harynska, I. Gubanska, J. Kucinska-Lipka, and H. Janik, "Fabrication and characterization of flexible medical-grade tpu filament for fused deposition modeling 3dp technology," *Polymers*, vol. 10, no. 12, p. 1304, Nov. 2018. DOI: 10.3390/polym10121304.

[17] Stratasys Ltd., *J5 digital anatomy 3d printer*, Online, Product Information Brochure, Eden Prairie, MN, USA, 2025. [Online]. Available: https://support.stratasys.com/en/Printers/PolyJet/J5-Digital-Anatomy-Printer.

[18] H. Kamalinia, M. Bonnevay, A. Barbarulo, E. Vennat, and B. Tie, "Numerical and experimental study of echogenicity in 3d-printed tissue-mimicking materials," *Ultrasonics*, vol. 148, p. 107 518, Apr. 2025. DOI: 10.1016/j.ultras.2024.107518.

[19] C. G. Rose and M. K. O'Malley, "Hybrid rigid-soft hand exoskeleton to assist functional dexterity," *IEEE Robot. Autom. Lett.*, vol. 4, no. 1, pp. 73–80, Jan. 2019. DOI: 10.1109/LRA.2018.2879850.

[20] T. Todsen, J. Melchiors, B. Charabi, *et al.*, "Reliable and valid assessment of point-of-care ultrasonography," *Annals of Surgery*, vol. 261, no. 2, pp. 309–315, Feb. 2015. DOI: 10.1097/sla.0000000000000552. [Online]. Available: https://doi.org/10.1097/sla.0000000000000552.

[21] M. Zheng, B. Wang, J. Huang, and J. Barbič, "Simulation of hand anatomy using medical imaging," *ACM Trans. Graph.*, vol. 41, no. 6, pp. 1–20, Nov. 2022. DOI: 10.1145/3550454.3555486.

[22] A. Saudabayev and H. A. Varol, "Sensors for robotic hands: A survey of state of the art," *IEEE Access*, vol. 3, pp. 1765–1782, 2015. DOI: 10.1109/ACCESS.2015.2482543.

[23] G. Langevin, *Inmoov hand project*, https://inmoov.fr/inmoov-hand/, Accessed: 2025-08-04, 2024.

[24] The Shadow Robot Company, *Shadow dexterous hand series*, https://shadowrobot.com/, Accessed: 2025-08-04, 2025.

[25] P.-H. Kuo, J. DeBacker, and A. D. Deshpande, "Design of robotic fingers with human-like passive parallel compliance," in *Proc. IEEE Int. Conf. Robot. Autom. (ICRA)*, Seattle, WA, USA, May 2015, pp. 2562–2567. DOI: 10.1109/ICRA.2015.7139543.

[26] D. I. of Robotics and Mechatronics, *Building a super robust robot hand*, IEEE Spectrum article, 2025.

[27] B. Fang, F. Sun, Y. Chen, C. Zhu, Z. Xia, and Y. Yang, "A tendon-driven dexterous hand design with tactile sensor array for grasping and manipulation," in *2019 IEEE International Conference on Robotics and Biomimetics (ROBIO)*, 2019, pp. 203–210. DOI: 10.1109/ROBIO49542.2019.8961671.

[28] A. D. Deshpande, Z. Xu, M. J. V. Weghe, *et al.*, "Mechanisms of the anatomically correct testbed hand," *IEEE/ASME Trans. Mechatronics*, vol. 18, no. 1, pp. 238–250, Feb. 2013. DOI: 10.1109/TMECH.2011.2166801.

[29] Z. Xu and E. Todorov, "Design of a highly biomimetic anthropomorphic robotic hand towards artificial limb regeneration," in *Proc. IEEE Int. Conf. Robot. Autom. (ICRA)*, Stockholm, Sweden, May 2016, pp. 3485–3492. DOI: 10.1109/ICRA.2016.7487528.

[30] P.-H. Kuo and A. D. Deshpande, "Muscle-tendon units provide limited contributions to the passive stiffness of the index finger metacarpophalangeal joint," *J. Biomech.*, vol. 45, no. 15, pp. 2531–2538, Oct. 2012. DOI: 10.1016/j.jbiomech.2012.07.034.

[31] A. A. M. Faudzi, J. Ooga, T. Goto, M. Takeichi, and K. Suzumori, "Index finger of a human-like robotic hand using thin soft muscles," *IEEE Robot. Autom. Lett.*, vol. 3, no. 1, pp. 92–99, Jan. 2018. DOI: 10.1109/LRA.2017.2732059.

[32] J. A. E. Hughes and et al., "An anthropomorphic soft skeleton hand exploiting conditional models for piano playing," *Sci. Robot.*, vol. 3, no. 25, eaau3098, Jun. 2018. DOI: 10.1126/scirobotics.aau3098.

[33] V. K. Nanayakkara, G. Cotugno, N. Vitzilaios, D. Venetsanos, T. Nanayakkara, and M. N. Sahinkaya, "The role of morphology of the thumb in anthropomorphic grasping: A review," *Frontiers in Mechanical Engineering*, vol. 3, p. 5, Jun. 2017. [Online]. Available: https://doi.org/10.3389/fmech.2017.00005.

[34] A. Baskaran, P. Esmatloo, M. Times, A. D. Deshpande, C. G. Rose, and et al., "An anthropomorphic passive instrumented hand for validating wearable robotic systems," in *Proc. IEEE/ASME Int. Conf. Adv. Intell. Mechatronics (AIM)*, Delft, Netherlands, Jul. 2021, pp. 134–139. DOI: 10.1109/AIM46487.2021.9517589.

[35] K. Agrawal and et al., *Textbook of Plastic, Reconstructive, and Aesthetic Surgery*. 2018. DOI: 10.1055/b-0042-186316.

[36] C. Hacking, *Ligaments of the fingers (gray's illustration)*, Radiopaedia.org, case study, Sep. 2024. [Online]. Available: https://doi.org/10.53347/rID-84587.

[37] M. Tebyani, A. Robbins, W. Asper, *et al.*, "3d printing an assembled biomimetic robotic finger," in *Proc. 17th Int. Conf. Ubiquitous Robots and Ambient Intelligence (URAI)*, Kyoto, Japan, Jun. 2020, pp. 526–532. DOI: 10.1109/UR49135.2020.9144774.

[38] D. D. Wilkinson, M. V. Weghe, and Y. Matsuoka, "An extensor mechanism for an anatomical robotic hand," in *Proc. 2003 IEEE Int. Conf. Robot. Autom. (ICRA)*, Taipei, Taiwan, Sep. 2003, pp. 238–243.

[39] R. Pioletti, L. Rütz, and P. R. Rakotomanana, "Strain rate effect on the mechanical behavior of the anterior cruciate ligament–bone complex," *Medical Engineering & Physics*, vol. 21, no. 2, pp. 95–100, 1999. DOI: 10.1016/S1350-4533(99)00028-4.

[40] K. Firoozbakhsh, I. S. Yi, M. S. Moneim, and Y. Umada, "A study of ulnar collateral ligament of the thumb metacarpophalangeal joint," *Clinical Orthopaedics and Related Research*, no. 403, pp. 240–247, Oct. 2002. DOI: 10.1097/00003086-200210000-00035.

[41] Y. Yun, P. Agarwal, J. Fox, K. E. Madden, and A. D. Deshpande, "Accurate torque control of finger joints with ut hand exoskeleton through bowden cable sea," in *Proc. IEEE/RSJ Int. Conf. Intell. Robots Syst. (IROS)*, Daejeon, South Korea, Oct. 2016, pp. 390–397. DOI: 10.1109/IROS.2016.7759084.

[42] P. Kuo and A. D. Deshpande, "A novel joint design for robotic hands with humanlike nonlinear compliance," *ASME J. Mech. Robot.*, vol. 8, no. 2, p. 021 004, Apr. 2016.

[43] A. D. Deshpande, N. Gialias, and Y. Matsuoka, "Contributions of intrinsic visco-elastic torques during planar index finger and wrist movements," *IEEE Trans. Biomed. Eng.*, vol. 59, no. 2, pp. 586–594, Feb. 2012. DOI: 10.1109/TBME.2011.2178240.

[44] G. Lee and Y. Choi, "Bio-inspired tendon-driven finger design with isomorphic ligamentous joint," *IEEE Access*, vol. 8, pp. 18 240–18 251, Jan. 2020. DOI: 10.1109/ACCESS.2020.2968739.

[45] I. Gaiser, S. Schulz, A. Kargov, *et al.*, "A new anthropomorphic robotic hand," in *Proc. IEEE-RAS Int. Conf. Humanoid Robots (Humanoids)*, Daejeon, South Korea, Dec. 2008, pp. 418–422. DOI: 10.1109/ICHR.2008.4755992.

[46] M. Grebenstein, M. Chalon, G. Hirzinger, and R. Siegwart, "Antagonistically driven finger design for the anthropomorphic dlr hand arm system," in *Proc. IEEE/RSJ Int. Conf. Intell. Robots Syst. (IROS)*, Taipei, Taiwan, Oct. 2010, pp. 3781–3787. DOI: 10.1109/IROS.2010.5650837.

[47] T. Fidinillah, A. G. Risangtuni, N. K. Putra, V. Virdyawan, S. Suprijanto, and S. M. Putri, "Design of soft pneumatic actuator in hand rehabilitation robot with fem-based modeling," in *Proc. 8th Int. Conf. Instrum., Control, Autom. (ICA)*, Bandung, Indonesia, 2023, pp. 109–113. DOI: 10.1109/ICA58538.2023.10273084.

[48] Z. Xu, Y. Bai, R. Ni, N. Yang, Y. Sun, and P. Qi, "Anthropomorphic soft pneumatic fingers towards full dexterity of human hand," in *Proc. 18th IEEE-RAS Int. Conf. Humanoid Robots (Humanoids)*, Beijing, China, 2018, pp. 381–386. DOI: 10.1109/HUMANOIDS.2018.8625023.

[49] T. Sonoda and I. Godler, "Multi-fingered robotic hand employing strings transmission named 'twist drive'," in *Proc. IEEE/RSJ Int. Conf. Intelligent Robots and Systems (IROS)*, Taipei, Taiwan, Oct. 2010. DOI: 10.1109/IROS.2010.5650837.

[50] S. D. Gollob, J. Poss, G. Memoli, and E. T. Roche, "A multi-material, anthropomorphic metacarpophalangeal joint with abduction and adduction actuated by soft artificial muscles," *IEEE Robot. Autom. Lett.*, vol. 7, no. 3, pp. 5882–5887, Jul. 2022. DOI: 10.1109/LRA.2022.3161714.

[51] S. N. Yousaf, J. C. Abbott, and C. J. Nycz, "Design and characterization of a passive instrumented hand," in *Proc. ASME Dyn. Syst. Control Conf. (DSCC)*, 2019.

[52] F. Dupriez and et al., "Evaluation of point-of-care ultrasound use in the diagnostic approach for right upper quadrant abdominal pain management in the emergency department: A prospective study," *Intern. Emerg. Med.*, vol. 19, no. 3, pp. 803–811, Apr. 2024. DOI: 10.1007/s11739-023-03480-9.

[53] N. Abeysekera, K. A. Whitmore, A. Abeysekera, G. Pang, and K. B. Laupland, "Applications of 3d printing in critical care medicine: A scoping review," *Anaesth. Intensive Care*, vol. 49, no. 3, pp. 164–172, May 2021. DOI: 10.1177/0310057X20976655.

[54] C. F. Dietrich and et al., "The ultrasound use of simulators, current view, and perspectives: Requirements and technical aspects (wfumb state of the art paper)," *Endoscopic Ultrasound*, vol. 12, no. 1, pp. 38–49, Jan. 2023. DOI: 10.4103/EUS-D-22-00197.

[55] N. S. Birbara, J. M. Otton, and N. Pather, "3d modelling and printing technology to produce patient-specific 3d models," *Heart Lung Circ.*, vol. 28, no. 2, pp. 302–313, Feb. 2019. DOI: 10.1016/j.hlc.2017.10.017.

[56] C. Lucius, M. B. Nielsen, M. Blaivas, *et al.*, "The use of simulation in medical ultrasound: Current perspectives on applications and practical implementation (wfumb state-of-the-art paper)," *Endosc. Ultrasound*, vol. 12, no. 3, pp. 311–318, May 2023. DOI: 10.1097/EUS.0000000000000022.

[57] M. L. Østergaard, L. Konge, N. Kahr, E. Albrecht-Beste, M. B. Nielsen, and K. R. Nielsen, "Four virtual-reality simulators for diagnostic abdominal ultrasound training in radiology," *Procedia Computer Science*, vol. 77, pp. 281–287, 2015. DOI: 10.1016/j.procs.2015.12.237.

[58] P. Buń, F. Górski, R. Wichniarek, W. Kuczko, and P. Zawadzki, "Immersive educational simulation of medical ultrasound examination," *Procedia Computer Science*, vol. 75, pp. 186–194, 2015. DOI: 10.1016/j.procs.2015.12.237.

[59] S. Kagbo–Kue, Q. Ngo, T. A. Ajose, and N. Bakinde, "A common presentation of right upper quadrant pain in an uncommon disease: 3020," *American Journal of Gastroenterology*, vol. 113, S1658, Oct. 2018.

[60] C. Ekomaru, *Understanding abdominal divisions/anatomy snippets*, Blog post on 3D4Medical Anatomy Snippets, Accessed: Aug. 2025, 2019. [Online]. Available: https://3d4medical.com/blog/abdominal-divisions.

[61] M. Mencarelli, L. Puggelli, A. Virga, R. Furferi, and Y. Volpe, "Acoustic velocity and stability of tissue-mimicking echogenic materials for ultrasound training phantoms," *J.*

Mater. Sci., vol. 59, no. 15, pp. 6509–6524, Apr. 2024. DOI: 10.1007/s10853-024-09610-8.

[62] V. Dinh, *Renal ultrasound made easy: Step-by-step guide*, Online, Available: https://www.pocus101.com/renal-ultrasound-made-easy-step-by-step-guide/, Jul. 2025.

[63] A. K. P. Lim, I. Grgurevic, and M. Rosselli, "Normal liver anatomy," in *How to Perform a Liver Ultrasound Scan*, 1st. London, U.K.: Imperial College Healthcare NHS Trust, 2023.

[64] S. I. Hernandez-Torres, C. Bedolla, D. Berard, and E. J. Snider, "An extended focused assessment with sonography in trauma ultrasound tissue-mimicking phantom for developing automated diagnostic technologies," *Front. Bioeng. Biotechnol.*, vol. 11, p. 1 244 616, Nov. 2023. DOI: 10.3389/fbioe.2023.1244616.

[65] J. I. Gear, C. Cummings, A. J. Craig, *et al.*, "Abdo-man: A 3d-printed anthropomorphic phantom for validating quantitative sirt," *EJNMMI Phys.*, vol. 3, p. 17, Aug. 2016. DOI: 10.1186/s40658-016-0151-6.

[66] K. Kagaku, *Us-5 fast-acute abdomen phantom "fast/er fan" with sonography for trauma*, Product listing on GTSimulators, Used for FAST training in perihepatic, perisplenic, pelvic, and pericardial regions, 2025.

[67] N. N. Zein, I. A. Hanouneh, P. D. Bishop, *et al.*, "Three-dimensional print of a liver for preoperative planning in living donor liver transplantation," *Liver Transplant.*, vol. 19, no. 12, pp. 1304–1310, Dec. 2013. DOI: 10.1002/lt.23729.

[68] Stratasys Ltd. and Creighton University School of Medicine Radiology Department, *Developing patient-specific, ultrasound-guided breast biopsy models using digital anatomy printer*, Online, Stratasys case study, Omaha, NE, Nov. 2024. [Online]. Available: https://support.stratasys.com/en/Printers/PolyJet/J5-Digital-Anatomy-Printer.

[69] P. Lum and et al., "Robotic devices for movement therapy after stroke: Current status and challenges to clinical acceptance," *Top. Stroke Rehabil.*, vol. 8, no. 4, pp. 40–53, 2002.

[70] C.-Y. Chu and R. M. Patterson, "Soft robotic devices for hand rehabilitation and assistance: A narrative review," *J. Neuroeng. Rehabil.*, vol. 15, no. 1, pp. 1–14, 2018. DOI: 10.1186/s12984-018-0421-2.

[71] Stratasys, *Biomedical modeling case studies*, Online, Jul. 2025. [Online]. Available: https://www.stratasys.com/en/resources/case-studies/biomedical-modeling/.

[72] B. Wang, G. Matcuk, and J. Barbič, *Hand mri dataset*, Online, 2020. [Online]. Available: http://www.jernejbarbic.com/hand-mri-dataset.

[73] Y. Li, M. Wu, Y. Zhang, L. Xu, and J. Yu, *Piano: A parametric hand bone model from magnetic resonance imaging*, Online, arXiv preprint arXiv:2106.10893, 2021. [Online]. Available: https://doi.org/10.48550/arXiv.2106.10893.

[74] Slicer, *Slicer: Free, open source software for medical image processing and 3d visualization*, Online, Oct. 2024. [Online]. Available: https://www.slicer.org.

[75] Axial3D, *3d printing solutions for healthcare*, Online, Available: https://axial3d.com, Oct. 2023.

[76] F. C. Chen, A. Favetto, M. Mousavi, *et al.*, "Human hand: Kinematics, statics, and dynamics," DOI: 10.2514/6.2011-5249. eprint: https://arc.aiaa.org/doi/pdf/10.2514/6.2011-5249. [Online]. Available: https://arc.aiaa.org/doi/abs/10.2514/6.2011-5249.

[77] Stratasys, *Digital anatomy creator*, Online, Available: https://www.stratasys.com/en/fdm-technology/digital-anatomy-creator/, Oct. 2024.

[78] H. Huang and R. Talreja, "Effects of void geometry on elastic properties of unidirectional fiber reinforced composites," *Compos. Sci. Technol.*, vol. 65, no. 13, pp. 1964–1981, 2005.

[79] K. S. Lee and M. C. Jung, "Flexion and extension angles of resting fingers and wrist," *Int. J. Occup. Saf. Ergon.*, vol. 20, no. 1, pp. 91–101, 2014.

[80] F. Pelayo, D. Blanco, P. Fernández, J. González, and N. Beltrán, "Viscoelastic behaviour of flexible thermoplastic polyurethane additively manufactured parts: Influence of inner-structure design factors," *Polymers*, vol. 13, no. 14, p. 2365, Jul. 2021.

[81] W. Murphy, J. Black, and G. W. Hastings, *Handbook of Biomaterial Properties*. Springer, 2016.

[82] A. Sensini and L. Cristofolini, "Biofabrication of electrospun scaffolds for the regeneration of tendons and ligaments," *Materials*, vol. 11, no. 10, p. 1963, Oct. 2018. DOI: 10.3390/ma11101963.

[83] NinjaTek, *Ninjaflex tpu filament*, Online, Available: https://ninjatek.com/shop/ninjaflex/, Jul. 2025.

[84] AnyCubic, *Kobra max 2*, Online, Available: https://store.anycubic.com/products/kobra-2-max, Jul. 2025.

[85] S. Jerban, T. Hananouchi, Y. Ma, *et al.*, "Correlation between the elastic modulus of anterior cruciate ligament (acl) and quantitative ultrashort echo time (ute) magnetic resonance imaging," *Journal of Orthopaedic Research*, vol. 40, no. 10, pp. 2330–2339, Oct. 2022. DOI: 10.1002/jor.25266.

[86] Zygote Media Group, Inc., *Zygote 3d human anatomy models*, Online, Jul. 2025. [Online]. Available: https://www.zygote.com/.

[87] K. Browne, *3d reference organ for liver, female v1.1*, Online, 2021. [Online]. Available: https://doi.org/10.48539/HBM798.JZZM.649.

[88] K. Browne and H. Schlehlein, *3d reference organ for kidney, female, left v1.2*, Online, 2022. [Online]. Available: https://doi.org/10.48539/HBM898.QGVV.734.

[89] J. Wasserthal, H.-C. Breit, M. T. Meyer, *et al.*, "Totalsegmentator: Robust segmentation of 104 anatomic structures in ct images," *Radiology: Artificial Intelligence*, 2023. [Online]. Available: https://doi.org/10.1148/ryai.230024.

[90] A. Affane, M. A. Chetoui, J. Lamy, *et al.*, "The r-vessel-x project," *IRBM*, vol. 46, no. 1, p. 100 876, 2025. DOI: 10.1016/j.irbm.2025.100876.

[91] P. Cignoni, A. Muntoni, G. Ranzuglia, and M. Callieri, *Meshlab*, Online, Jul. 2025. [Online]. Available: https://www.meshlab.net/.

[92] Autodesk, Inc., *Meshmixer (for fusion)*, Online, Version 3.5.0, last updated Jan. 6, 2025, Jul. 2025. [Online]. Available: https://apps.autodesk.com/FUSION/en/Detail/Index?id=4108920185261935100&appLang=en&os=Win64.

[93] Autodesk, Inc., *Autodesk fusion*, Online, Jul. 2025. [Online]. Available: https://www.autodesk.com/products/fusion-360/overview.

[94] B. Brown and B. Herman, "Phantom materials for ultrasound imaging," *Ultrasound in Medicine & Biology*, vol. 31, no. 4, pp. 477–485, 2005.

[95] H. Kamalinia, A. Barbarulo, and B. Tie, "A coupled acoustic/elastic discontinuous galerkin finite element method: Application to ultrasonic imaging of 3d-printed synthetic materials," *Computers & Structures*, vol. 291, p. 107 208, 2024. DOI: 10.1016/j.compstruc.2023.107208.

[96] Stratasys, *Biomechanical evaluation of printed liver and myocardium samples – j5 digital anatomy™ printer*, Online, 2020. [Online]. Available: https://www.stratasys.com.

Appendices

Appendix A: MATLAB Code for Generating Void Parameters Within Solid Works

```
close all;clear all;clc;
%% Program
%Creates normally distributes coordinates for voids to be
   placed in a
%coupon of certain dimensions. The void size and distribution
   properties
%may also be changed to coupon designers needs. This should
   only be used
%for 3D void models
%% File erase
%if file is not found, you may have to comment out the delete
   functions to first create the
%excel
recycle on
delete('Coupon - Variable Pattern Table.xlsx')
delete('Control Coupon - Variable Pattern Table.xlsx')
%% Parameters and Inputs
%% pre-set constants
%coupon dimensions
l_coupon=152.4; %length
```

```
w_coupon= 25.4;%width
h_coupon= 3.175;%height

% space from surface in each dimension
surface_spacex=1.27;
surface_spacey=1.27;
surface_spacez= 0.1*(0.1*h_coupon);
print_res= 0.005; %printer resolution safety net that also
   prevents overlap

% % if statement ensures there is no structure failure at walls
% if print_res>surface_spacez || print_res>surface_spacey ||
   print_res>surface_spacex
%     fprintf("Ensure print resolution is lower than distance
   from surface chosen\n")
%     return
% end

%% variables
% Void dimensions(rectangular)
void_sizex= 0.01; % must be smaller than x dimension
void_sizey= 0.01; % must be smaller than y dimension
void_sizez=0.01;  % mmust be smaller than z dimension

% no. of voids along each specific dimension (whole number)
no_of_voidx= 20;
no_of_voidy= 10;
```

```
no_of_voidz=2;% must be greater than 2 for 3D
%for 2D please go to 2D code where number of voids in x and y
   must be greater than 1
%% Spacing Optimization/Validity for Variables Chosen
% if statement ensures the size of voids or number of voids
   dont overlap
% initially or exceed dimensions
if ((no_of_voidx*void_sizex)+(surface_spacex*2))<=l_coupon
x=linspace((surface_spacex),(l_coupon-surface_spacex-void_sizex
   ),(no_of_voidx+2))';% creates linear distribution of
   coordinates in x
else
    fprintf("Too many voids in X or size of void too large\n")
    return
end
if ((no_of_voidy*void_sizey)+(surface_spacey*2))<=w_coupon
y=linspace((surface_spacey),(w_coupon-surface_spacey-void_sizey
   ),(no_of_voidy+2))';% creates linear distribution of
   coordinates in y
else
    fprintf("Too many voids in Y or size of void too large\n")
    return
end
if ((no_of_voidy*void_sizez)+(surface_spacez*2))<=h_coupon
z=linspace((surface_spacez),(h_coupon-void_sizez-surface_spacez
   ),(no_of_voidz+2))';% creates linear distribution of
   coordinates in z
```

```
else
    fprintf("Too many voids in Z or size of void too large\n")
    return
end
% note 2 is added to void size in order to create end points on
    the numeber asked for so that thry can be
%equal distribution amongst internal points from the edge and
   be romoved after
% actual space between each void coordinate
spacex=x(2)-x(1);
spacey=y(2)-y(1);
spacez=z(2)-z(1);

%removes added end points
x([1,end])=[];
y([1,end])=[];
z([1,end])=[];

% radius/range of movement that void can move in x y and z
   plane
space_Rx= spacex-print_res-void_sizex;
space_Ry= spacey-print_res-void_sizey;
space_Rz=spacez-print_res-void_sizez;



%% Coordinate Creation
```

```
% if statement creates void coordinates for x and y depending
   on which one
% is larger
if length(x)>= length(y);
  for j= 1: length(y)
    for i = 1:length(x)
     Cordx(i,j)= x(i);
     Cordy(i,j)= y(j);
    end
  end
elseif length(y)>= length(x)
    for j= 1: length(x)
     for i = 1:length(y)
    Cordx(j,i)= x(j);
    Cordy(j,i)=y(i);
     end
    end
end
Cordx; %x cordinate matrix
Cordy; %y cordinate matrix

%Attaches z Coordinates to corresponding x and y
Cordz= z(1).*ones(no_of_voidx,no_of_voidy);
Cordy_3D=Cordy;
Cordx_3D= Cordx;
for p= 2:no_of_voidz
Cordz= [Cordz;z(p).*ones(no_of_voidx,no_of_voidy)];
```

```
Cordy_3D=[Cordy_3D;Cordy];
Cordx_3D=[Cordx_3D;Cordx];
end

%% Creates Linear Distribution Control Coupon
X= Cordx_3D(:,1); %x cordinate
Y= Cordy_3D(:,1); %y cordinate
Z=Cordz(:,1); %z cordinate
for q = 2:size(Cordx_3D,2)
X=[X;Cordx_3D(:,q)];
Y=[Y;Cordy_3D(:,q)];
Z=[Z;Cordz(:,q)];
end
Inst=[1:size(Y,1)]';
Insts= zeros(size(Y,1),1);
xbox_sample=ones(size(X,1),1)*void_sizex; %void x dim
ybox_sample=ones(size(Y,1),1)*void_sizey; %void y dim
zbox_sample=ones(size(Z,1),1)*void_sizez; %void z dim
Coord_sample = table(Inst,Insts,X,Z,zbox_sample,xbox_sample,
   ybox_sample,Y)
filename = 'Control Coupon - Variable Pattern Table.xlsx';
writetable(Coord_sample,filename,'Sheet','void-coordinates','
   Range','A2','WriteVariableNames',true)

%% Guassian Distribution Implementation
% creates gausian distribution under parameters and truncates
   it between -1
```

```
% and 1
pd= makedist('Normal',0,0.5); %0.1-0.4
trunc= truncate(pd,-1,1);

%Creates a different set of numbers for each dimension with the
    same set of parameters.
Gaus_ptsx=random(trunc,[size(Cordx_3D,1),size(Cordx_3D,2)]);
Gaus_ptsy=random(trunc,[size(Cordy_3D,1),size(Cordy_3D,2)]);
Gaus_ptsz=random(trunc,[size(Cordz,1),size(Cordz,2)]);%check if
    syntax is right
%checks that truncation worked
max(Gaus_ptsz);
min(Gaus_ptsz);

% Adds normal distribution of displacement values to linear
   system to
% create random distribution of voids
x_gaus= Cordx_3D+(Gaus_ptsx.*space_Rx);
y_gaus=Cordy_3D+(Gaus_ptsy.*space_Ry);
z_gaus=Cordz+(Gaus_ptsz.*space_Rz);

%Places new coordinates(x,y and z_gaus) into desired format for
    export
X_dim= x_gaus(:,1); %x cordinate distributed
Y_dim= y_gaus(:,1); %y cordinate distributed
Z_dim=z_gaus(:,1); %z cordinate distributed
for m= 2:size(x_gaus,2)
```

```
X_dim=[X_dim;x_gaus(:,m)];
Y_dim=[Y_dim;y_gaus(:,m)];
Z_dim=[Z_dim;z_gaus(:,m)];
end


%% Prepares coordinate data for export to SolidWorks
Instance=[1:size(Y_dim,1)]';
Instances= zeros(size(Y_dim,1),1);
xbox=ones(size(X_dim,1),1)*void_sizex;%void x dim
ybox=ones(size(Y_dim,1),1)*void_sizey;%void y dim
zbox=ones(size(Z_dim,1),1)*void_sizez;%void z dim
Coordinates = table(Instance,Instances,X_dim,Z_dim,zbox,xbox,
   ybox,Y_dim)
filename = 'Coupon - Variable Pattern Table.xlsx';
writetable(Coordinates,filename,'Sheet','void-coordinates','
   Range','A2','WriteVariableNames',true)
%% Test data for reasonable normal distribution
histogram(Cordx)
figure(2)
histogram(X_dim)
\end{}
```

Appendix B: MATLAB Code for ROI Extraction and Grayscale Analysis of Ultrasound Images

```
clear all;
```

```
clc;
close all;
% File list
file_ = { ...
    'coupon_human.png','coupon_human2.png','coupon_human3.png',
       'coupon_1.png','coupon_6.png','coupon_9.png','coupon_10.
       png','coupon_7.png','coupon_12.png','coupon_13.png','
       coupon_2.png','coupon_3.png','coupon_4.png','coupon_5.
       png','coupon_8.png',...
    'coupon_11.png','coupon_14.png','coupon_16.png','coupon_17.
       png'};

pixel_size = 1/114;   % pixel size in cm
pixel_size_human = 5/226;  % pixel size in cm for human scan
crop_top = 20;        % pixel to crop from top to 0 on scan
   scale

num_images = length(file_);
roi_data = struct();            % initialize ROI data
images = cell(1, num_images);   % for SSIM

%% Prepare Reference Image from Body

% roi_angle_human = 45;      % degrees
% r_min_human = 0.65;        % cm
% r_max_human = 1.25;        % cm
```

```
w= 1; %cm
h= 0.5; %cm
offset= 0.65; %cm
echo_pos= [155,395,464];          %px
for n= 1:3 % liver, renal medula, renal pelvis
    % Load image
    image_path = file_{n};
    img_ = imread(image_path);

    % Convert to grayscale if needed
    if size(img_, 3) == 3
        img_gray_ = rgb2gray(img_);
    else
        img_gray_ = img_;
    end
    img_gray_ = imgaussfilt(img_gray_, 0.5); %gaussian blur
    % Crop to ultrasound origin
    [imgH, imgW] = size(img_gray_);
    crop_top_px = crop_top; %round(crop_top / pixel_size);
    img_cropped = img_gray_(crop_top_px+1:end, :);
    [cropH, cropW] = size(img_cropped);

    % Create polar coordinate grid
    [X_, Y_] = meshgrid(1:cropW, 1:cropH);
   % r_min_hpx = r_min_human / pixel_size_human;
    %r_max_hpx = r_max_human / pixel_size_human;
    w_hpx = w/ pixel_size_human;
```

```
h_hpx = h/ pixel_size_human;
offset_hpx = offset/pixel_size_human;
cx = cropW / 2;
cy = echo_pos(n)- offset_hpx ;

% Compute top-left corner of rectangle
rect_y = round(cy + offset_hpx);
rect_x = round(cx - w_hpx / 2);  % center the box
   horizontally

% Ensure the rectangle stays within image bounds
rect_y = round(max(1, rect_y));
rect_x = round(max(1, rect_x));
rect_y_end = round(min(rect_y + h_hpx - 1, cropH));
rect_x_end = round(min(rect_x + w_hpx - 1, cropW));

roi_area = false(size(img_cropped));
roi_area(rect_y:rect_y_end, rect_x:rect_x_end) = 1;



roi_img = img_cropped;
[row_idx, col_idx] = find(roi_area);
min_row = min(row_idx);
max_row = max(row_idx);
min_col = min(col_idx);
max_col = max(col_idx);
```

```
% Crop the image to ROI
roi_img = img_cropped(min_row:max_row, min_col:max_col);

 % Save ROI image to disk
 roi_save_name = sprintf('ROI_image_human%02d.png', n);
 imwrite(uint8(roi_img), roi_save_name);

 % Display Cropped & ROI (optional visualization)
 % figure;
 % subplot(1,2,1); imshow(img_cropped); %title(sprintf('
    Cropped Image human%d', n));
 % hold on;
 % visboundaries(roi_area, 'Color', 'r','linewidth',1);
 % subplot(1,2,2); imshow(roi_img); %title(sprintf('ROI -
    Image human%d', n));
 %   title('Rectangular ROI at Distance from Origin');

 % Mean and Std Dev
 roi_double = double(roi_img);
 roi_vals = roi_double(:);  % include only ROI pixels
 roi_mean = mean(roi_vals);
 roi_std = std(roi_vals);

 roi_data(n).Mean = roi_mean;
 roi_data(n).StdDev = roi_std;

 % Store cropped image for SSIM
```

```
    images{n} = im2double(roi_img);
end
%Draw ROI overlay on original image
figure;
imshow(img_gray_(1,2,3)); %title(sprintf('Cropped Overlay %d',
   i-n));
hold on;
visboundaries(roi_area(1,2,3), 'Color', 'r');
%% Prepare coupon Images
for i = n+1:num_images
    % Load image
    image_path = file_{i};
    img_ = imread(image_path);

    % Convert to grayscale if needed
    if size(img_, 3) == 3
        img_gray_ = rgb2gray(img_);
    else
        img_gray_ = img_;
    end
    img_gray_ = imgaussfilt(img_gray_, 0.5); %gaussian blur
    % Crop to ultrasound origin
    [imgH, imgW] = size(img_gray_);
    crop_top_px = crop_top; % round(crop_top / pixel_size);
    img_cropped = img_gray_(crop_top_px+1:end, :);
    [cropH, cropW] = size(img_cropped);
```

```
% Create coordinate grid
[X_, Y_] = meshgrid(1:cropW, 1:cropH);
cx = cropW / 2;
cy = 0;

%roi_img = img_cropped;
%roi_img(~roi_area) = 0;

w_px = w/ pixel_size;
h_px = h/ pixel_size;
offset_px = (offset/pixel_size);

% Compute top-left corner of rectangle
rect_y = round(cy + offset_px);
rect_x = round(cx - w_px / 2);  % center the box
   horizontally

% Ensure the rectangle stays within image bounds
rect_y = round(max(1, rect_y));
rect_x = round(max(1, rect_x));
rect_y_end = round(min(rect_y + h_px - 1, cropH));
rect_x_end = round(min(rect_x + w_px - 1, cropW));

roi_area = false(size(img_cropped));
roi_area(rect_y:rect_y_end, rect_x:rect_x_end) = 1;
```

```
 roi_img = img_cropped;
 [row_idx, col_idx] = find(roi_area);
 min_row = min(row_idx);
 max_row = max(row_idx);
 min_col = min(col_idx);
 max_col = max(col_idx);

% Crop the image to ROI
roi_img = img_cropped(min_row:max_row, min_col:max_col);

 % Save ROI image to disk
 roi_save_name = sprintf('ROI_Image_%02d.png', i-n);
 imwrite(uint8(roi_img), roi_save_name);

 %Display Cropped & ROI (optional visualization)
 % figure;
 % subplot(1,2,1); imshow(img_cropped); %title(sprintf('
    Cropped Image %d', i-n));
 % hold on;
 % visboundaries(roi_area, 'Color', 'r');
 % subplot(1,2,2); imshow(roi_img); title(sprintf('ROI -
    Image %d', i-n));

 %% Mean and Std Dev
 roi_double = double(roi_img);
 roi_vals = roi_double(:);  % include only ROI pixels
 roi_mean = mean(roi_vals);
```

```
    roi_std = std(roi_vals);

    roi_data(i).Mean = roi_mean;
    roi_data(i).StdDev = roi_std;

    %Draw ROI overlay on original image
    % figure;
    % imshow(img_cropped); %title(sprintf('Cropped Overlay %d',
        i-n));
    % hold on;
    % visboundaries(roi_area, 'Color', 'r','linewidth',1);

    % Store cropped image for SSIM
    images{i} = im2double(roi_img);
end

img_stack = cat(3, images{4:end});
img_avg = mean(img_stack, 3);
figure;
imshow(img_avg,[]);
for p=1:16
    img_error(:,:,p) = abs(img_avg - img_stack(:,:,p));
    imwrite(mat2gray(img_error(:,:,p)), sprintf('Error_Image_
       %02d.png', p));
    % figure;
    % imshow(img_error(:,:,p),[]);
end
```

```
title={'liver', 'RM', 'RP'};
colors = [
    0.35 0.70 0.90;  % Sky Blue
    0.00 0.60 0.50;  % Bluish Green
    0.80 0.40 0.00;  % Vermillion
];
for m=1:3
    ref_img = images{m};
    [H, W] = size(ref_img);

    for k = 4:num_images
        if ~isequal(size(images{k}), [H W])
            images{k} = imresize(images{k}, [H W]);
        end
    end

% Create and display ROI table with SSIM
ref_mean = roi_data(m).Mean;

% Preallocate grayscale error arrays
gray_errors = zeros(1, num_images - (n));
gray_stddev = zeros(1, num_images - (n));

for k = 4:num_images
    gray_errors(k - 2) = abs(roi_data(k).Mean - ref_mean);
```

```
    gray_stddev(k - 2) = abs(roi_data(k).StdDev - roi_data(m).
       StdDev);
end

gray_errors = gray_errors';
gray_stddev = gray_stddev';

%% Display
% Create table
roi_table = table((1:(num_images-(n-1)))', gray_errors,
   gray_stddev, ...
    'VariableNames', {'Coupon_No', 'GrayError', 'GrayErrorStd'
       });

fprintf( 'Grayscale Error Comparison - %s:\n',title{m});
disp(roi_table);
fprintf('\n');

% Save per-reference table
writetable(roi_table, sprintf('ROI_Statistics_%s.csv', title{m
   }));

ref_label{m} = title{m};
ref_avg(m) = roi_data(m).Mean;
ref_std(m) = roi_data(m).StdDev;

gray_means = [roi_data(n+1:end).Mean]';
```

```
gray_stds  = [roi_data(n+1:end).StdDev]';

%mean_diff = gray_means - ref_mean;    % deviation from
   reference mean
%std_diff  = gray_stds - ref_std;      % deviation from
   reference std

end

no_coupon = 1:16;

% Plot grayscale mean + std deviations
figure;
errorbar(no_coupon, gray_means, gray_stds, 'o', ...
    'Color', [0,0,0], 'MarkerFaceColor',[0,0,0], 'LineWidth',
       1.5);
hold on;
yline(ref_avg(1), '--', sprintf('%s ROI Mean = %.2f grayscale',
    ref_label{1}, ref_avg(1)), ...
    'Color', colors(1,:), 'LineWidth', 1.5, 'FontName', 'Times
       New Roman', 'FontSize', 12,'LabelHorizontalAlignment', '
       left');

yline(ref_avg(2), '--', sprintf('%s ROI Mean = %.2f grayscale',
    ref_label{2}, ref_avg(2)), ...
```

```
    'Color', colors(2,:), 'LineWidth', 1.5, 'FontName', 'Times
       New Roman', 'FontSize', 12,'LabelHorizontalAlignment', '
       left');

yline(ref_avg(3), '--', sprintf('%s ROI Mean = %.2f grayscale',
    ref_label{3}, ref_avg(3)), ...
    'Color', colors(3,:), 'LineWidth', 1.5, 'FontName', 'Times
       New Roman', 'FontSize', 12,'LabelHorizontalAlignment','
       left');
xlabel('Sample Number','FontName', 'Times New Roman', 'FontSize
   ', 12);
ylabel('Average Grayscale Values of ROI','FontName', 'Times New
    Roman', 'FontSize', 12);
%title(sprintf('Grayscale Mean & Std Dev Deviation vs %s',
   ref_label));
grid on;
xlim([0.5, length(no_coupon)+0.5]);
xticks(no_coupon);
%legend('Mean +/- Std Deviation','Location','northeastoutside')
   ;
set(gca, 'FontName', 'Times New Roman', 'FontSize', 12);

roi_table_1 = table((1:num_images)', [roi_data.Mean]', [
   roi_data.StdDev]', 'VariableNames', {'Coupon_No', 'Mean', '
   StdDev'});
fprintf('ROI Intensity Stats:\n');
disp(roi_table_1);
```

```
fprintf('\n');
writetable(roi_table_1, sprintf('ROI_Statistics.csv'));

% Plot Samples with Similar Echogenic properties together on
   plot

gray_means_echogenic= gray_means
   ([6,7,12,13,1,2,5,8,14,3,4,11,9,10,15,16]);
      gray_stds_echogenic = gray_stds
         ([6,7,12,13,1,2,5,8,14,3,4,11,9,10,15,16])
no_coupon_reordered = {'6','7','12','13','1','2','5','8','14','
   3','4','11','9','10','15','16'};

% Plot grayscale mean + std deviations
figure;
errorbar(no_coupon, gray_means_echogenic, gray_stds_echogenic,
   'o', ...
    'Color', [0,0,0], 'MarkerFaceColor',[0,0,0], 'LineWidth',
       1.5);
hold on;
yline(ref_avg(1), '--', sprintf('%s ROI Mean = %.2f grayscale',
    ref_label{1}, ref_avg(1)), ...
    'Color', colors(1,:), 'LineWidth', 1.5, 'FontName', 'Times
       New Roman', 'FontSize', 12,'LabelHorizontalAlignment', '
       left');
```

```
yline(ref_avg(2), '--', sprintf('%s ROI Mean = %.2f grayscale',
    ref_label{2}, ref_avg(2)), ...
    'Color', colors(2,:), 'LineWidth', 1.5, 'FontName', 'Times
       New Roman', 'FontSize', 12,'LabelHorizontalAlignment', '
       left');

yline(ref_avg(3), '--', sprintf('%s ROI Mean = %.2f grayscale',
    ref_label{3}, ref_avg(3)), ...
    'Color', colors(3,:), 'LineWidth', 1.5, 'FontName', 'Times
       New Roman', 'FontSize', 12,'LabelHorizontalAlignment','
       left');
xlabel('Sample Number','FontName', 'Times New Roman', 'FontSize
   ', 12);
ylabel('Average Grayscale Values of ROI','FontName', 'Times New
    Roman', 'FontSize', 12);
%title(sprintf('Grayscale Mean & Std Dev Deviation vs %s',
   ref_label));
grid on;
xlim([0.5, length(no_coupon)+0.5]);
xticks(no_coupon);
xticklabels(no_coupon_reordered);
%legend('Mean +/- Std Deviation','Location','northeastoutside')
   ;
set(gca, 'FontName', 'Times New Roman', 'FontSize', 12);
```